Rock-slope Activity Index (RAI): a lidar-derived process-based rock-slope assessment system

Lisa Ann Dunham

A thesis submitted in partial fulfillment of the requirements for the degree of

Master of Science in Civil Engineering

University of Washington

2015

Committee:

Dr. Joseph Wartman

Dr. Pedro Arduino

Program authorized to offer degree: Civil and Environmental Engineering

©Copyright 2015
Lisa Ann Dunham

University of Washington

Abstract

Rockslope Activity Index (RAI)

Lisa Ann Dunham

Chair of the Supervisory Committee:
Dr. Joseph Wartman H.R. Berg Associate Professor
Civil And Enviromental Engineering

Inventory of unstable highway slopes is an immense challenge for Departments of Transportation (DOTs) due to the geographic dispersion of problematic slopes as well as the variable nature and speed of erosional processes. Due to advancements in lidar technology, acquisition of high resolution spatial data to map and monitor these slopes is becoming simpler, less expensive, and more widely available. Further, the collected data can be used for wide array of applications in addition to the slope inventory, enabling new discoveries for a variety of applications. However, several challenges remain in using lidar for slope assessment. One key problem is the amount of data collected requires significant data processing, a steep learning curve, and can be labor and computationally intensive. To reduce this bottleneck an automated classification system for characterizing rock slopes and calculating their likelihood of failure from lidar data has been developed. This algorithm quickly extracts morphological indices and evaluates them to determine the likelihood of failure throughout the entire face of each rock outcrop. To test this algorithm, a series of terrestrial lidar scans have been completed for several road cuts located adjacent to the Glenn and Parks Highways in Alaska over a three year period. Areas screened as highly unstable are being compared to erosion estimates obtained from the time series lidar data for validation. DOTs can then use this method directly with traffic information for risk assessment, improving safety and enabling them to efficiently determine how to allocate limited resources for road and slope improvements.

Table of Contents

Figures

Tables

Acronyms

AKDOT&PF	Alaska Department of Transportation and Public Facilities
DEM	Digital Elevation Model
DOT	Department of Transportation
FHWA	Federal Highway Administration
GG	Glitter Gulch
GNSS	Global Navigation Satellite System
GPS	Global Positioning System
Lidar	Light detection and Ranging
LL	Long Lake
m	meters
mJ	mili Joules
MP	Milepost
OSU	Oregon State University
PacTrans	Pacific Northwest Transportation Consortium
RAI	Rock-slope Activity Index
RDA	Rock-slope Deterioration Assessment
RHRS	Rockfall Hazard Rating System
SFM	Structure for Motion
USMP	Unstable Slope Management Program
USMR	Unstable Slope Management Report

Dedication

To my parents

Acknowledgements

I would like to thank Alaska Department of Transportation and Public Facilities and Pacific Northwest Transportation Consortium (PacTrans) for financial support of this project. Also, I would like to thank the team which worked on this project, in particular Michael Olsen from Oregon State University and Keith Cunningham from University of Alaska Fairbanks. Most of all, I would like to thank my adviser Joseph Wartman for the support and encouragement.

1. Introduction

Slope stability along highways is a major concern in areas where there are active slopes and where even small failures can have a significant effect on a transportation network. Slope failures can have affects ranging from block traffic leading to economic losses to possible death or injury resulting from debris hitting traffic. Small amounts of hard material such as a rock could damage an oil pan and strand motorists far from service centers and roadside help, especially in remote areas. The role of the Department of Transportations (DOT) in maintaining safe driving conditions can be difficult when such a wide range of slope hazards can cause problems, especially when small incidents which can be hard to predict. The ability to know where these failures are likely to occur can improve road safety and lessen the impact on DOT budgets.

Through asset management, DOTs keep track of and plan maintenance and replacement of different types of assets to increase service life and decrease costs. According to the Federal Highway Administration (FHWA, 2013), states must have Transportation Asset Management Plans that include pavements and bridges, but the FHWA also encourages including all infrastructure assets (Federal Highway Administration, 2014). Other infrastructure assets would include geotechnical assets, which a 2013 FHWA report suggests the need to include because the economic losses due to failures in geotechnical assets are much greater than the mitigate costs (FHWA, 2013).

Currently, geotechnical asset management is not standardized and only a few DOTs monitor anything other than slopes. According to the 2013 FHWA report, at least 25 states use the Rockfall Hazard Rating System (RHRS) (Pierson, 1991) to monitor slopes within their corridors. The RHRS provides a general understanding of the processes acting on slopes and assigns a numerical to assess the relative hazard. Systems such as the RHRS typically focus on one of two major aspects of the slope, either major structural features or the weathering of parent rock, (e.g. RHRS) or erosional processes (e.g. Rockslope Deterioration Assessment (RDA) Nicholson, 2005). These systems require varying levels of field reconnaissance which requires trained personal, resources, and time.

Advancing technology such as Light Detection and Ranging (lidar) enable high resolution monitoring and assessment of slopes that is not possible through current methods. Several states have already adopted lidar as an asset management tool using it for bridges and pavements (Ellsworth, 2013; Rister, McIntosh, & Whelan, 2013). Some DOTs are adopting lidar for the assessment of geotechnical assets as well, but lidar derived tools for the analyses of slopes are limited. The need for tools to help understand slope processes and classify areas as to potential hazard and quantify this hazard are needed so that DOTs can have a standard for the comparison of slopes. As noted by Lato: “A new lidar based rock-mass rating system is essential to the development of Lidar as a geotechnical evaluation tool.” (Lato, Diederichs, & Hutchison, 2012)

The Rockslope Activity Index (RAI) is a Lidar-Derived Process-Based Rock-Slope assessment system. Through this system, rock slopes can automatically be classified into different geomorphological categories which are then evaluated for hazard. Rock slopes are assessed for potential hazard in the measurement of the probable amount of kinetic energy that will be released to the road surface. Sites can be assessed against each other or divided into sections and assessed to find areas that have a higher probability of activity or “energy release”. This system aims to classify both the major failure areas as well as areas of smaller failures.

2. Site Information

Two study areas were selected as study areas by engineers at the Alaska Department of Transportation and Public Facilities (AKDOT&PF). These sites were selected to the needs of the AKDOT&PF in monitoring a diverse series of rock-slopes within their system. These sites also have the need of continuing maintenance where rock falls have damaged the road and a cause a life safety threat. Along with these considerations, these sites needed to be accessible so both mobile (i.e. vehicle-mounted) lidar and terrestrial-based lidar can be used. Also, consideration of vegetated areas which may need filtering of data to produce a higher quality point cloud.

2.1 Study Sites

Study sites of interest are locations with slopes along transportation corridors that would be suitable for formulating a proactive method of slope stability analysis are seen in Figure 2.1. The first site is located along Parks Highway Alaska Route 3 at Mileposts 239 and 241. The second site is located on the Glenn Highway (Alaska Route 1), between mileposts 78 to 89. Appendix A maps individual sites.

2.2 Geologic Setting

Alaska largely consists of numerous accreted terranes as shown in Figure 2.2. These terranes are the product of subduction, whereby the pacific plate acted as a conveyer belt of material bringing portions of distinctly different rock that has become bound together by faults (Thornberry-Ehrlich, 2010). Figure 2.3 is a north-south cross section of Alaska that shows the various terranes accreted over geologic time. The collision of these terranes with the existing land mass has caused the uplift of mountains (i.e., Orogeny), volcanic activity, and seismicity that are associated with Alaska today.

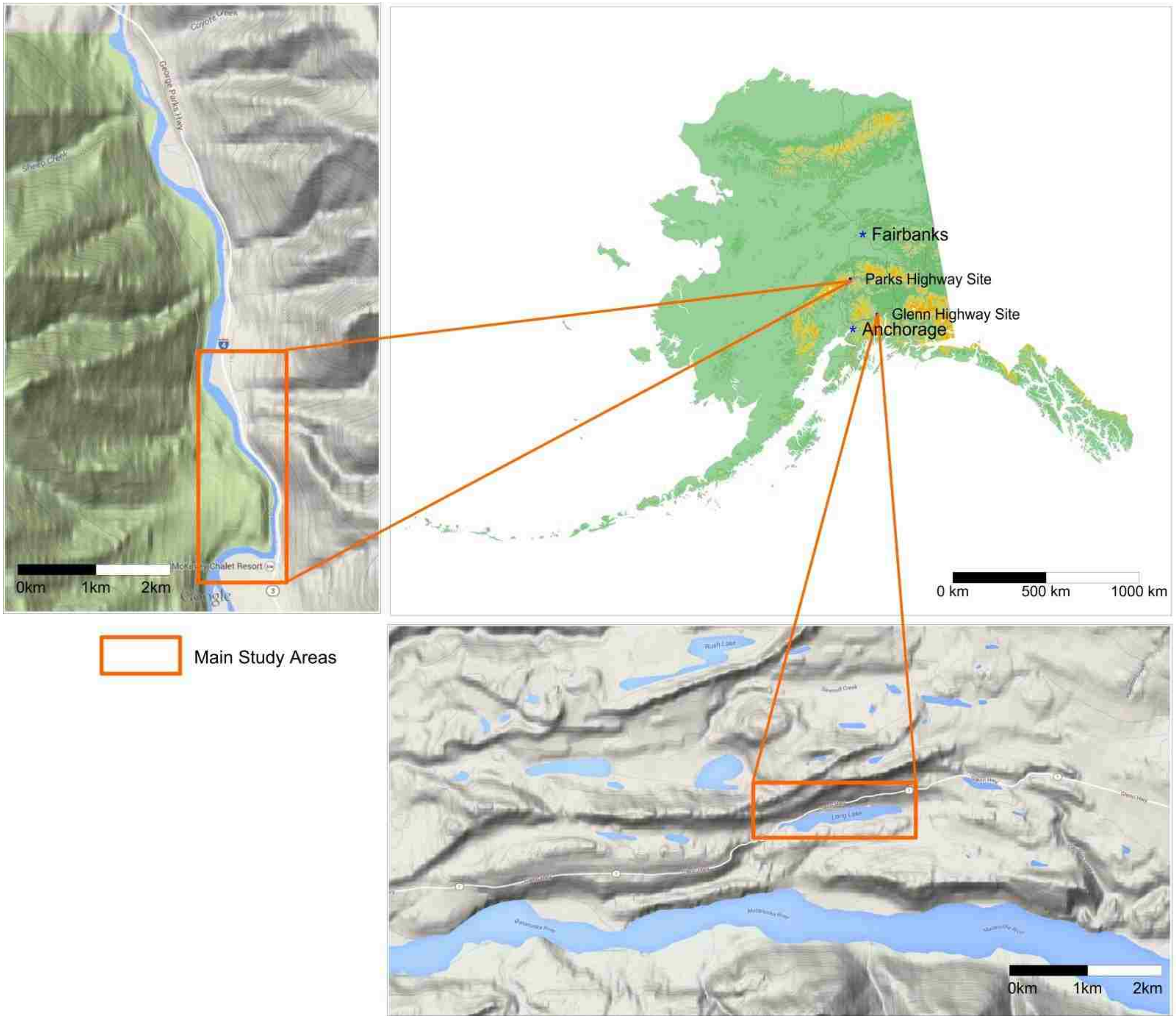

Figure 2.1 The locations of the two sites in relation to Fairbanks and Anchorage. (Alaska Department of Resources and Google)

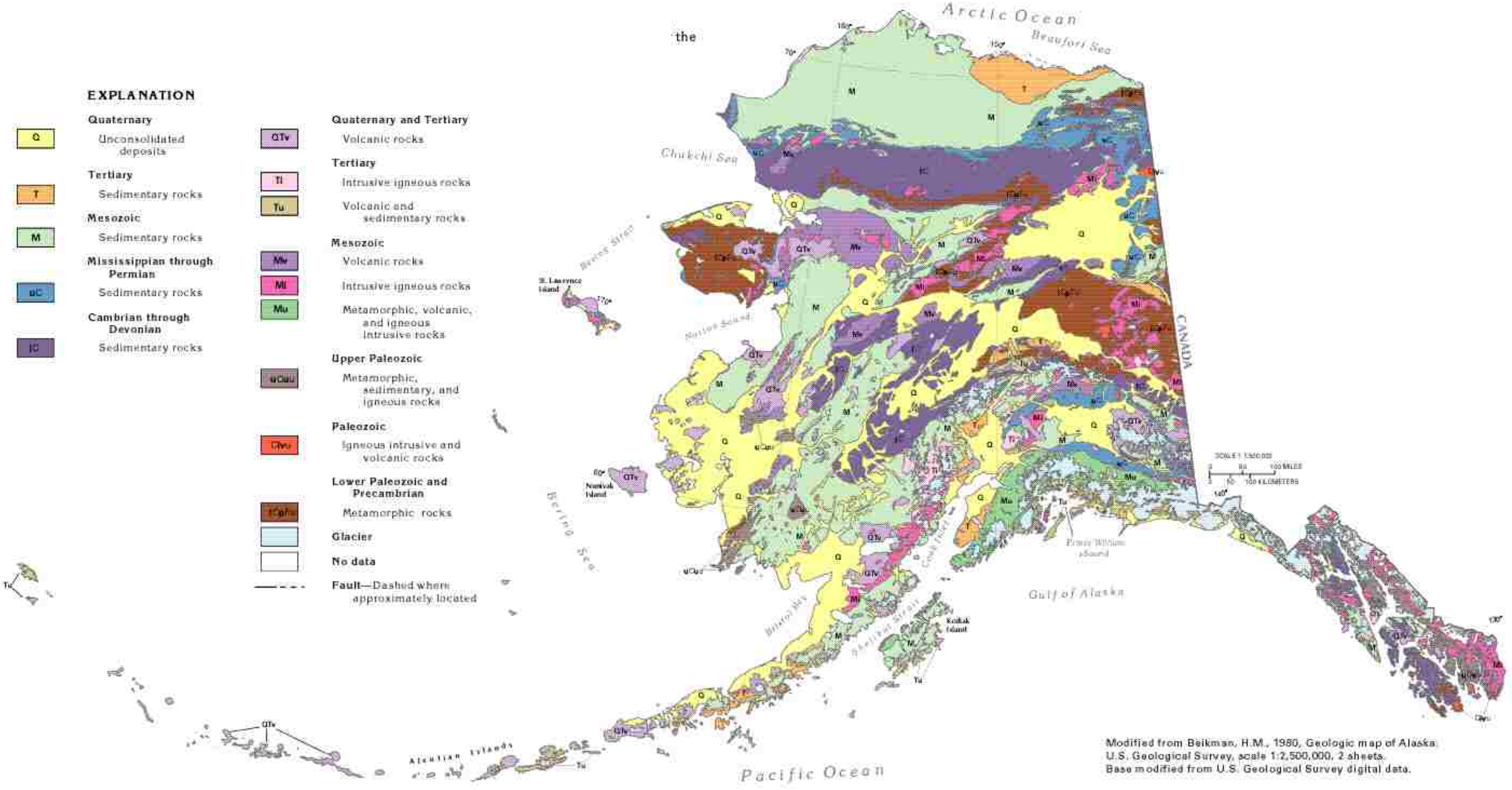

Figure 2.2 General geology map of Alaska (Miller & Whitehead, 1999)

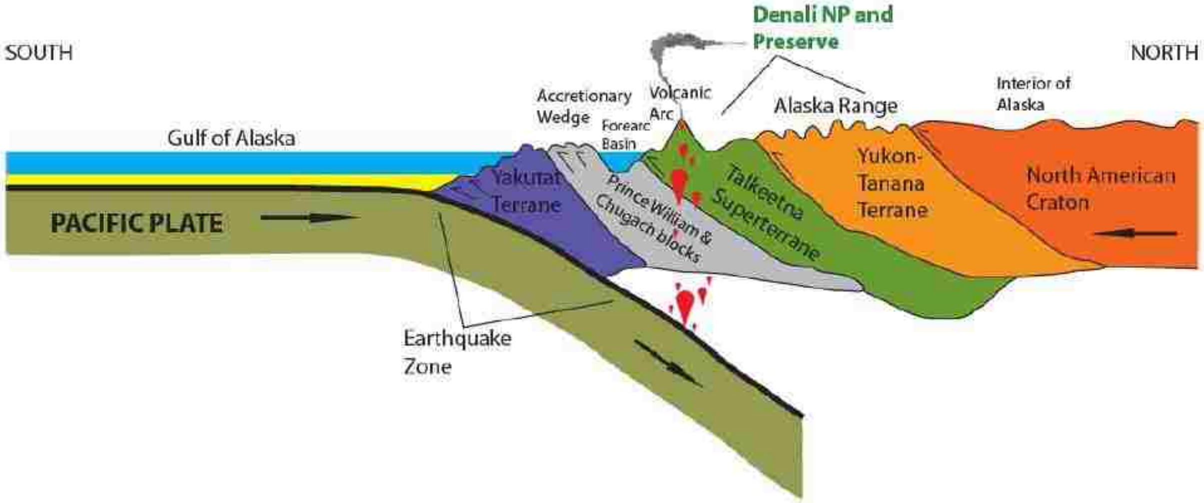

Figure 2.3 Generalized section of terrain from interior of Alaska to the Gulf of Alaska showing different terrains that have been added to Alaska. (Thornberry-Ehrlich, 2010)

2.3.1 Geology of Parks Highway Site

Parks Highway site is located within the Yukon-Tanana Terrane, which is the oldest terrane that has been added to Alaska. This terrane is part of what is now known as the Alaska Range, a chain of mountains that extends east to west along the south of Alaska creating a drainage divide between the Cook Inlet and the Yukon lowlands (Thornberry-Ehrlich, 2010). The Alaska Range is also faulted by the Denali fault which runs approximately 30 km (20 miles) to the south of the study area and does not directly affect the Parks Highway site.

The main type of rock found within the Parks Highway study area is a rock is known as Birch Creek Schist or Healy Schist (Figure 2.4) that Connor (1988) describes as “metamorphic rocks, muscovite-quartz schist, micaceous quartz and lesser amounts of graphitic schist.” Wahrhaftig (1958) notes that Birch Creek schist is inherently weak because of its "ease of separation along planes of foliation, produced by tiny, oriented mica flakes." This rock also includes cross joints, which run near vertical and may locally abut basalt dikes. Figure 2.6 is a geologic map of the area that shows volcanic dikes (Tvim, Tvif) within the Healy schist (PzpCp). The volcanic rock can be clearly seen as the darker rock in Figure 2.5, with a lighter Healy schist layer below.

Figure 2.4 Close up of Healy Schist a metamorphic rock containing quartz, schist and mica.

Figure 2.5 Slope at parks highway showing the darker volcanic rock, on top of the lighter Healy schist.

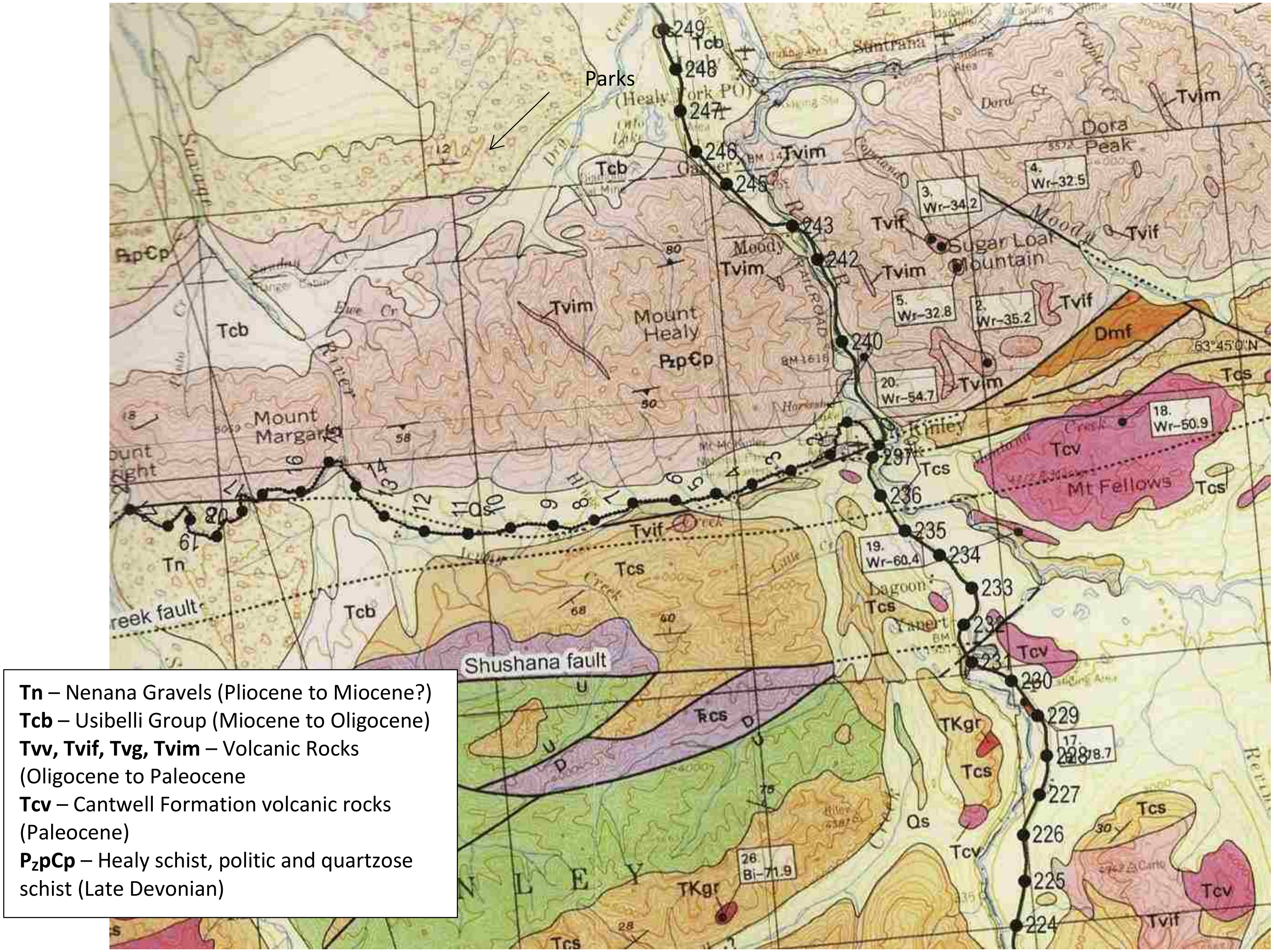

Tn – Nenana Gravels (Pliocene to Miocene?)
Tcb – Usibelli Group (Miocene to Oligocene)
Tvv, Tvif, Tvg, Tvim – Volcanic Rocks (Oligocene to Paleocene
Tcv – Cantwell Formation volcanic rocks (Paleocene)
P_zpCp – Healy schist, politic and quartzose schist (Late Devonian)

Figure 2.6 Area surrounding the Parks Highway site highlighting the geology. Sites for this study where between Mileposts 239 and 241. (Hults, Capps and Brease 2013)

2.3.2 Geology of Glenn Highway Site

The Glenn Highway site, which also lies within a region of accreted terrane, primarily consists of sedimentary rocks of the Matanuska and Chickaloon Formations. This area formed at first as a marine sediment, as show in Figure 2.7 a, during the orogenic rise of the Talkeetna Mountains. As the Mantanuska Formation was uplifted forming the mountains, erosion deposited propagating alluvial fans that became the Chickaloon Formation (Figure 2.7 b and c) [Belowich, 2006]. Local faulting can be seen throughout the area around Glenn Highway. One major fault, the Castle Mountain Fault runs parallel to the road about 5 km (3 miles) north of the Long Lake; there is no evidence that it is currently active or that it affects the study area. The valley where the highway runs follows a glacial cut into the Chickaloon Formation; however, no other glacial evidence is found in the area (Trop & Plawman, 2006).

The chosen study areas were mostly within the Chickaloon formation, which has four distinct lithologic units, (1) coal bearing rock, (2) shale, siltstone and claystone, (3) sandstone and (4) conglomerate [(Trop 2006) (R&M Consultants, INC., 2005)]. Figure 2.8 shows the Chickaloon formation manifesting itself as a carbonaceous siltstone overridden by a mafic sill intrusion. These mafic sills are located throughout the Matanuska and Chickaloon Formations. In contrast, Figure 2.9 shows sandstone from the Chickaloon formation in block failure in one of the study sites (Milepost 85.5). The other study site along Glenn Highway (Milepost 87), can be seen in Figure 2.10 with a manifestation of the carbonaceous siltstones overridden by the sandstones both of the Chickaloon formation. This combination creates differential erosion at the contact as the siltstones erode more quickly than the sandstones creating overhangs within the sandstone. Figure 2.11 presents a generalized cross section of the Long Lake region showing the Matanuka formation (Km) below the Chickaloon formation (Tc) near the Castle Mountain Fault (CMF). The general geology of the Long Lake region is shown on Figure 2.12, with the dotted line indicating the location of the Glenn Highway.

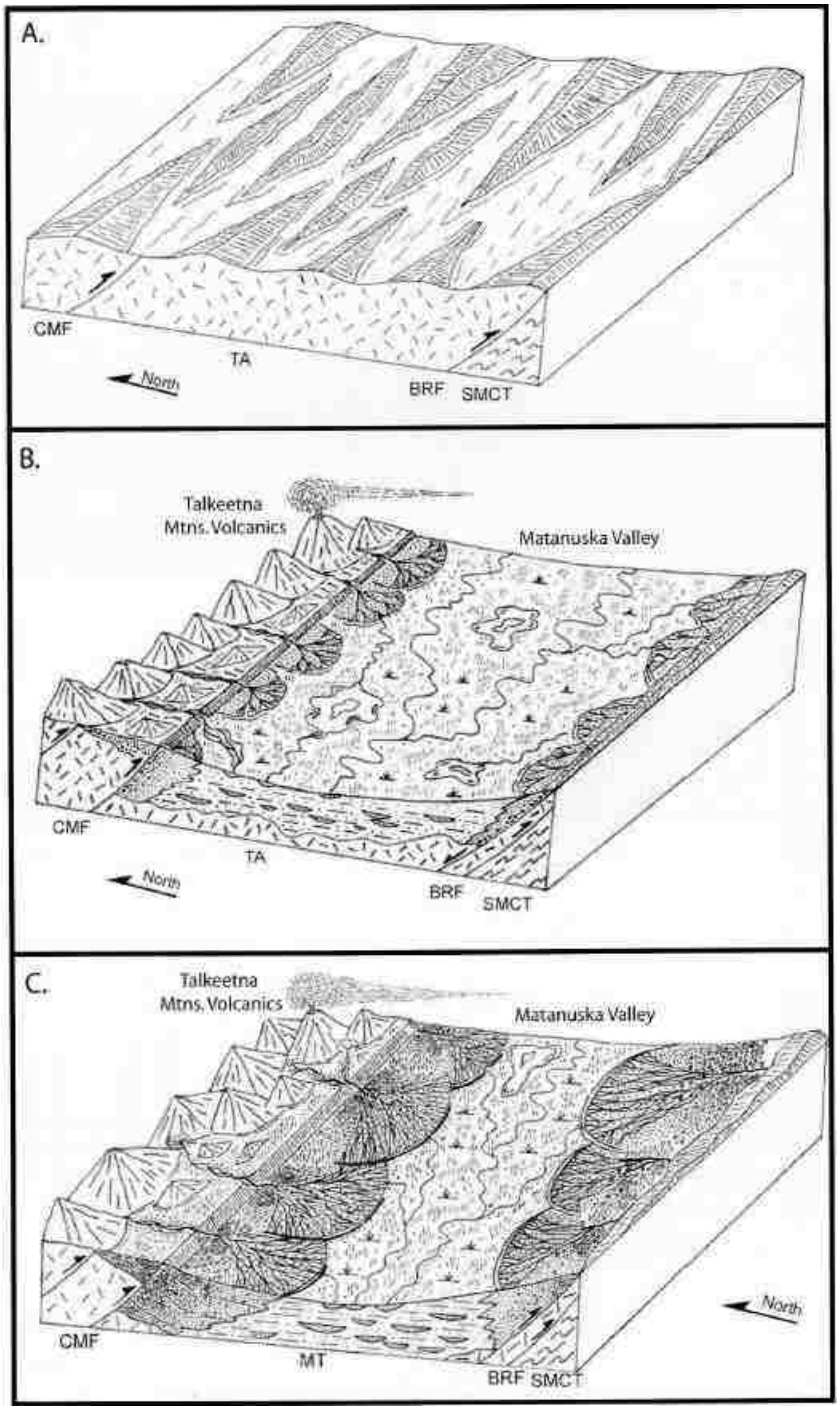

Figure 2.7 The building of the Glenn Highway area. A) Uplift of the Matanuska formation in the Cretaceous-Paleocene from marine strata. B) Talkeetna Mountains form with volcanic activity. Alluvial fans develop at base of mountains. Braided streams within the valley floor. C) Alluvial fans propagate, Castle Mountain fault (CMF) displaces. (Trop 2006)

Figure 2.8: Carbonous rock in the Chickaloon Formation below with mafic sill intrusions on top as seen near Milepost 85

Figure 2.9: Chickaloon formation sandstone in block failure near Milepost 85.5.

Figure 2.10: Carbonous siltstones overridden by a sill. The siltstones are a weaker material and therefore erode faster than the sill causing overhangs within the sill. To the right a fault can be seen offsetting these strata. These faults can be seen throughout the Chickaloon formation.

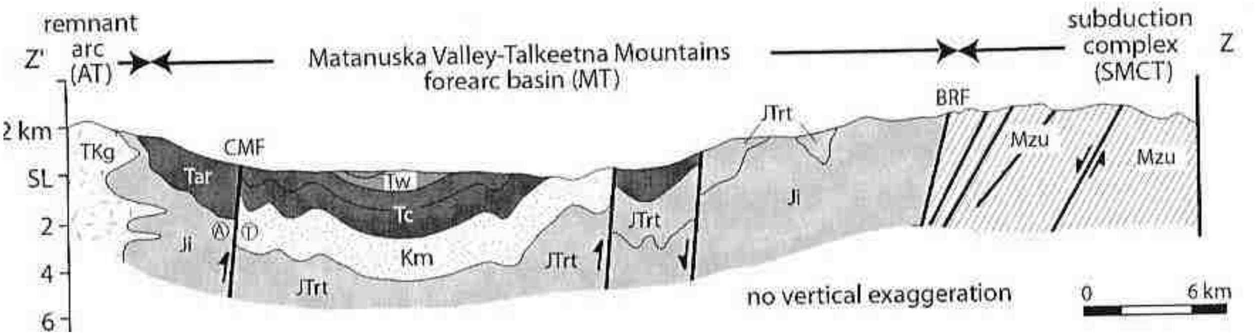

Figure 2.11 Cross section of the Matanuska Valley-Talkeetna Mountains forearc basin (Trop and Plawman, 2006)

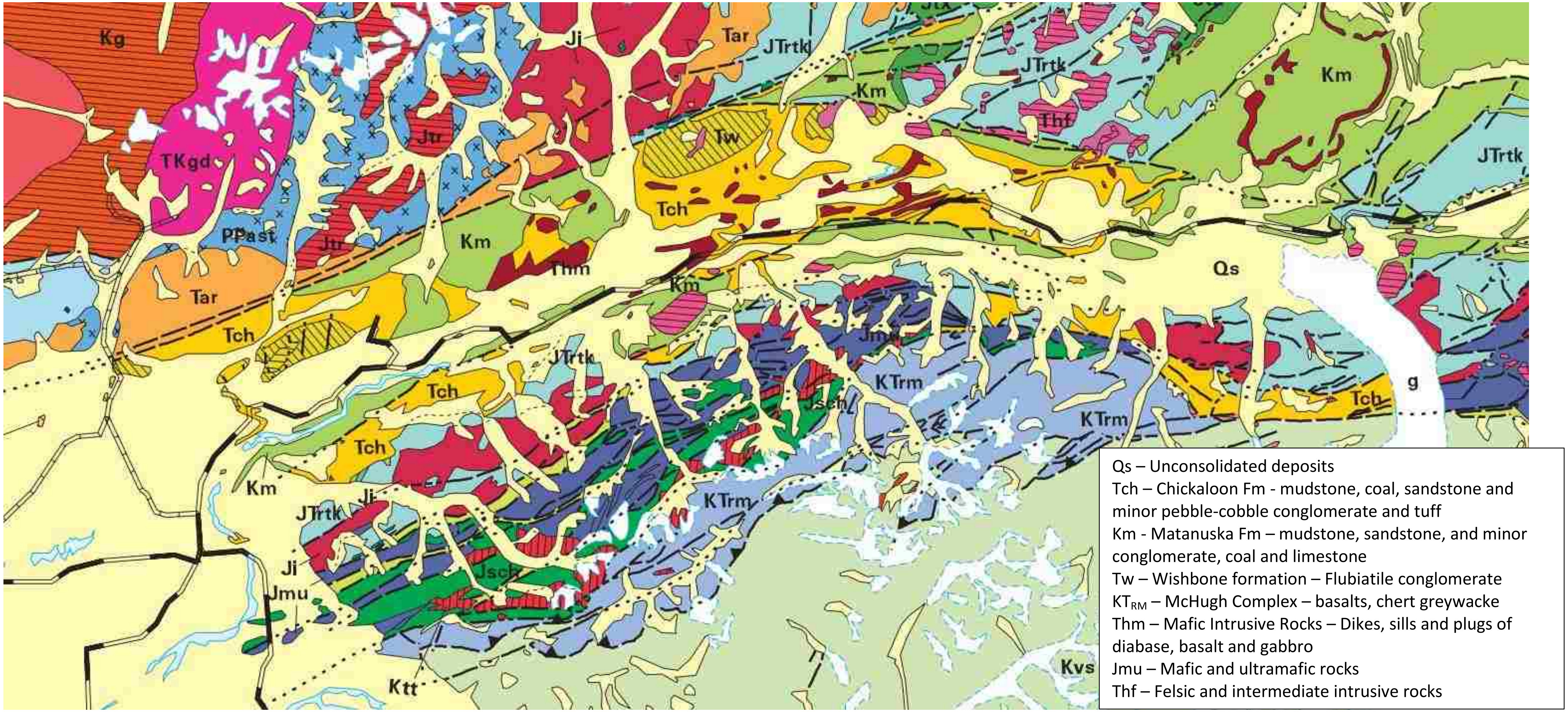

Qs – Unconsolidated deposits
Tch – Chickaloon Fm - mudstone, coal, sandstone and minor pebble-cobble conglomerate and tuff
Km - Matanuska Fm – mudstone, sandstone, and minor conglomerate, coal and limestone
Tw – Wishbone formation – Flubiatile conglomerate
KT_{RM} – McHugh Complex – basalts, chert greywacke
Thm – Mafic Intrusive Rocks – Dikes, sills and plugs of diabase, basalt and gabbro
Jmu – Mafic and ultramafic rocks
Thf – Felsic and intermediate intrusive rocks

Figure 2.12 General geology of the Glenn Highway area. Glenn Highway is the dotted line in the top third of the map. (Wilson, Dover, Bradley, Weber, Bundtzen, & Haeussler, 1998)

2.3.3 Focus sites within Glenn Highway

Two sites along Glenn Highway, mileposts 87 and 85.5 were more fully examined and used in the development of the RAI class and energy ratings. These sites were chosen because there was lidar coverage for two years of scans. In addition, these were structurally and compositionally different showing a wider range of geologic conditions and there was a range of change from year to year.

Milepost 87 seen in Figure 2.13 is part of the Chickaloon formation and consists of soft sedimentary rock overridden by hard mafic sills. The contrast between strengths of these units has caused differential erosion forming overhangs within the site. The mafic sills have two major joint sets, one dipping at approximately 50 degrees with a dip direction of 195 degrees and the other dipping at approximately 40 degrees with a dip direction of 5 degrees. The overall slope and direction of the site is approximately 58 degrees slope with a direction of east to west. The stereonet for this site can be seen in Figure 2.14.

Milepost 85.5 is an outcrop of fine-medium grained grey and tan sandstone of the Chickaloon formation, Figure 2.15. This area has been moderately weathered and three joint sets are visible Figure 2.15. The dip and direction of these sets are approximately: 60 degrees dip, 90 degrees dip direction; 85 degrees dip, 0 degrees dip direction and 30 degrees dip, 200 degrees dip direction. The overall slope and direction of this site is 60 degrees slope with a northeast to southwest direction.

Figure 2.13 (above): Chickaloon formation at Milepost 87 along Glenn Highway. This site has soft sedimentary rock overridden by hard mafic sills causing differential erosion resulting in overhangs within the slope.

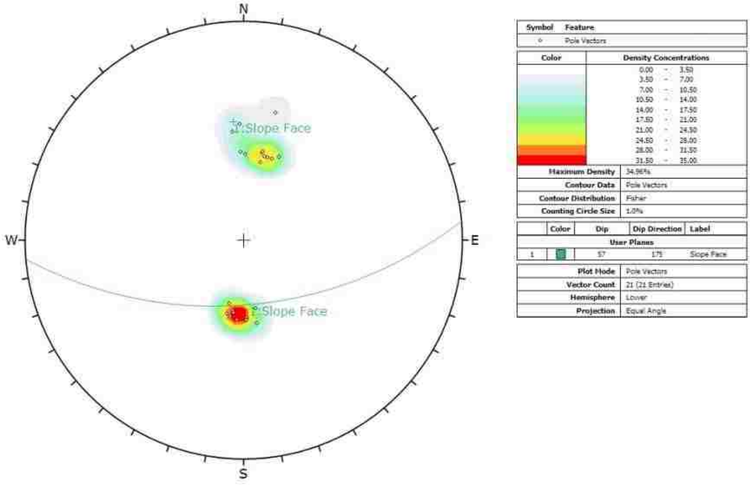

Symbol	Feature
◇	Pole Vectors

Color	Density Concentrations
⬜	0.00 - 3.50
⬜	3.50 - 7.00
🟦	7.00 - 10.50
🟦	10.50 - 14.00
🟩	14.00 - 17.50
🟩	17.50 - 21.00
🟩	21.00 - 24.50
🟨	24.50 - 28.00
🟧	28.00 - 31.50
🟥	31.50 - 35.00
Maximum Density	34.96%
Contour Data	Pole Vectors
Contour Distribution	Fisher
Counting Circle Size	1.0%

	Color	Dip	Dip Direction	Label
User Planes				
1	🟩	57	175	Slope Face

Plot Mode	Pole Vectors
Vector Count	21 (21 Entries)
Hemisphere	Lower
Projection	Equal Angle

Figure 2.14 (left): Stereonet representing the two joint sets found at milepost 87. The slope face itself runs nearly east west with a slope of 58 degrees. The two joint sets are approximately 50 degrees dip with dip direction of 195 degrees and 40 dip with a dip direction of 5 degrees.

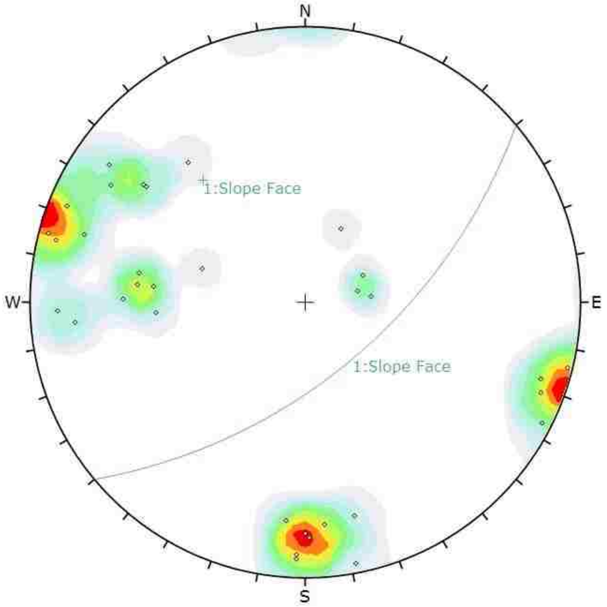

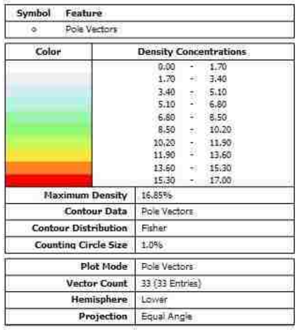

Symbol	Feature
○	Pole Vectors

Color	Density Concentrations
⬜	0.00 - 1.70
⬜	1.70 - 3.40
🟦	3.40 - 5.10
🟦	5.10 - 6.80
🟩	6.80 - 8.50
🟩	8.50 - 10.20
🟨	10.20 - 11.90
🟨	11.90 - 13.60
🟧	13.60 - 15.30
🟥	15.30 - 17.00

Maximum Density	16.85%
Contour Data	Pole Vectors
Contour Distribution	Fisher
Counting Circle Size	1.0%

Plot Mode	Pole Vectors
Vector Count	33 (33 Entries)
Hemisphere	Lower
Projection	Equal Angle

Figure 2.15 (above): Sandstones from Chickaloon formation at Milepost 85.5 along Glenn Highway.

Figure 2.16 (left): Stereonet representing the three joint sets found at milepost 85.5. The slope face itself runs nearly northeast to southwest with a slope of 60 degrees. The three joint sets are approximately 60 degrees dip with dip direction of 90 degrees, 85 degree dip with a dip direction of 0 degrees and30 dip with a dip direction of 200 degrees.

2. 4 Climate of the Study Region

Table 2.1 summarizes the climate of the Parks Highway and Glenn Highway regions. Weather station "Healy 2 NW" is located near Parks Highway, while the "Matanuska" station is located near Glenn Highway. Note that the local climate varies between the two sites. The significant climatic factors controlling the hillslope erosional processes are freeze-thaw days and precipitation. Freeze thaw days are defined as the difference between the amount of days where the diurnal temperature varies above and below 0° C (32° F). As freeze-thaw days are indicative of temperature cycling, erosion would be generally expected to increase with the number of freeze-thaw days. The effects of precipitation depend upon both the intensity and duration of an event; however hillslope erosion is generally proportional to the mean yearly precipitation.

Table 2.1: Climatological Data (Western Regional Climate Center)

	Healy 2 NW	**Matanuska AES**
Dates of Records	1976-2012	1949-2012
Elevation	45.4 m (149 feet)	4.6 m (15 feet)
Average Yearly Max Temperature	4.2° C (39.6° F)	37.5° C (44.7° F)
Average Yearly Min Temperature	-6.5° C (20.3° F)	-3° C (26.5° F)
Average Yearly Mean Temperature (F)	-1.2° C (29.9° F)	2° C (35.6° F)
Annual Days of Max Temp under 0° C (32° F) (days)	121	96.7
Annual Days of Min Temp under 0° C (32° F) (days)	212	203
Freeze/Thaw Days (Min – Max under 0° C (32° F))	91	106.3
Mean Yearly Precipitation (inches)	37.5 cm (14.75 inches)	38.8 cm (15.3 inches)
Mean Yearly Total Snowfall (inches)	194.8 cm (76.7 inches)	121.2 cm (47.7 inches)
Annual Days with at least .025 cm (.01 inches) precipitation	100	96

3. Current state of slope classification

A classification system is an organization of characteristics that aids in the comparison, quantification and/or categorization of a topic. Classification systems are common in many fields and allow non-experts to better understand a topic. Additionally, they provide a concise description that is understood by all using the system. These systems also organize a subject into a useful pattern so that it can be better studied (Singh & Goel, 2011).

In rock slope engineering, rock classification systems are used to understand slope processes and identify, factors contributing to instability. Set up by subject experts, rock slope classification systems help distill the complexities of slopes into understandable units, serving as tools to assist users in evaluating slope stability. Rock classification systems facilitate communication among the different parties who design and construct structures by providing a common language and understanding (Singh & Goel, 2011).

3.1 Slope classification systems used in this project

Table 3.1 summarizes several rock mass and/or slope classification systems that were considered for use in this project. This selection of classification systems was based on accessibility to information about the system, and if the system had potential for remote application and systems that were in use and commonly known. To compare the systems, the attributes of each system were first categorized and assessed based on means of measurement, nature of the attribute (quantitative or qualitative), availability of required information, and use in practice [especially at the Alaska Department of Transportation (DOT)]. Based on this assessment, the Rockfall Hazard Rating System and Rock Slope Deterioration were judged to be the systems best suited for the research.

Table 3.1 Rock Slope Classification Systems

System	Main Use
Rock Quality Designation (RQD) (Deere and Deere 1988)	Tunneling (used as parameter)
Rock Mass Rating (Bieniawski 1973)	Tunneling
Rock Mass Quality Q-System (Barton, Lien and Lunde 1974)	Tunneling
Rock Mass Index (Palmstrom 1996)	Tunneling
Slope Mass Rating (Romana 1985)	Rock Slope Classification
Geologic Strength Index (Hoek and Brown 1997)	Rock Slope Classification/Tunneling
Rockfall Hazard Rating System (Pierson 1991)	Rock Slope Classification
Rock Slope Deterioration (Nicolson 2004)	Classify and mitigate erosional features in slopes

3.2 Rockfall Hazard Rating System (RHRS)

Rock-fall Hazard Rating System (RHRS) as a way to assess rock slopes easily and have a metric to understand slopes and compare them to each other across a system of assets. Larry Pierson first developed the system in 1984 for the Oregon DOT, and later in 1991, detailed the system in a design report. The original system covered 10 aspects rated 0 to 100 as summarized in Table 3.2 (Pierson, 1991). The scoring is exponentially scaled to more heavily weight issues that might result in failure. These attributes are flexible, allowing a DOT to add attributes that are more focused to their area or concerns and drop those that either do not apply or are not seen as major problems. The system is widely used throughout the United States with at least half the (Huang, Darrow, & Calvin, 2009) states adopting some form of it. The system has two main focuses, hazard and risk. In using this system, only the attributes related to the hazard were used; attributes relating to the risk of vehicles traveling on the roads were ignored because factors such as usage of the road and percent sight distance are better calculated through means other than lidar. Although attributes which were later added to subsequent versions of this system were looked at, this paper will only consider those that were in the original system.

3.2.1 Uses in Department of Transportations (DOTs)

Many Department of Transportations (DOTs) have adapted the published RHRS to their needs by adding, modifying or deleting parameters according to their state's needs and setting. A summary of several state-specific RHRS is found in Table 3.3 (Huang, Darrow, & Calvin, 2009).

In the original version of the RHRS by Pierson (1991), hazard and risk pertaining to a slope were considered together. Later the system evolved such that the hazard and risk were considered separately. This is true of many of the state RHRS, including the system used for this project, which is based on the Alaska DOT system modified from the Unstable Slope Management Program report (Huang et al 2009).

3.3.2 Selection of RHRS

A primary reason for this system being chosen was its common use by many state DOTs. The system has a history of use by the Alaska DOT and remains the basis of their current unstable slope management program.

3.3.3 Evaluation of the RHRS

The RHRS provides a standardized way to rate rock slopes in a manner that scores more critical items at a higher weight, thus emphasizing the possibility these factors may govern stability. The factors can be divided into risks: (1) possibility of loss, and (2) hazard, the possibility of something happening that will result in a loss. For the current phase of the research, hazard was focused on because it most closely related to the actual failure of slopes.

Table 3.2: RHRS Original System developed by Pierson for the use of Oregon Department of Transportation. (Pierson 1991)

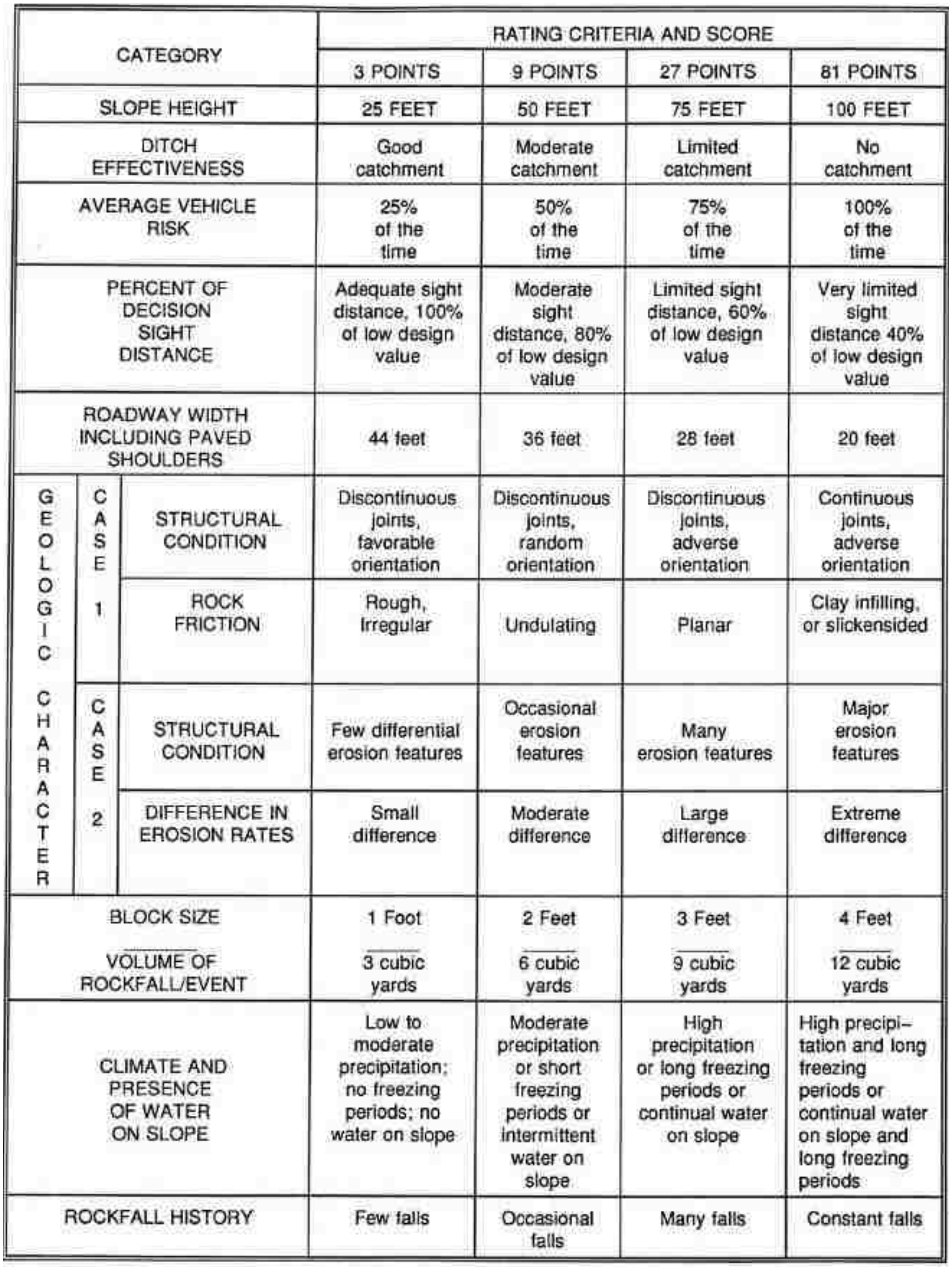

CATEGORY			RATING CRITERIA AND SCORE			
			3 POINTS	9 POINTS	27 POINTS	81 POINTS
SLOPE HEIGHT			25 FEET	50 FEET	75 FEET	100 FEET
DITCH EFFECTIVENESS			Good catchment	Moderate catchment	Limited catchment	No catchment
AVERAGE VEHICLE RISK			25% of the time	50% of the time	75% of the time	100% of the time
PERCENT OF DECISION SIGHT DISTANCE			Adequate sight distance, 100% of low design value	Moderate sight distance, 80% of low design value	Limited sight distance, 60% of low design value	Very limited sight distance 40% of low design value
ROADWAY WIDTH INCLUDING PAVED SHOULDERS			44 feet	36 feet	28 feet	20 feet
GEOLOGIC CHARACTER	CASE 1	STRUCTURAL CONDITION	Discontinuous joints, favorable orientation	Discontinuous joints, random orientation	Discontinuous joints, adverse orientation	Continuous joints, adverse orientation
		ROCK FRICTION	Rough, Irregular	Undulating	Planar	Clay infilling, or slickensided
	CASE 2	STRUCTURAL CONDITION	Few differential erosion features	Occasional erosion features	Many erosion features	Major erosion features
		DIFFERENCE IN EROSION RATES	Small difference	Moderate difference	Large difference	Extreme difference
BLOCK SIZE VOLUME OF ROCKFALL/EVENT			1 Foot 3 cubic yards	2 Feet 6 cubic yards	3 Feet 9 cubic yards	4 Feet 12 cubic yards
CLIMATE AND PRESENCE OF WATER ON SLOPE			Low to moderate precipitation; no freezing periods; no water on slope	Moderate precipitation or short freezing periods or intermittent water on slope	High precipitation or long freezing periods or continual water on slope	High precipitation and long freezing periods or continual water on slope and long freezing periods
ROCKFALL HISTORY			Few falls	Occasional falls	Many falls	Constant falls

Table 3.3: Rockfall Hazard Slope Characteristics by Department of Transportation illustrating the differences between each system. (Huang et al 2009)

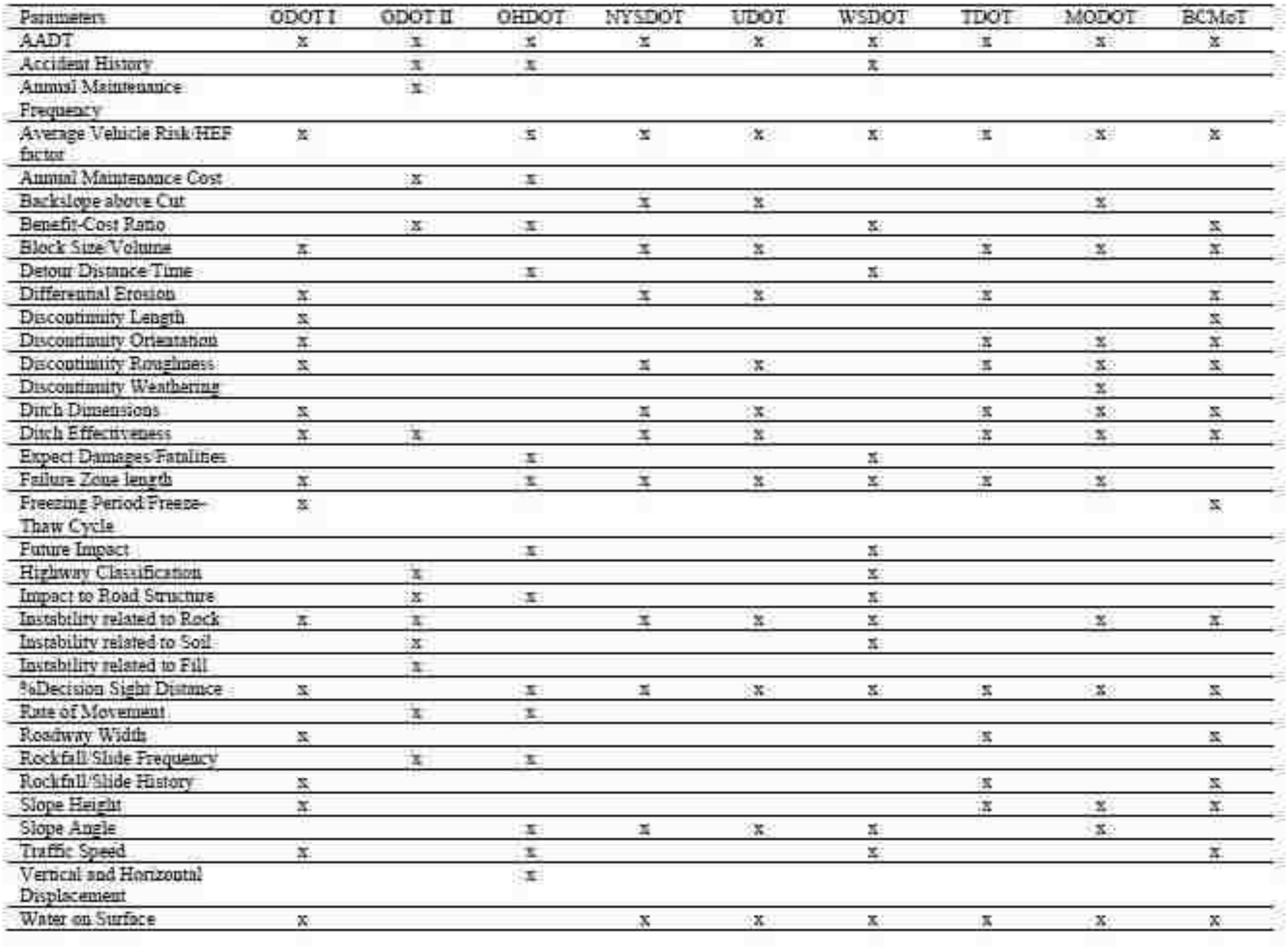

Parameters	ODOT I	ODOT II	OHDOT	NYSDOT	UDOT	WSDOT	TDOT	MODOT	BCMoT
AADT	x	x	x	x	x	x	x	x	x
Accident History		x	x			x			
Annual Maintenance Frequency		x							
Average Vehicle Risk/HEF factor	x		x	x	x	x	x	x	x
Annual Maintenance Cost		x	x						
Backslope above Cut				x	x			x	
Benefit-Cost Ratio		x	x			x			x
Block Size/Volume	x			x	x		x	x	x
Detour Distance/Time			x			x			
Differential Erosion	x			x	x		x		x
Discontinuity Length	x								x
Discontinuity Orientation	x						x	x	x
Discontinuity Roughness	x			x	x		x	x	x
Discontinuity Weathering								x	
Ditch Dimensions	x			x	x		x	x	x
Ditch Effectiveness	x	x		x	x		x	x	x
Expect Damages/Fatalities			x			x			
Failure Zone length	x		x	x	x	x	x	x	
Freezing Period Freeze-Thaw Cycle	x								x
Future Impact			x			x			
Highway Classification		x				x			
Impact to Road Structure		x	x			x			
Instability related to Rock	x	x		x	x	x		x	x
Instability related to Soil		x				x			
Instability related to Fill		x							
%Decision Sight Distance	x		x	x	x	x	x	x	x
Rate of Movement		x	x						
Roadway Width	x						x		x
Rockfall/Slide Frequency		x	x						
Rockfall/Slide History	x						x		x
Slope Height	x						x	x	x
Slope Angle			x	x	x	x		x	
Traffic Speed	x		x			x			x
Vertical and Horizontal Displacement			x						
Water on Surface	x			x	x	x	x	x	x

One limitation of this system is that it is designed to be used by personnel in the field. Therefore, most of the attributes are assigned subjectively. Another limitation is that the system has categorical attributes that many of the slope sections in our study did not fit into very well (e.g., structural conditions for some sites did not specifically fit into one of the categories). This can be challenging, especially when looking at the structural condition of the slope. Expert evaluation needs to be made for such situations.

3.4 Rockslope Deterioration Assessment (RDA)

The Rock slope Deterioration Assessment (RDA) was developed by Nicholson (Nicholson, 2004) as a way to assess and remediate rock slopes. This system has three stages: (1) classification, (2) rock mass type and (3) remediation. Only the first of these three stages (classification) was used for this project. The system has four main factors and nine adjustment factors that can be expanded for special circumstances such as earthquake failure. Three of the main factors, fracture spacing, fracture aperture and rock strength, use a graph to determine the RDA Rating as seen in Figure 3.1. The fourth, weathering, uses subjective descriptions as seen in Table 3.4. In Table 3.5, a list of the adjustment factors is presented.

This system is not widely used, but is seen as a complement to the RHRS because the RHRS focuses mainly on structural aspects of rock slopes and the RDA focuses mostly on the erosional aspects, although both consider both aspects, for complete coverage both need to be fully considered.

3.4.1 Uses of RDA

The RHRS System focused more on the structure of the slope, while the RDA system examined erosional processes and was a good complement for the RHRS. The RDA is not designed to be an inventory system, but rather to look at individual slopes and assess them for potential failure risks.

3.4.2 Analysis of the RDA

The RDA system fills the partial void with regard to the erosional processes in the RHRS that are a major factor in this project. Most of the categories are easily measured, and there is flexibility in the system to fit the need of the assessment. This system has not been used on large scale, however, and is not intended to be up-scaled for inventory proposes. This makes some of the implementation difficult, and attributes need to be slightly modified to meet our needs.

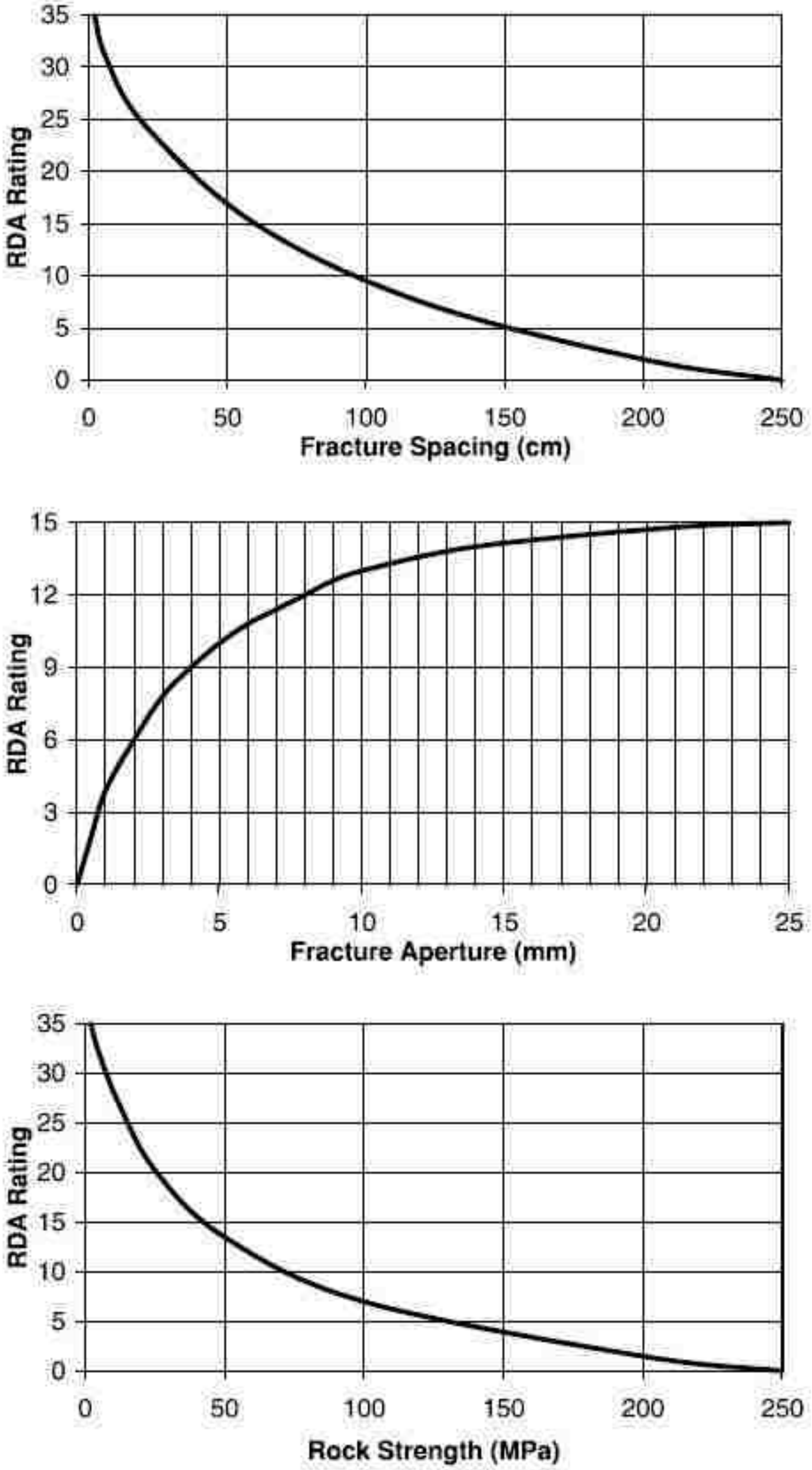

Figure 3.1 RDA Main Factors charts to determine the score of fracture spacing, fracture aperture and rock strength (Nicolson 2004).

Table 3.4: Table to determine the RDA weathering score (Nicolson 2004).

Grade	Material description	Rating
Fresh	Unchanged from original state.	0
Slightly weathered	Slightly discoloured; slight weakening.	5
Moderately weathered	Weakened in association with penetrative discolouration.	10
Highly weathered	Large pieces (eg NX drill core) cannot be broken by hand; does not readily slake when imersed.	14
Completely weathered	Considerably weakened; slakes readily; original texture retained.	15
Residual soil	No original fabric or texture remains (soil).	n/a

Table 3.5: Adjustment factors for the RDA. Each factor has a different weight either adding to or subtracting from the score (Nicolson 2004).

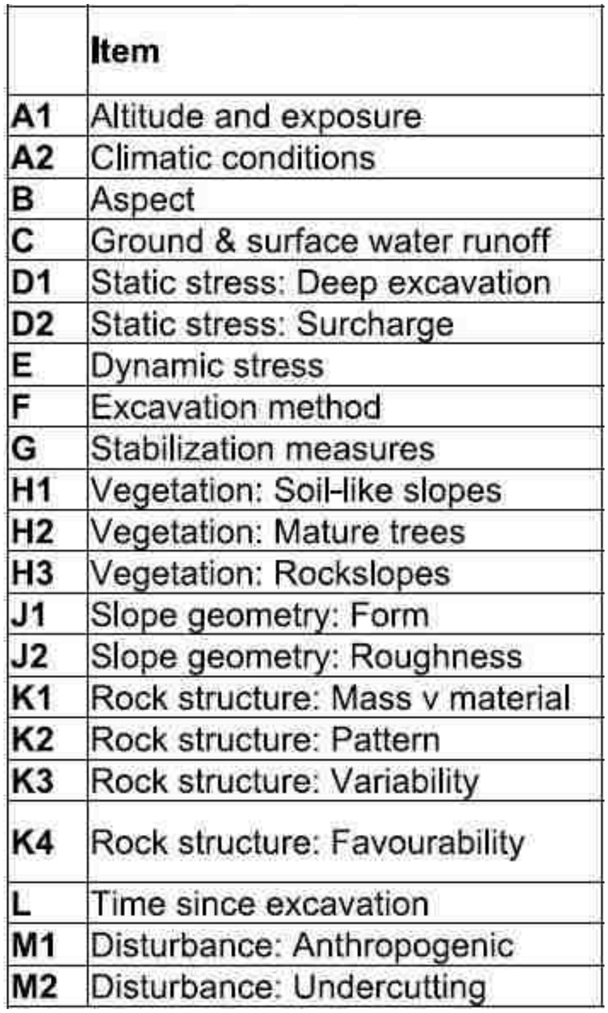

	Item
A1	Altitude and exposure
A2	Climatic conditions
B	Aspect
C	Ground & surface water runoff
D1	Static stress: Deep excavation
D2	Static stress: Surcharge
E	Dynamic stress
F	Excavation method
G	Stabilization measures
H1	Vegetation: Soil-like slopes
H2	Vegetation: Mature trees
H3	Vegetation: Rockslopes
J1	Slope geometry: Form
J2	Slope geometry: Roughness
K1	Rock structure: Mass v material
K2	Rock structure: Pattern
K3	Rock structure: Variability
K4	Rock structure: Favourability
L	Time since excavation
M1	Disturbance: Anthropogenic
M2	Disturbance: Undercutting

4. Remote Processing of Classification Systems

4.1 Slope Change using RDA and RHRS systems

To understand what is driving the slope changes, an investigation into classification systems and their required factors was performed using the Rockslope Deterioration Assessment (RDA) and the Rockfall Hazard Rating System (RHRS). This helped to establish a baseline behavior of the slopes and to characterize the important factors leading to failure.

Not all of the factors that are measured in the RDA and RHRS system are readily measured with lidar. The two systems are flexible in that they allow factors to be removed or added. The factors used in this characterization of slopes needed to be measurable remotely using lidar, photographs, Google Earth Street View, and online databases.

Some of the factors were easy to measure from the lidar and a digital elevation model (DEM) derived from the lidar data. Other factors were assigned based on a relative scale because exact measurements were not possible to make from photographs. Other factors were assumed or disregarded in the final iteration of the analysis because there was no significant difference between sites for example excavation methods. One factor— the compressive strength of the rock— was not possible to measure remotely. For this factor, assumptions were made using the type of rock until a second field study was be conducted in August 2013 and measurements were taken with a Schmidt Hammer (Goudie, 2006) (See Appendix B). A complete history of rock falls does not exist to support assignment of a rock fall history factor; therefore, assumptions were made when assigning this parameter by looking at talus piles and debris in ditches. Table 4.1 summarizes the factors and how they were measured.

Table 4.1 Factors and how they were measured remotely for this project.

Factor	Data Summary
Altitude	Geographic Information Systems (GIS) using Digital Elevation Models (DEM) maps
Aspect	GIS using DEM maps
Rock Weathering	From photographs, Google Earth, lidar
Stabilization and Protective measures	Lidar and photographs
Vegetation	Lidar and photographs
Slope Height	GIS and lidar
Ditch Effectiveness	Lidar software. Note: Measured width and depth of ditches and used a relative scale to rate.
Roadway width	GIS and lidar
Rockfall History	Evidence in pictures and lidar (Maintenance and Operation records were not available)
Aperture	Photographs on a relative scale and in field
Fracture Spacing	Lidar software. Note: had to hand marked the discontinuities. Also measured in person and from photographs for relative measures.
Rock Compressive Strength	Taken in field via Schmidt Hammer
Static and Dynamic Stresses	Assumed not to change in an area because traffic patterns were same for whole length of road.
Excavation methods	Assumed the same between all cuts because historical record are difficult to obtain
Climate/Presence of water	Assumed same in each study area because of proximity between sites
Annual Freeze/Thaw Days	Online databases from NOAA
Maintenance Frequency	Assumed to be the same, did not find information on individual slopes (Maintenance and Operation records were not available)

4.2 Alaska Unstable Slope Management Report Scores

The sites that were examined for this study were not the identical sites from the Alaska Unstable Slope Management Report (USMR) [Landslide Technology R and M Consultants, 2010] Because of this, a direct comparison is not possible. THE USMR though can shed some light on the overall picture seen by Alaska Department of Transportation. For the records obtained, each site was looked at only one day, October 2, 2010 for Glenn Highway and October 5, 2010 for Parks Highway. The following table summarizes the findings using the attributes determined in Table 4.2a and b.

Table 4.2a: Summary of Glenn Highway Unstable Slope management report for 2 October 2010

	Glenn Highway - 2 October 2010						
Site	MP 84.67	MP 84.7	MP 85.4	MP 85.7	MP 86.4	MP 86.8	MP 87
Structural Condition	0	20	35	60	40	20	27
Rock Friction/Diff Erosion	0	20	30	40	40	27	20
Ditch Effectiveness	0	50	27	40	50	60	27
Rockfall history	0	20	27	40	27	40	40
Slope Height	22	9	3	100	100	100	4
Block Size	0	47	47	100	100	100	39
Total	22	166	169	380	357	347	157

Table 4.2b: Summary of Parks Highway Unstable Slope management report for 5 October 2010

	Parks Highway - 5 October 2010			
Site	GG238.25	GG238.35	GG239.25	GG239.6
Structural Condition	0	0	81	81
Rock Friction/Diff Erosion	0	0	81	81
Ditch Effectiveness	0	0	27	3
Rockfall history	0	0	81	100
Slope Height	17	3	27	100
Block Size	0	0	100	81
Total	17	3	397	446

These results show a variation over the two sites. Average Glenn Highway scores with these attributes was 228 points and for Parks highway 215, but the variation between areas in the two sites is great. Because the sites did not exactly match and it was desired to have a finer resolution of scoring, the RHRS was determined using the remote process in the following section.

4.3 RHRS Procedure

RHRS is a relatively simple method to carry out. Each attribute has four categories, which scale with worsening conditions. An example of this method was done on a second field trip to the sites and used as a basis for some of the measurements.

For the remote the following procedures were followed:

1. In ArcGIS, the area is sectioned off into compartments of a certain width based on a centerline using the TopCat toolbox (Olsen et al., 2012)
2. Calculate the zonal statistics of each compartment on the DEM
3. With this find the height of each slope (the range)
4. Estimate via photographs the structural condition, rock friction or differential erosion, rockfall history and block size
5. Measure the ditch widths on lidar point clouds
6. Sum ratings to give a RHRS score

The final attribute list can be seen in Table 4.3. Several attributes were omitted from the original Pierson (1991) system so the maximum possible score was 600.

Table 4.3 Final RHRS Factors used for remote classification for this project. (revised from Pierson 1991)

Attribute	Source
Structural Condition	Onsite analysis/Photograph analysis
Rock Friction/Differential Erosion	Onsite analysis (This could be assumed by photographs, but not accurately)
Ditch Effectiveness	Measured from lidar, looked at relative volume. Onsite visit.
Rockfall History	Looked at Talus piles, evidence in photographs, onsite
Slope Height	Measured within the lidar point cloud
Block Size	Onsite/lidar, on Parks Highway there is no real “blocks”

4.4 Results of the RHRS

Figures 4.1 and 4.2 are examples of the final rated slopes in compartments of 10 m width for Glenn Highway and Parks Highway respectively and Table 4.4 is the respective scoring. There is a distinguishable difference between the two areas rated. Looking at the Alaska Unstable Slope Management Report (USMR) for sites near each of these, there would be an expectation for both to receive a mix of low and high scores. This is not the case especially for the Glenn Highway section. Part of this is because of the areas chosen for analysis. These depended on the first reconnaissance photographs and notes, and all some of the sites that were not covered through in this visit would have given different and higher scores.

Of the two sites, Parks highway was dominated by two factors, height of slope and rockfall history. These areas are constantly eroding and have large catchments to hold the material that comes off the slope on a regular basis. The analyzed areas in Glenn Highway were areas where there was no dominating feature. The only significant contributor to any of the sites raising the score was ditch effectiveness in MP 85.5.

Over all this is a good method for a general understanding of the processes that are occurring on a slope.

Figure 4.1 Glenn Highway sites scored with RHRS using remote sensing technique described in section 4.2

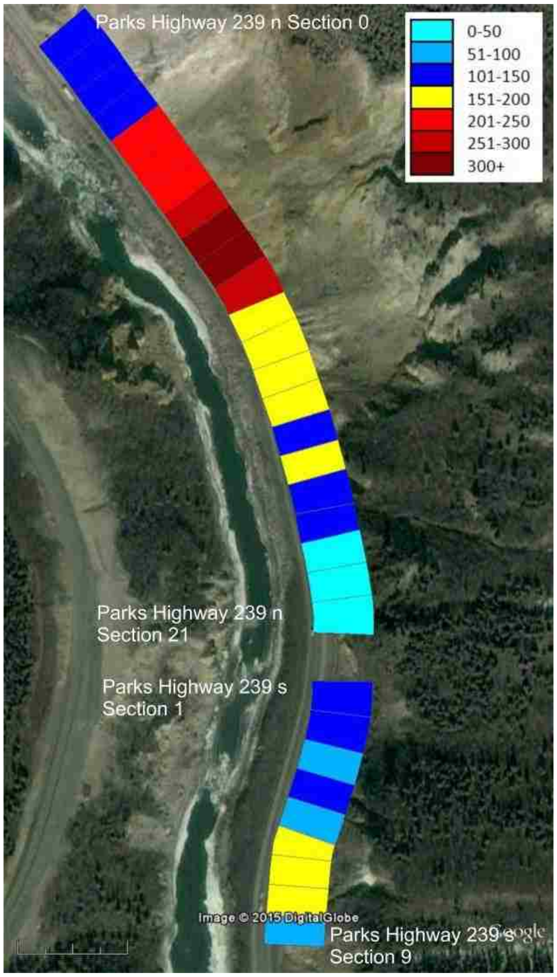

Figure 4.2 Parks Highway MP 239.5n section scored with RHRS using remote sensing technique described in section 4.

Table 4.4 Results of remote RHRS analysis

Parks Highway MP 239.5s									
Section	1	2	3	4	5	6	7	8	9
Structural Condition	18	18	3	3	3	18	9	9	9
Rock Friction/Diff Erosion	27	18	18	20	18	50	50	81	20
Ditch Effectiveness	9	9	9	9	9	9	9	9	9
Rockfall history	81	81	27	81	27	81	81	81	50
Slope Height	3	3	3	3	3.7	3.7	3.7	3.7	3.7
Block Size	3	3	3	3	3	3	3	3	3
Total	141	132	63	119	63	164	155	186	94

	Parks Highway MP 239.5n										
Section	0	1	2	3	4	5	6	7	8	9	10
Structural Condition	3	9	9	9	27	27	27	27	27	27	27
Rock Friction/Diff Erosion	9	9	9	9	27	27	27	27	81	81	27
Ditch Effectiveness	3	3	3	3	3	3	3	3	3	3	3
Rockfall history	27	18	27	9	81	81	81	81	81	81	27
Slope Height	81	81	81	81	81	81	81	81	81	81	81
Block Size	27	27	9	9	27	27	27	81	81	81	50
Total	150	147	138	120	246	246	246	300	354	354	215

	Parks Highway MP 239.5n										
Section	11	12	13	14	15	16	17	18	19	20	21
Structural Condition	27	27	18	27	9	9	3	3	3	3	3
Rock Friction/Diff Erosion	27	27	27	27	9	27	9	9	9	3	3
Ditch Effectiveness	3	3	3	3	3	3	3	3	3	9	9
Rockfall history	27	18	18	18	27	27	18	18	9	3	3
Slope Height	81	81	81	81	81	81	81	81	5.8	5.8	5.8
Block Size	27	27	9	9	9	9	18	18	9	9	3
Total	192	183	156	165	138	156	132	132	38	32	26

Glenn Highway	85.5				86.9				87				
Section	0	1	2	3	0	1	2	3	0	1	2	3	4
Structural Condition	9	3	3	3	3	3	3	3	3	3	9	9	3
Rock Friction/Diff Erosion	9	9	9	9	3	3	3	3	9	9	9	9	9
Ditch Effectiveness	27	27	27	3	9	9	9	9	9	9	9	9	9
Rockfall history	3	3	3	3	9	9	9	9	3	3	3	3	3
Slope Height	1.6	1.6	1.6	1.6	3	3	3	3	1.6	1.6	1.6	1.6	1.6
Block Size	9	9	9	3	3	3	9	9	9	27	27	9	9
Total	58	52	52	22	30	30	36	36	34	52	58	40	34

4.5 RDA procedure

The RDA process can be of a finer resolution than the RHRS. Where the RHRS looks at overall slope conditions (e.g. in the case presented in the prior sections at 10 m sections), the RDA can look at individual features. This was found to be difficult to implement because point clouds of each attribute needed to be manually mapped. The first attempt of this process using as many attributes as possible was found to be too labor intensive (results are shown in Appendix C). The following procedure was established to rate the point clouds using the four main attributes.

4.5.1 Mapping of the RDA

The main process in this procedure was to map the individual attributes. Each attribute was determined through photographs, measurements on the point cloud or field measurements. Data was then transferred to the point cloud. Only the four main attributes were used and the adjustments were not considered. The following guidelines were used for each attribute.

Weathering

Weathering was determined along the guidelines established by Nicholson (2004) as seen in Table 4.5. The interpretation of these can be seen in Figure 4.3.

Table 4.5: Descriptions of weathering from RDA (Nicholson, 2004)

Grade	Material description	Rating
Fresh	Unchanged from original state.	0
Slightly weathered	Slightly discoloured; slight weakening.	5
Moderately weathered	Weakened in association with penetrative discolouration.	10
Highly weathered	Large pieces (eg NX drill core) cannot be broken by hand; does not readily slake when imersed.	14
Completely weathered	Considerably weakened; slakes readily; original texture retained.	15
Residual soil	No original fabric or texture remains (soil).	n/a

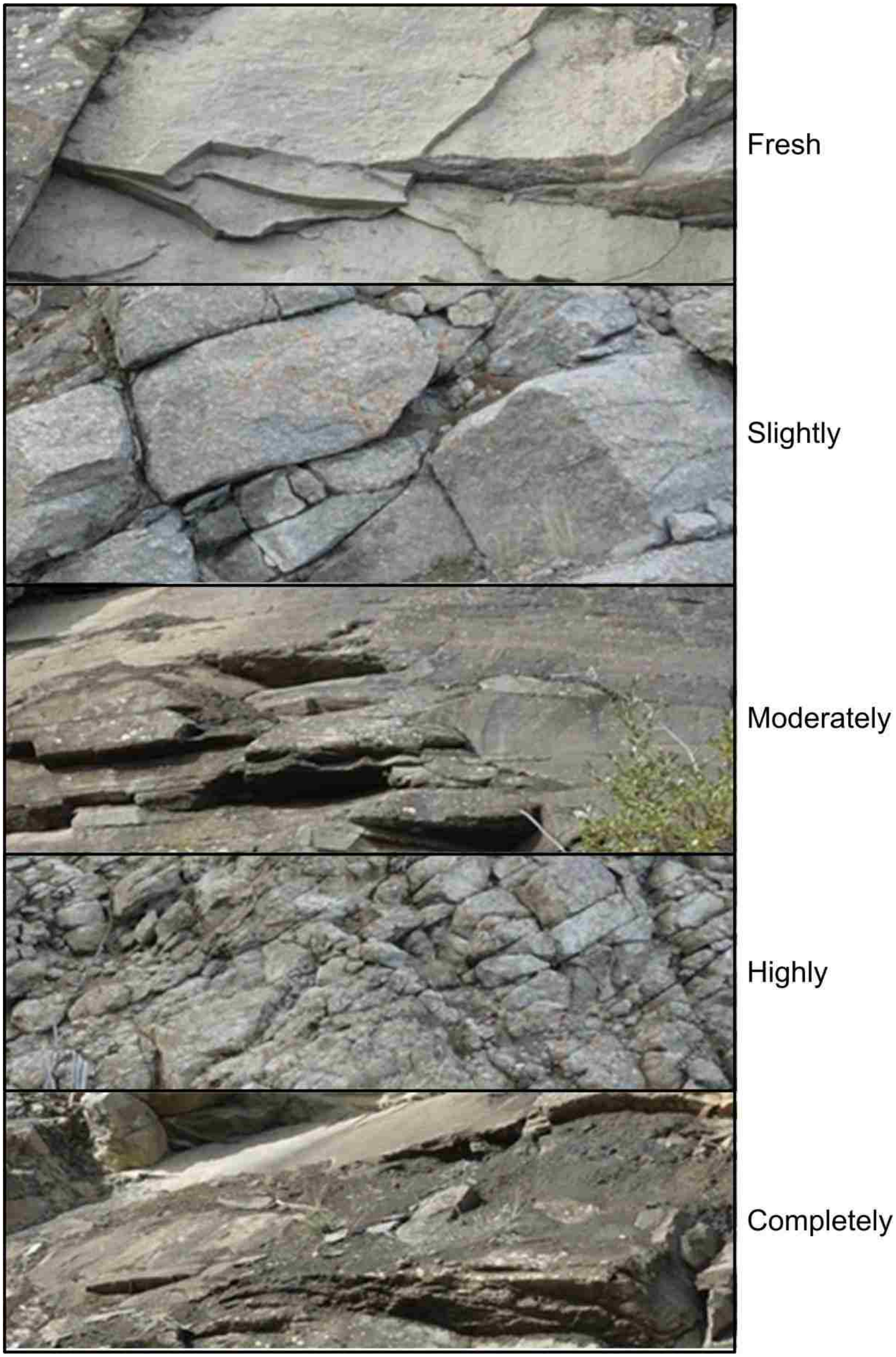

Figure 4.3: Examples of weathering taken from sites along Parks Highway and Glenn Highway

Fracture spacing

Fractures spacing was separated into five categories, Figure 4.4, and the mean of each category was used as the score. The spacing was measured using split FX software, Figure 4.5, and then generalized for an area.

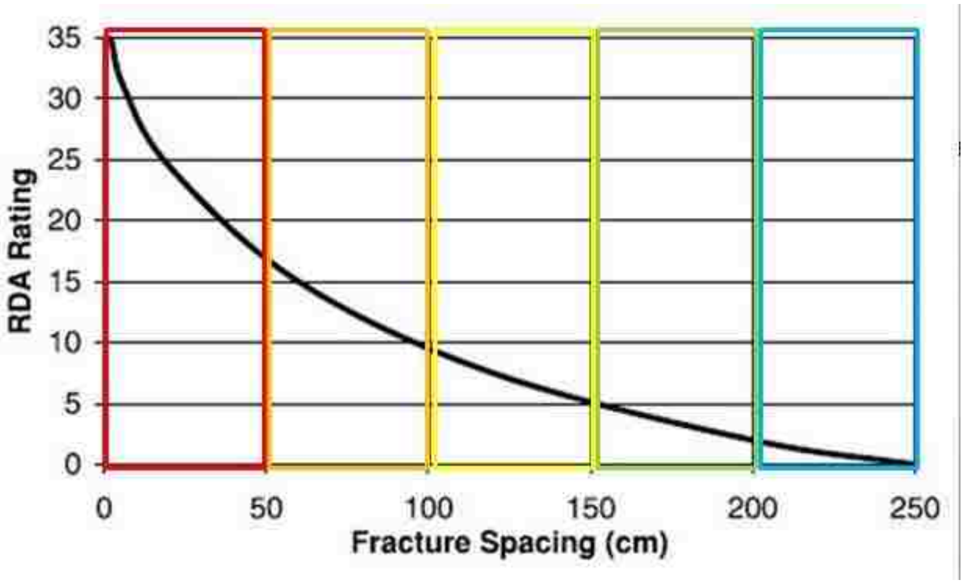

Figure 4.4: Generalization of the fracture spacing as used in the remote application of the RDA. Each color represents a different level. Scores used can be seen in Table 4.6 (Nicholson, 2004).

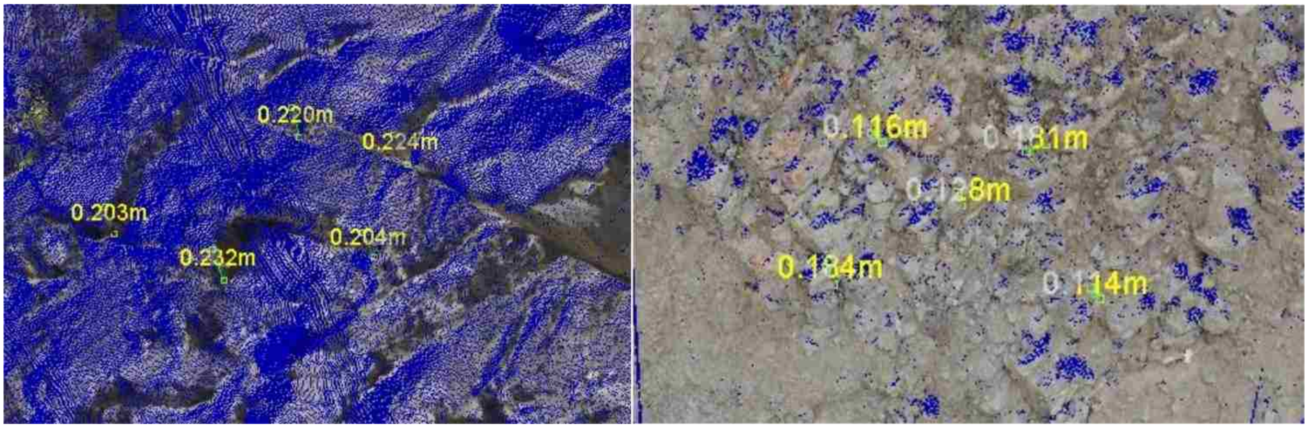

Figure 4.5: Examples of fracture spacing as measured in Split FX (Split Engineering LLC, 1997-2015). These measurements were also taken in the field. The final iteration was a generalization of the spacing that can be in Figure 4.4.

Fracture Aperture

Fracture aperture was split into three grades, loose, medium and tight as seen in Figure 4.6. These were determined visually as seen in Figure 4.7.

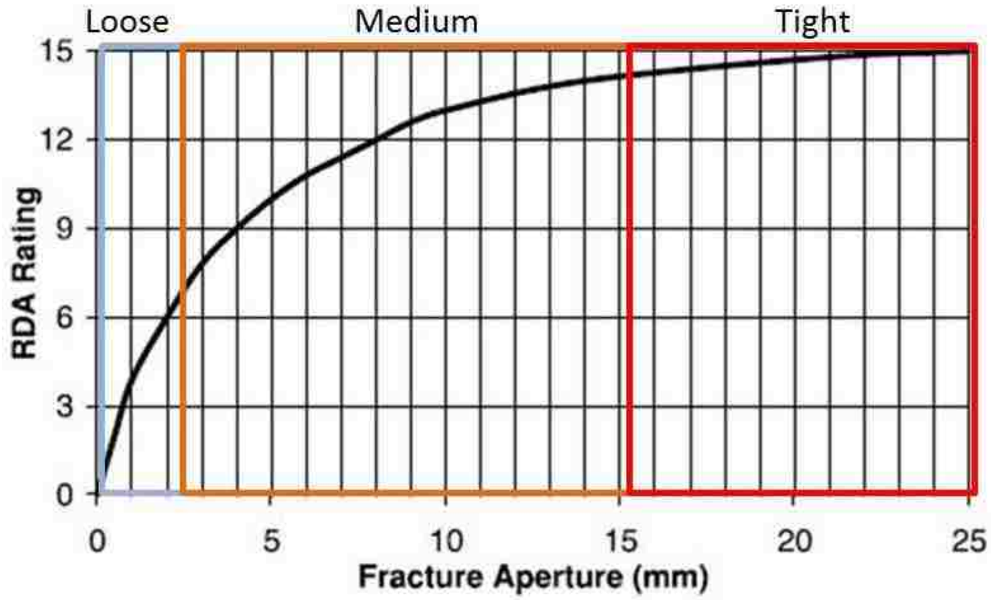

Figure 4.6: Generalization of the fracture aperture. Examples of each level, loose, medium and tight can be seen in Figure 4.7. (Nicholson, 2004)

Figure 4.7: Examples of the generalized levels of Fracture Aperture using examples from Glenn Highway and Parks Highway study areas.

Rock Strength

Rock strength was calculated with the use of Schmidt hammer measurements as described in Appendix B. The sites were then separated according to lithological units as shown in Figure 4.8.

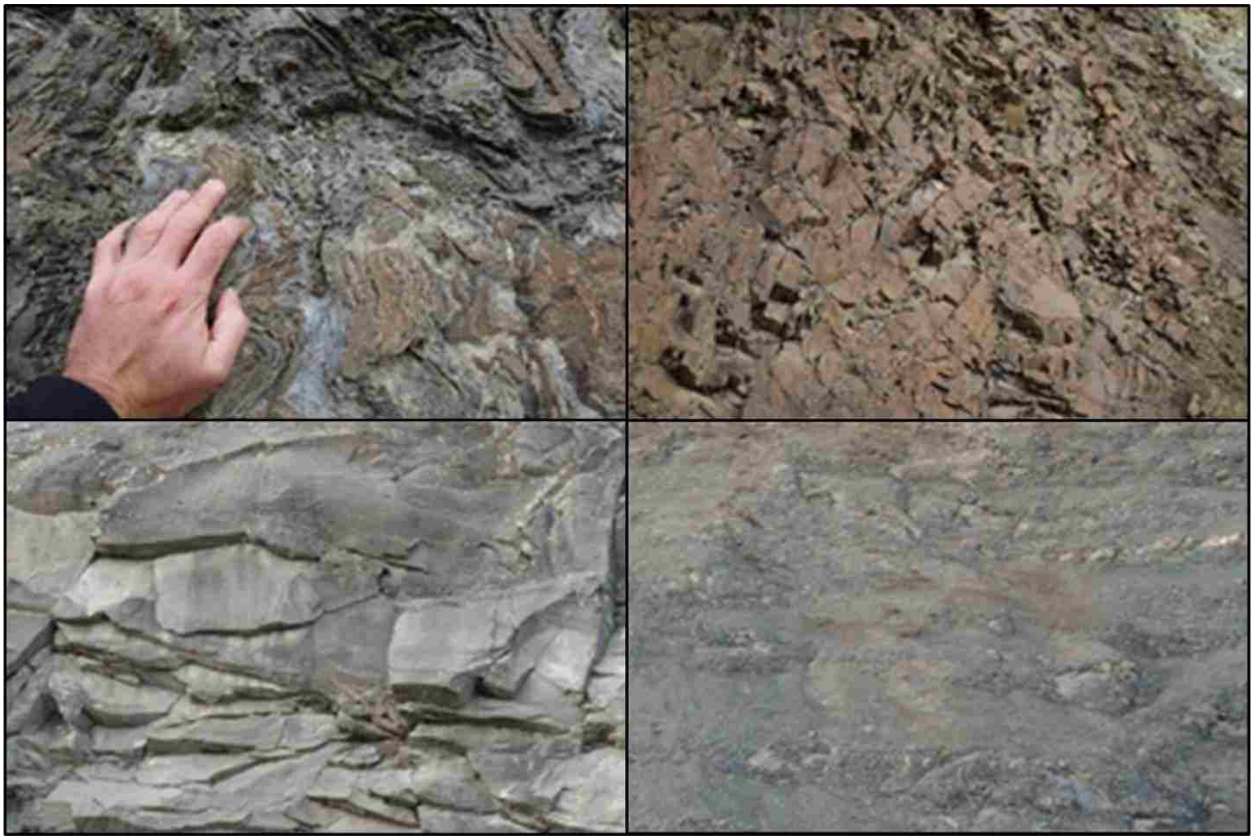

Figure 4.8: Top left, Healy Schist, top right: mafic intrusion along Parks highway, bottom left: sill intrusion along Glenn Highway and bottom right: carbonous rock from the Chickaloon formation.

RDA Values per class

Each grade was made into an individual point cloud which was given a RDA score. The clouds were combined to create a total RDA score. Table 4.6 describes the different clouds with their corresponding colors in Figure 4.9.

Table 4.6: RDA Values per class with description, color and RDA score. The following figures will use these colors as reference.

File Name	RDA Score	Color	Description
W_Completely	15	Red	Weathering Completely
W_Highly	14	Orange	Weathering Highly
W_Moderately	10	Yellow	Weathering Moderately
W_Slightly	5	Green	Weathering Slightly
W_Fresh	0	Blue	Weathering Fresh
W_Debris, W_Debris_Veg, W_Veg (or other form)	0	Gray or Black	Areas of debris or vegetation, sometimes there just won't be a point cloud for these areas
F_Debris	0	Gray or Black	Area of debris or veg…
F_50	25	Red	Fracture spacing 50 mm
F_100	10	Orange	Fracture spacing 100 mm
F_150	5	Yellow	Fracture spacing 150 mm
F_200	2.5	Green	Fracture spacing 200 mm
F_250	0	Blue	Fracture spacing 250 mm
A_Tight	5	Blue	Aperture tight
A_Med	12	Green	Aperture Medium
A_Loose	15	Red	Aperture Loose (Loose rocks)
G_Shale	32	Yellow	Chickaloon Shale/siltstone in LL
G_Sandstone	7	Pink	Sandstone in LL
G_Mudstone	9		Chickaloon Mudstone in LL
G_Schist	1	Yellow-green	Healy Schist in GG
G_Mafic	2	Purple	Mafic Intrusions in GG

4.5.2 Results of the RDA

This process does establish a slightly finer resolution cloud then the RHRS, but it is still is coarse in its nature and is time consuming to process. The areas that the RDA highlights as potential concern are those that are of differential erosion under the overhangs. This is good in that it is establishing these areas as potential problems, but it misses the overhangs which could potentially be a greater concern. Overall, besides the differential erosion areas, there are no outstanding features.

4.5.3 Discussion of classification methods

The remote application of these two classification systems as seen in the above sections both capture an overall sense of each of the classification systems although not a detailed one. The systems are able to show major areas that are of potential problems through these methods. But this is because of the domination of a few factors in the case of the RHRS and an emphasis on a particular feature in the

RDA. This being said, they both provide useful information to the users and allow focus on areas that would be potential concern.

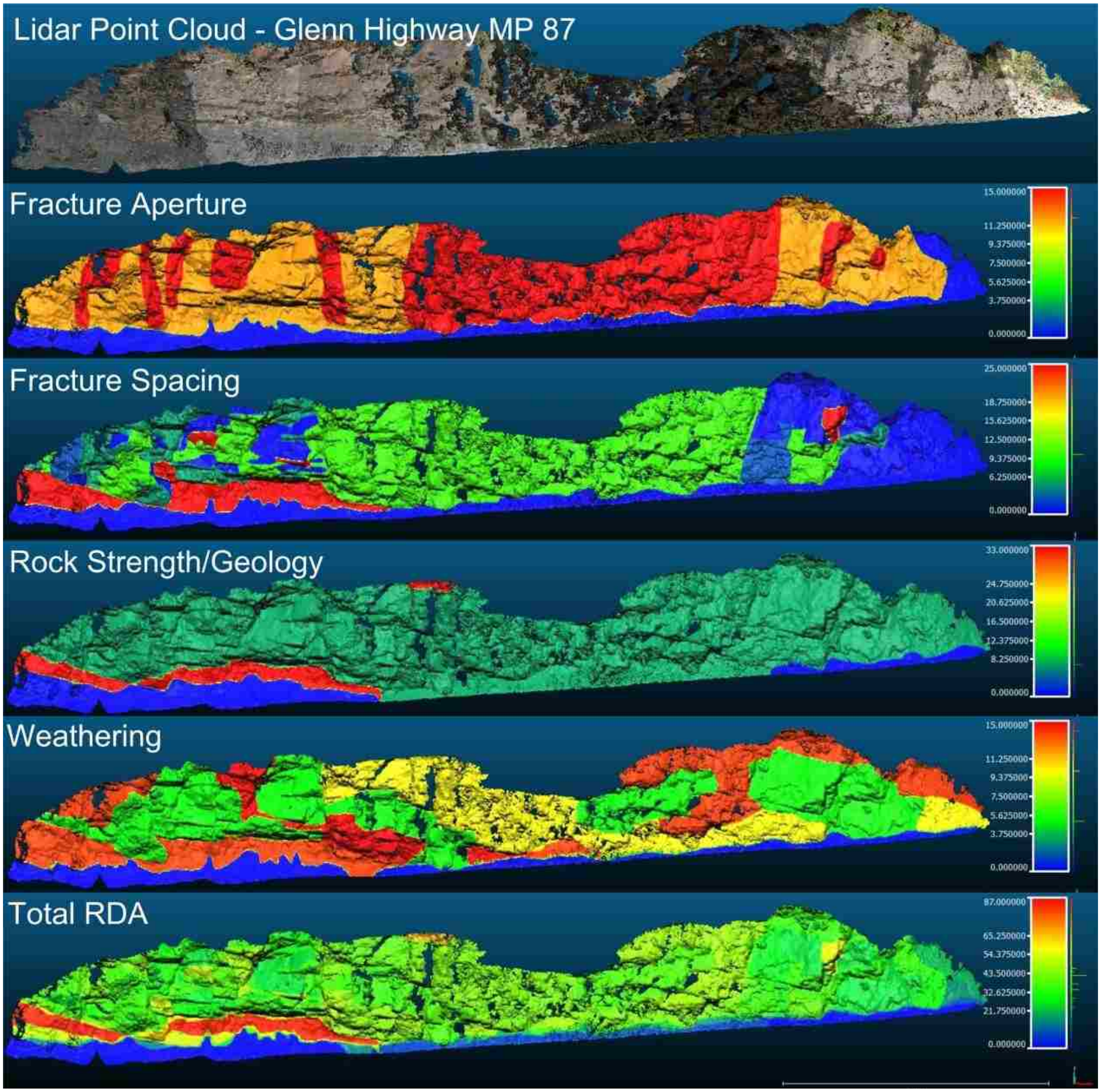

Figure 4.9: Glenn Highway MP 87 RDA scoring clouds for the four individual attributes and a total score. Each attribute cloud was determined manually using photographs, lidar and field notes. Appendix D contains a RDA point clouds for other sites.

The main problem with these applications is the process. This can be a very labor intensive process in the case of the RDA where manual mapping for each attribute had to be done before a final score could be established. For the RHRS the process was easier, but the confidence level of this process was not as high as one would hope for and could be accomplished with greater ease in the field.

Both of these systems work well in their respective spheres and can be used to accomplish remote classification, although there is a loss of confidence and difficulty in implementation.

4.6.1 Use of lidar with classification systems

There was some reliance on the point clouds produced by the lidar scans to establish mapped attributes for the RDA, but the use of the 3D point clouds did not take full advantage of the lidar data. Also, this system proved difficult to use lidar data. The RHRS relied very little on the lidar point cloud and could have been completed without access to this data. Over all the lidar helped to map the RDA, but because of the mapping process, the final result was of a coarse resolution in comparison of the lidar data available.

4.6.2 Contributing Attributes

Sometimes there are one or two factors that drive a system. These contributing attributes are important to understanding and assessing slope stability. Both RHRS and RDA use a partially categorical approach to look at factors that sometimes overlooks the importance of these contributing attributes. Structural condition is one such factor that while there are several choices, many slopes examined did not fit precisely into any one category. Instead attributes that might be main contributors were lumped into a category that might not show their significance.

One contributing factor, overhang, is not a major attribute in either the RHRS or RDA. This is one of the main factors in Parks Highway’s geologic development and is a driving factor for the safety of these areas. The potential for use of lidar is not even considered by these systems as they were not designed for the fine resolution that can be provided along with the extra information that can be established through point cloud analysis.

4.6.3 Conclusions on classification Systems

The RHRS and RDA are current state of practice in field classification. This chapter discussed using point cloud data to improve the resolution and mapping, however, although it provides some benefit, it is limited by the various limitations of the classification systems. These systems have given us a foundation to understand rock slope processes that will now be built upon in our upcoming research.

5. Lidar Overview

To date, three lidar surveys have been completed for the Parks and Glenn Highway sites (see Table 5.1). The first survey was acquired and processed by David Evans and Associates while the second and third were acquired and processed by the Oregon State University (OSU) geomatics team under the direction of Michael Olsen. Methods of the lidar processing have been more fully laid out in the phase I, (Metzger, Olsen, Wartman, Dunham, & Stuedlein, 2014), and phase II, (Cunningham, Olsen, Wartman, & Dunham, 2015), reports for this project through Pacific Northwest Transportation Consortium (PacTrans). This section is a simplified brief overview of the processes.

Table 5.1: Dates of lidar scans along Parks and Glenn Highway

Year	Dates	Acquired by
2012	September 4-14	David Evans and Associates
2013	August 1-14	Oregon State University
2013	August 1-7	Oregon State University

5.1 Workflow

For purposes of this report, the workflow has been separated into four main steps as seen in Figure 5.1, planning, data acquisition, processing and analysis. The first three were done by David Evans and Associates in 2012, and by the Oregon State Geomatics team in 2013-14. The analysis will be the subject of the coming chapters in this report.

5.2 Planning

The key to the success of lidar scanning is detailed planning. This includes considerations for safety, site walkthroughs, and possible climatic issues.

1. Safety of those involved with the scan and those using the corridors being scanned should be examined. Different considerations will be made when using mobile verses ground based surveys, but safety for each is important. Ground based crews need more attention to safety as there are greater

risks while conducting a ground based survey. Safety measures such as lane closures and signage need to be used if they are found necessary.

2. Site walkthroughs are important and allow the identification of problem areas for Global Positioning System (GPS), areas where ground based scanning may be difficult or unsafe and allow areas where lidar scans might have difficulty capturing data can be identified. This can also involve finding the best locations and times to acquire GPS/GNSS (Global Navigation Satellite System) sites so that the data can be tied together as well as into the global coordinate system.

3. Climate can affect the ability of the scanners. If there is precipitation this can interfere with the scan and cause false returns. Other conditions such as humidity, temperature and other atmospheric activities can affect the signal returns as well as the GPS/GNSS.

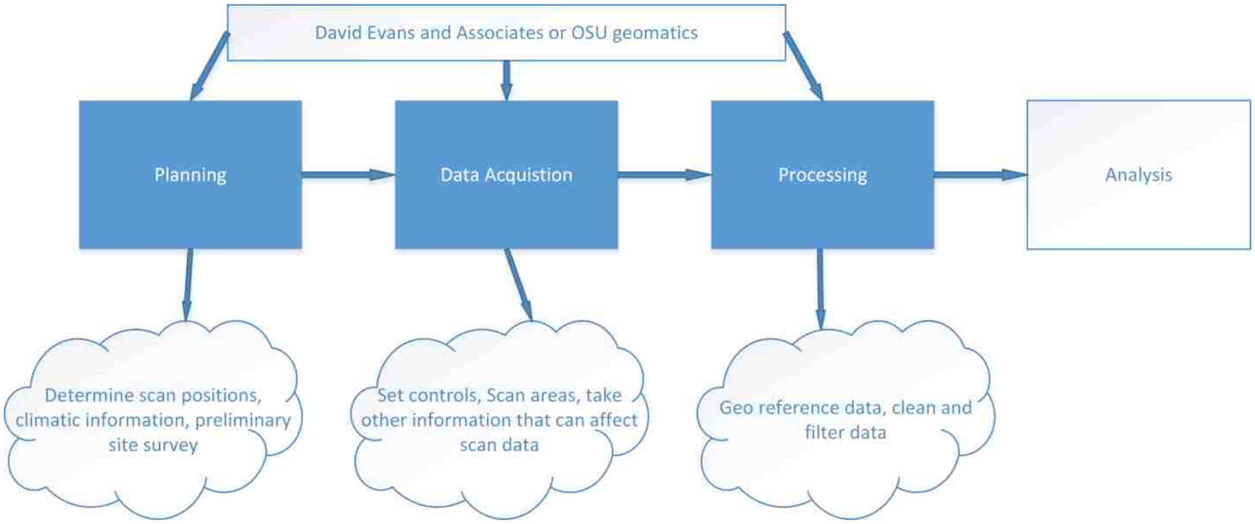

Figure 5.1: Work flow of lidar process. The first three steps were accomplished by David Evans and Associates (2012) and OSU in 2013-14. The analysis was the process that is described later in this report.

5.3 Data Acquisition

The first scan was mobile lidar conducted by David Evans and Associates using mobile lidar method with their terrestrial TITAN® Mobile laser scan system. There were also supplementary scans taken of locations that were difficult to survey from the highway using terrestrial laser scans. This survey was conducted from September 4-14, 2012 and provided a continuous data set for the study areas. During this scan, two primary GPS control points were set up at each of the locations. Mobile lidar data was acquired using multi passes that were later merged by David Evans and Associates. Figure 5.2 shows the product of these scans at Parks Highway and Figure 5.3 shows Glenn Highway. The color scale is according to the elevation of the points.

The second scan was taken from August 1-14, 2013 by graduate students from Oregon State University (OSU). A “stop and go” method was taken where a Riegl VZ-400 3D terrestrial laser scanner and GPS unit mounted to a wagon and scans of well-exposed cliff sections were taken, Figure 5.4 shows an example scan with real color mapped on to it. In this survey, areas were given priority as can be seen in Figure 5.5 and 5.6 showing Parks and Glenn Highway survey sites. The third survey was conducted August 1-7 by graduate students from OSU using a Riegl VZ-400 scanner by the same methods in the previous survey. During these surveys, lidar scans, digital images of sites, as well as GPS locations were taken at each scan position. Other field notes such as sketches, temperature, atmospheric pressure, relative humidity, approximate yaw angles, excessive wind, and falling rocks were also noted in a field notebook held at OSU geomatics lab.

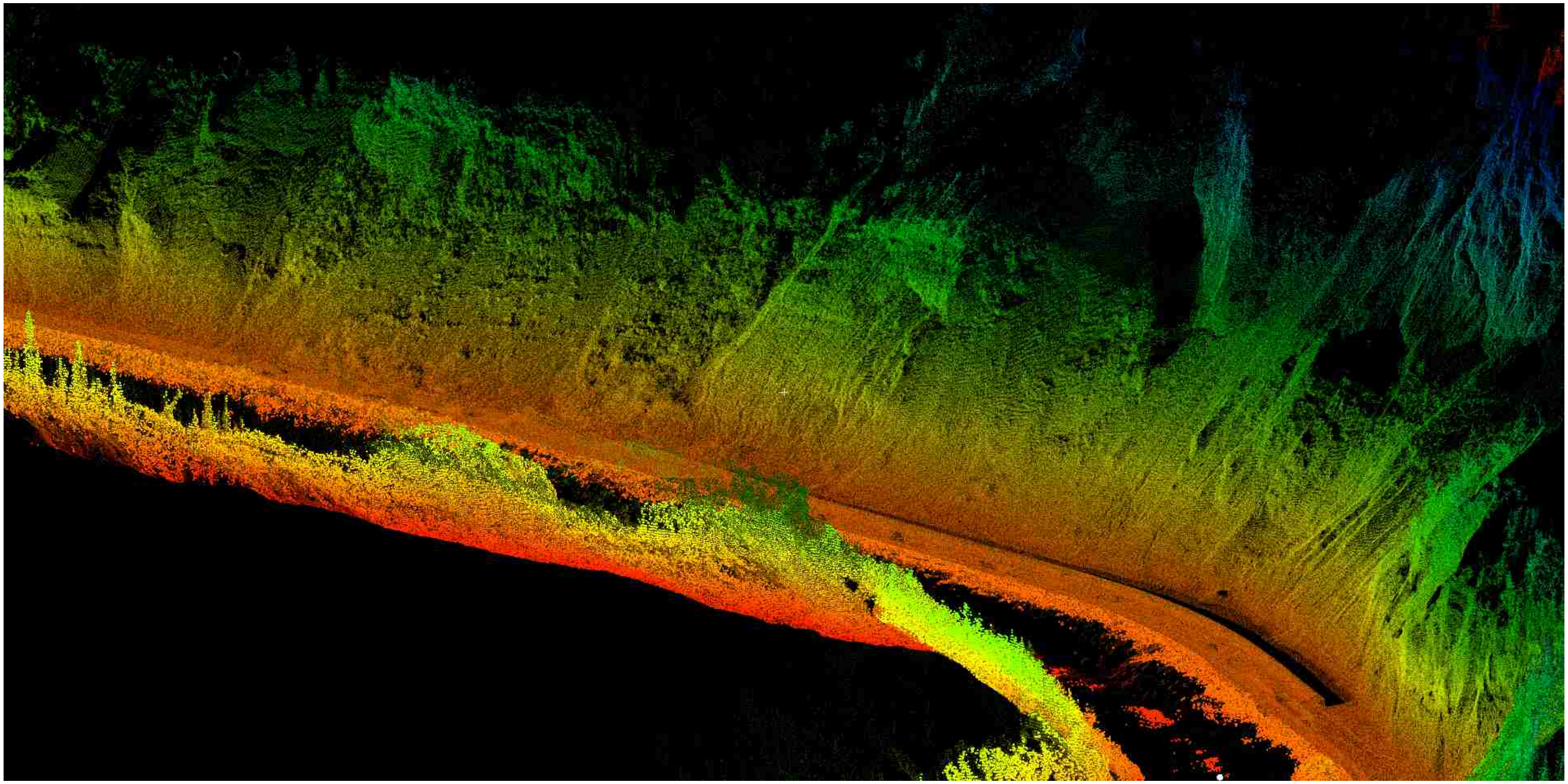

Figure 5.2: Example of lidar scan at Parks Highway from the 2012 mobile survey. The color scale represents the elevation of the points with red/orange being the lowest and blue/green being the highest.

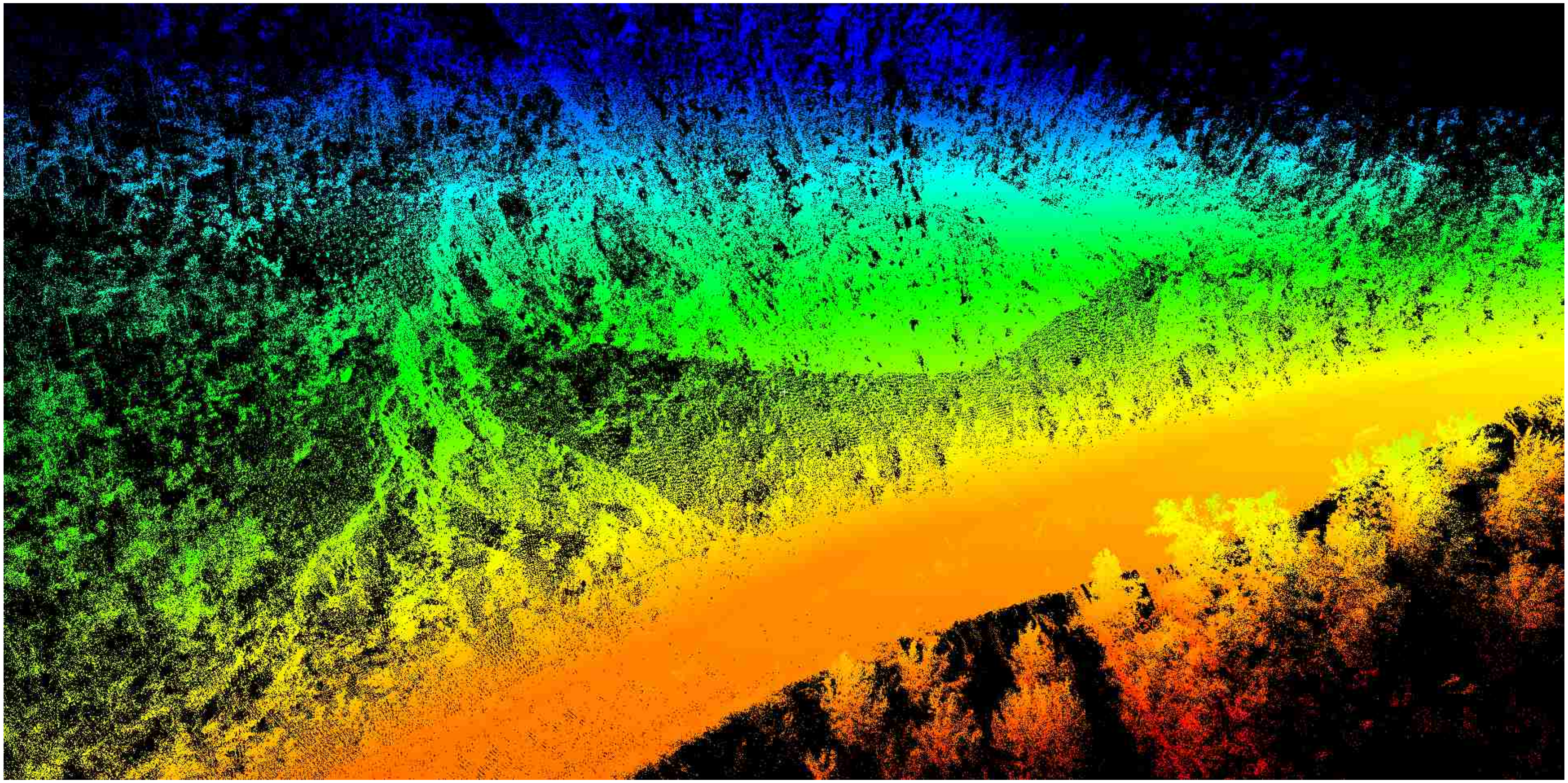

Figure 5.3: Example of lidar scan from Glenn Highway from the 2012 mobile survey. The color scale represents the elevation of the points with red/orange being the lowest and blue/green being the highest.

Figure 5.4: Example of 2013 lidar scan from an area along Parks Highway in an area that has highly unstable rocks.

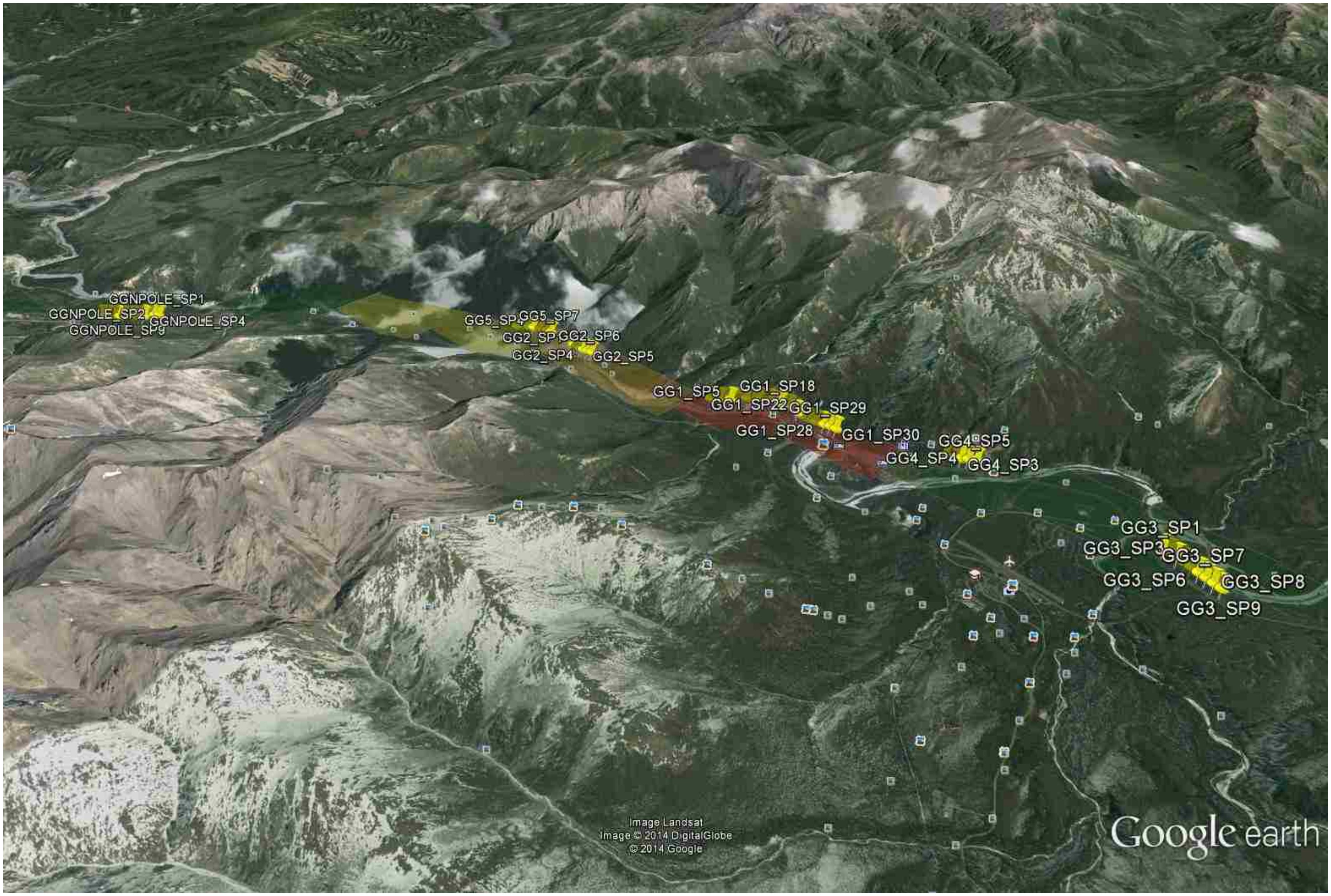

Figure 5.5: Parks Highway survey site. The different shaded colors were for the priority of the sites, the yellow pins were scan positions. The priority colors were: Red->Green = Highest -> Lowest Priority

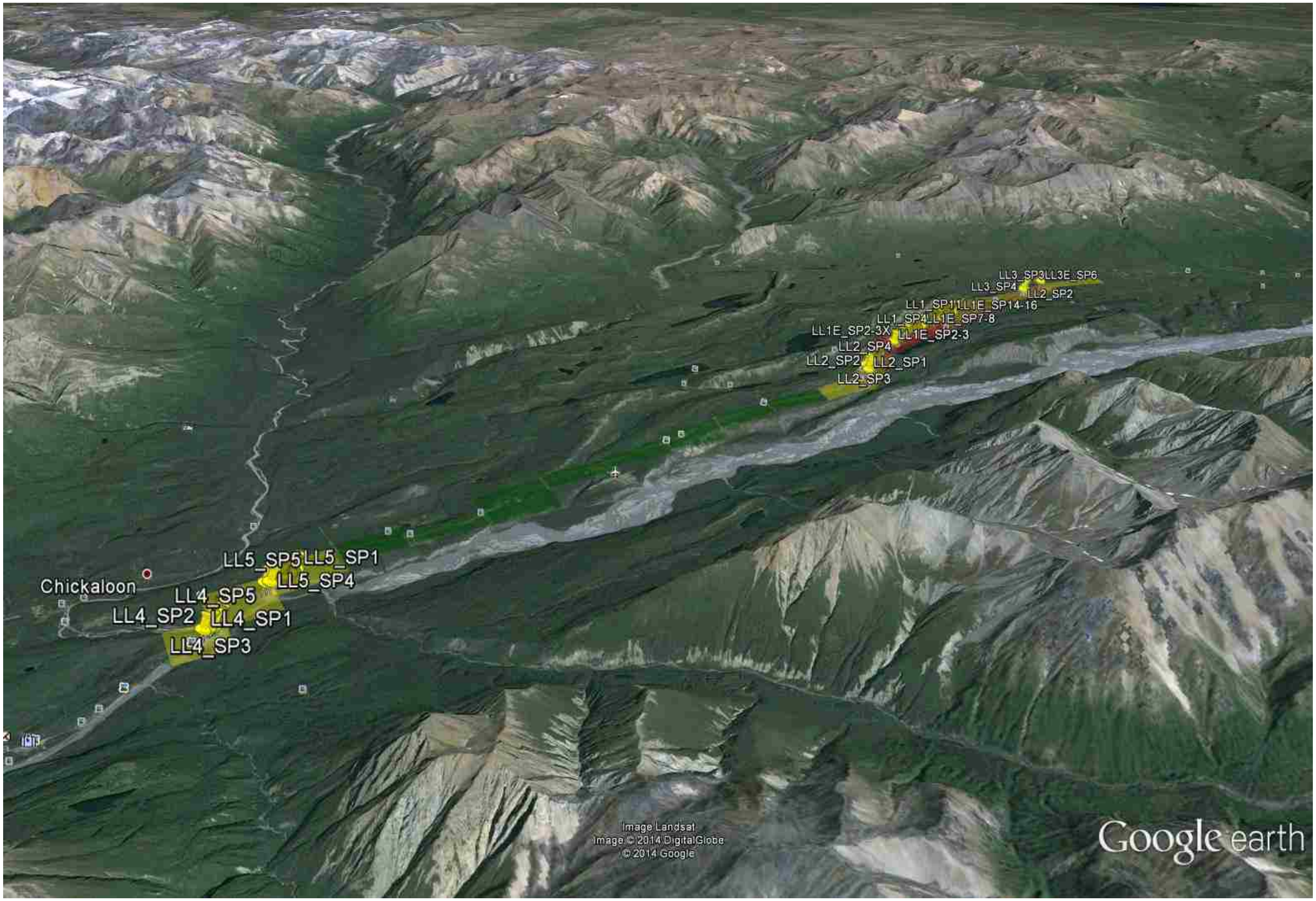

Figure 5.6: Glenn Highway survey site. The different shaded colors were for the priority of the sites, the yellow pins were scan positions. The priority colors were: Red->Green = Highest -> Lowest Priority

5.3 Data Processing

Each scan from mobile and terrestrial based lidar is in its own local scanner coordinate systems. These clouds must be combined into a single data set. Once the information is all in one data set, the clouds need to be georeferenced so they can be compared against other scans from the same area to see and evaluate temporal changes.

Once scans are referenced together, data needs to be filtered. Figure 5.7 shows examples of possible noise that needs to be removed from scans. Sources of noise include atmospheric conditions, vehicles, and vegetation. In ground based lidar scans, the removal of vegetation and noise can also cause loss of resolution, so this removal has to be conducted carefully. Ground based filter techniques have been created specifically for this project. (Cunningham, Olsen, Wartman, & Dunham, 2015)

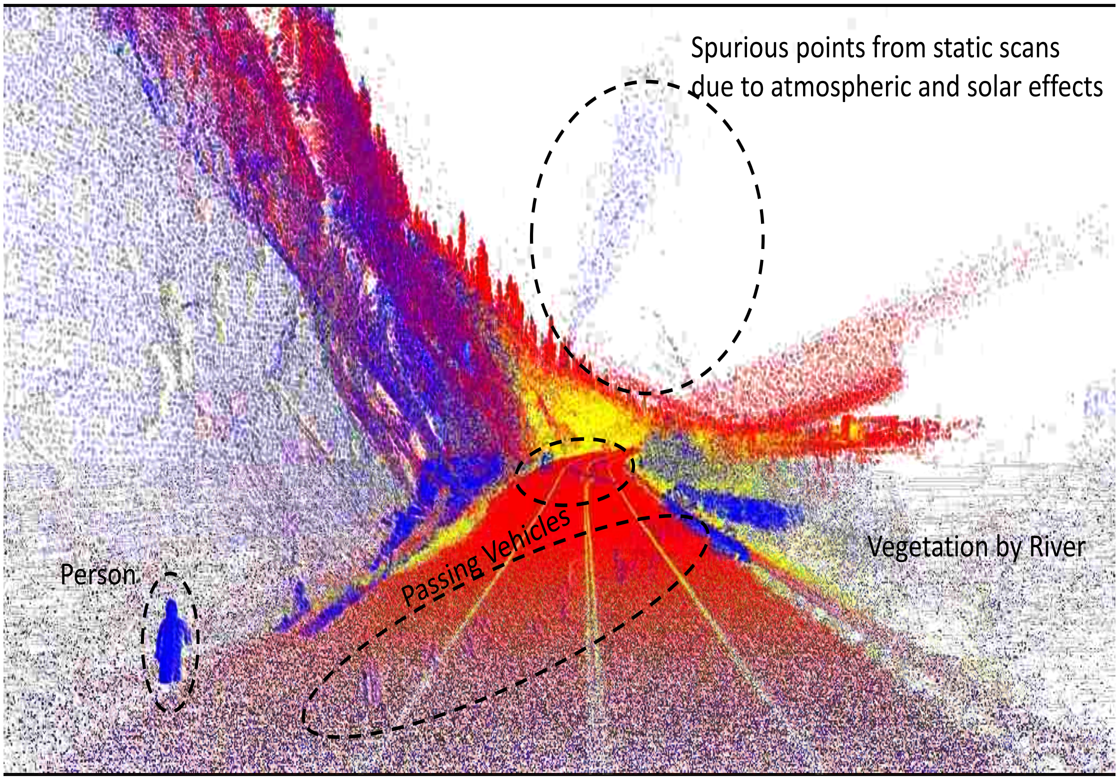

Figure 5.7: Examples of noise that is removed from lidar scans. If this noise is not removed, it can interfere with the analysis of the data.

5.4 Products of lidar processing

The finished result of the lidar processing is a 3D point cloud that can be further studied and analyzed. Point clouds can be visualized using one of several programs, including Maptek I-site, which offers a variety of analysis options used for this research. Another program, Cloud Compare, is an open-source code that functions on multiple operating system platforms, was also used. Processing was also accomplished with in-house software created for the RAI system (Cunningham, Olsen, Wartman, & Dunham, 2015).

Table 5.2 shows a selection of the output files that were produced and used in later analysis. The PARAMS.txt file is the cell by cell output of fields found in Table 5.3. Several of these cells, including SlopeDEG, RoughDEG35 and RoughDEG85, were used in the calculation of RAI classes in Chapter 6. Area and Rel_Z were used in the calculation of RAI energy rating. The FIDvolsNEG.csv file, which was based on change detection, was used in the frequency magnitude relationships that are discussed in Chapter 8. The CLASSAREA.txt and PARAMSSTATS.csv were both used in analysis at all stages.

Table 5.2: Selected output files produced by the RAI hazard rating program. Note that each file is created to append and change the extension of the name of the input file. For example, if the input file is GG10C.bpd, the ground filtered points would be GG10C_GRND.bpd. (Cunningham, Olsen, Wartman, & Dunham, 2015)

OUTPUT FILE	DESCRIPTION
bpd	Input file after running the binary converter for a text file that has X,Y,Z or X,Y,Z,R,G,B, or X,Y,Z,R,G,B,I values.
_PARAMS.txt	The master output file with the parameters described in Table 5.3.
_FIDvolsNEG.csv	An output file with the IDs, volumes, and dominate RAI class for each erosion cluster
_CLASSAREAS.txt	Area calculations (e.g., m^2 for each RAI class on the slope). 7 = unclassified, 8 = total area. This output file also provides failure rate for each RAI class (the number of cells that have failed for each RAI class, the total number of cells within each RAI class, and the percent failed).
_PARAMSSTATS.csv	Summary statistics of many of the parameters in the PARAMS.txt file.

Table 5.3: Output parameter fields of the RAI processing program (Cunningham, Olsen, Wartman, & Dunham, 2015)

Fields	Description
X,Y,Z	X,Y,Z coordinates of the centroid of the lidar points in each cell, typically in m
R,G,B	Average Red, Green, Blue color values (0-255) of all lidar points in each cell.
Intensity	Average intensity value of all lidar points in each cell
SlopeDEG	The local slope of each cell, in degrees
SlopeRAD	The local slope of each cell in radians
NX,NY,NZ	The normal vector components of the surface in each cell, based on its connectivity with neighbors
Rel_Z	The height of the cell above the base of cliff
RoughDEGXX	Roughness values for a window size of XX in degrees. Roughness values are determined as the standard deviation of slope within a window. For example, RoughDEG01 means that the roughness values is evaluated for a cell by looking at cells that are 1 cell away from the current cell. (e.g., a 3x3 window).
CRVX	For diagnostics only. Curvature in the X direction of the local, rotated coordinate system.
CRVY	For diagnostics only. Curvature in the Y direction of the local, rotated coordinate system.
CRVXY	Local curvature for each cell
Area	The 3D surface area connecting the centroid point of a cell with its neighboring cells.
CHG	The 1D magnitude of change in the direction of the best fit plane of the dataset (i.e. orthogonal to the general cliff surface). The units are the same as the input data, typically in meters. Positive values indicate accretion, negative values indicate erosion.
VOL	The change in volume of each cell between datasets. The units are the cube of the input data units (e.g. m^3). Positive values indicate accretion, negative values indicate erosion.
SIG_CHG	An indication if the observed change is larger (either positive or negative) than a threshold value to remove effects of georeferencing error. +1 means significant accretion was observed, -1 indicates significant erosion occurred, and 0 means that the difference was not significant (i.e., within +/- the threshold value).
FID_NEG	The ID for the cluster of erosion which the cell belongs to. 0 indicates that there was no significant erosion in the cell.
FID_POS	The ID for the cluster of accretion which the cell belongs to. 0 indicates that there was no significant accretion in the cell.
KE	The computed kinetic energy for the cell, in Joules
REI	The rockfall energy index (REI) for the cell
RAI	The RAI classification for the cell. UNCLASSIFIED = 0, TALUS=1, MASSIVE_STABLE=2, SMALL_ACTIVE=3, MEDIUM_ACTIVE=4, LARGE_ACTIVE=5, SHALLOW_OVERHANG=6, FLAT_OVERHANG=7.

RAIclusterPOS	The general RAI classification for the accretion cluster that the cell belongs to. -1 indicates that it is not applicable.
RAIclusterNEG	The general RAI classification for the erosion cluster that the cell belongs to. -1 indicates that it is not applicable.

6. RAI implementation

6.1 Rock-slope process mapping:

The basis of the rock-slope process mapping is understanding the different types of structure and erosion occurring in a rock-slope. Rock-slopes continually evolve due to erosional forces including water, climate and anthropogenic affects, and their stability is affected by the structural condition. Understanding how these processes and conditions manifest themselves geomorphologically is vital to understanding how rock-slopes deteriorate over time. Geomorphological indices, as seen in Figure 6.1, of roughness, slope and curvature are used to distinguish between types of processes and materials found on a rock-slope. Through identification of key classes which affect stability of slopes a hazard rating can be derived. For this analysis, seven classes are used but more or less can be used dependent on the site characteristics. Figures 6.2-6.4 show the different classes. Figure 6.2 shows talus and intact, size classes of 10 cm, 20 cm and 30 cm in Figure 6.3 and the difference in overhang <120 degrees and overhang > 120 degrees in Figure 6.4. Table 6.1 gives a short description of each of class. These classes generalize specific processes and features, identifying areas which would act the same way during failure of a slope not identifying each individual cell belonging to a specific class if such a classification was done by hand.

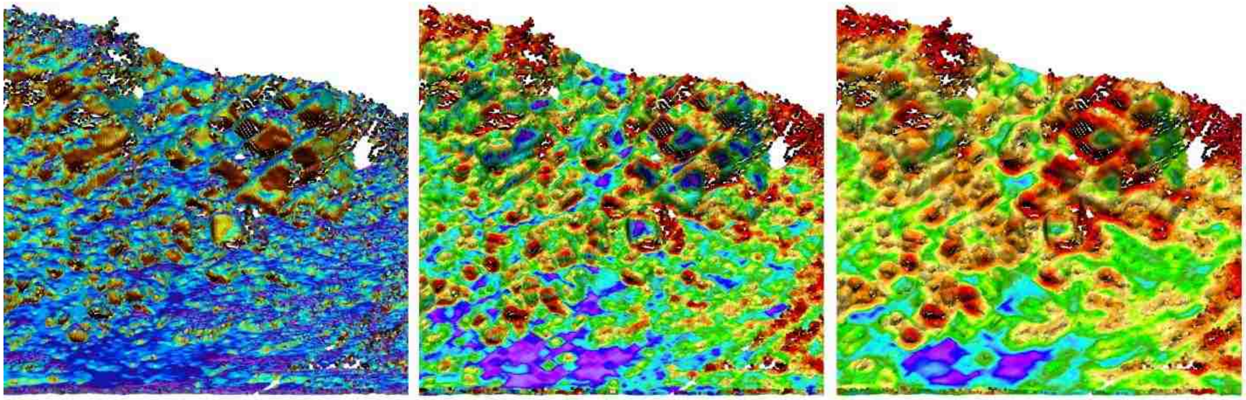

Slope Roughness 25x25 cm window Roughness 55x55 cm window

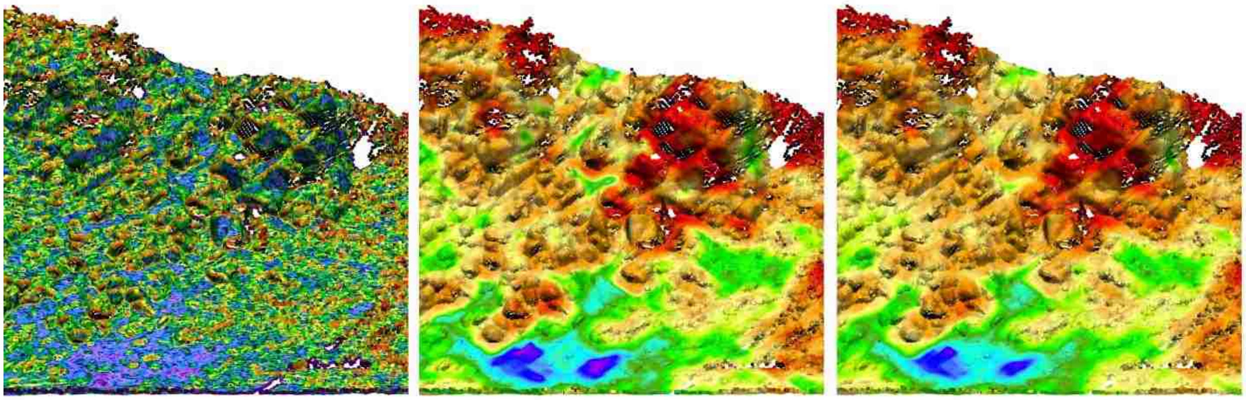

Curvature Roughness 85x85 cm window Roughness 105x105 cm window

Figure 6.1: Geomorphological indices calculated on 3D point clouds. Each index highlights slightly different aspects of the slope. By combining several indices different erosional processes can be highlighted.

6.2 Geomorphological Features:

Talus is rock debris mostly found at the bottom of slopes, although it can deposit anywhere in the slope. These are made up of loose material that has eroded from parent rocks and can be any size but the classification of talus focuses on small particles smaller than 3-5 cm. larger size particles are accounted for in the size classes discussed below of 10 cm, 20 cm and 30 cm. It is assumed that larger talus spread throughout the slope will continue to fail until it has reached equilibrium.

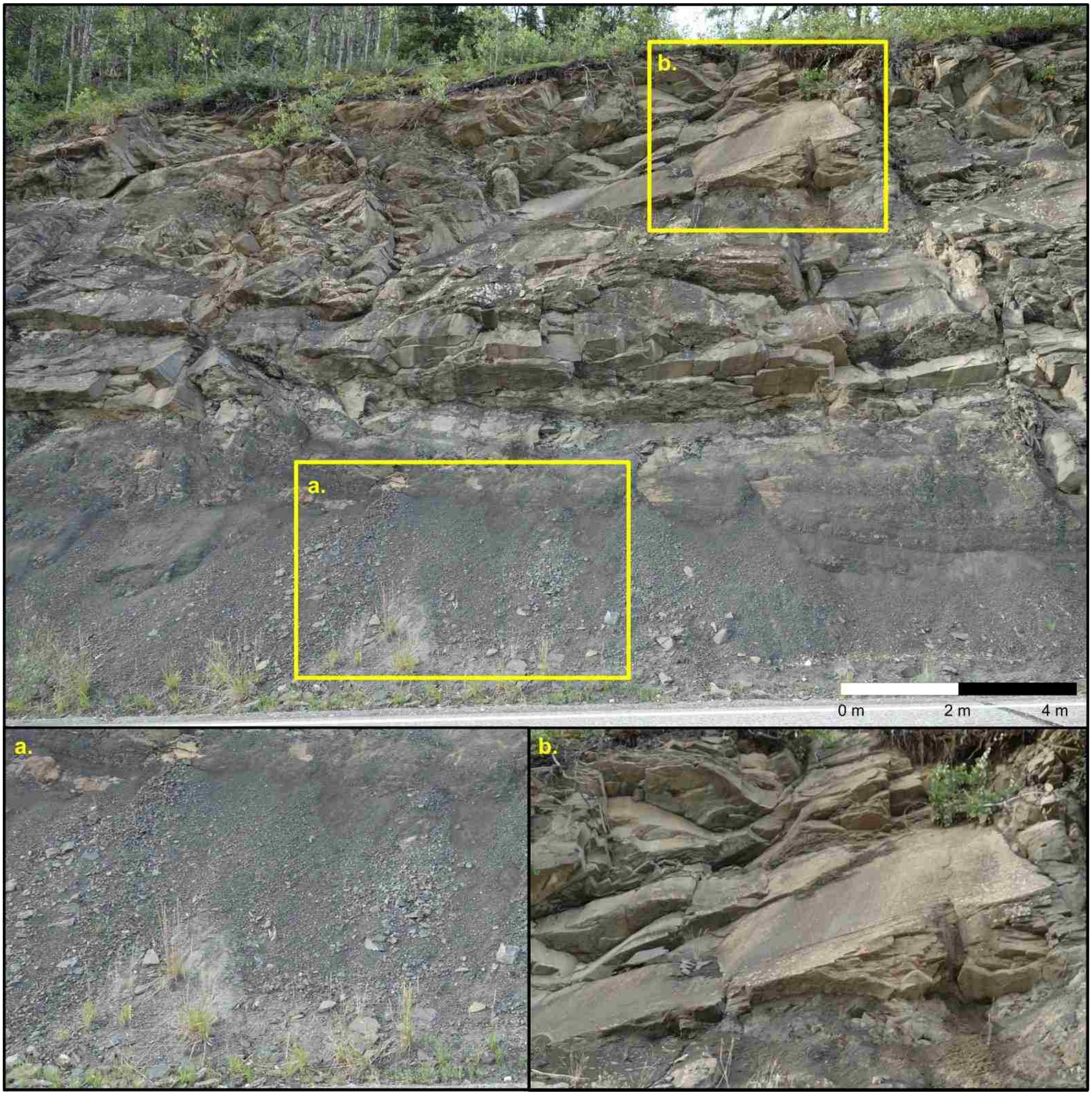

Figure 6.2: Example of intact and talus classifications for the RAI at milepost 87.

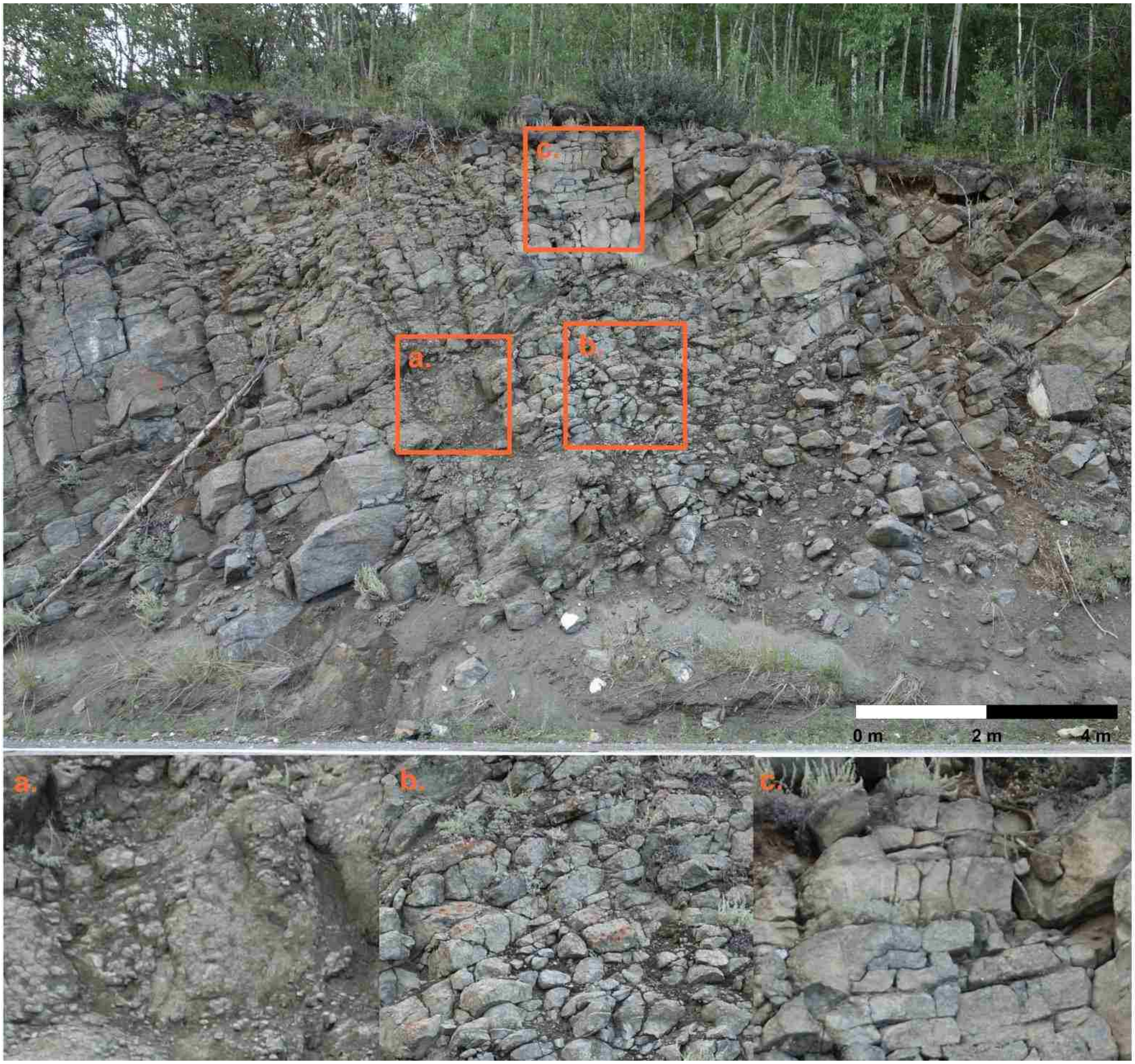

Figure 6.3: Examples of 10 cm, 20 cm and 30 cm active classifications for the RAI at milepost 85

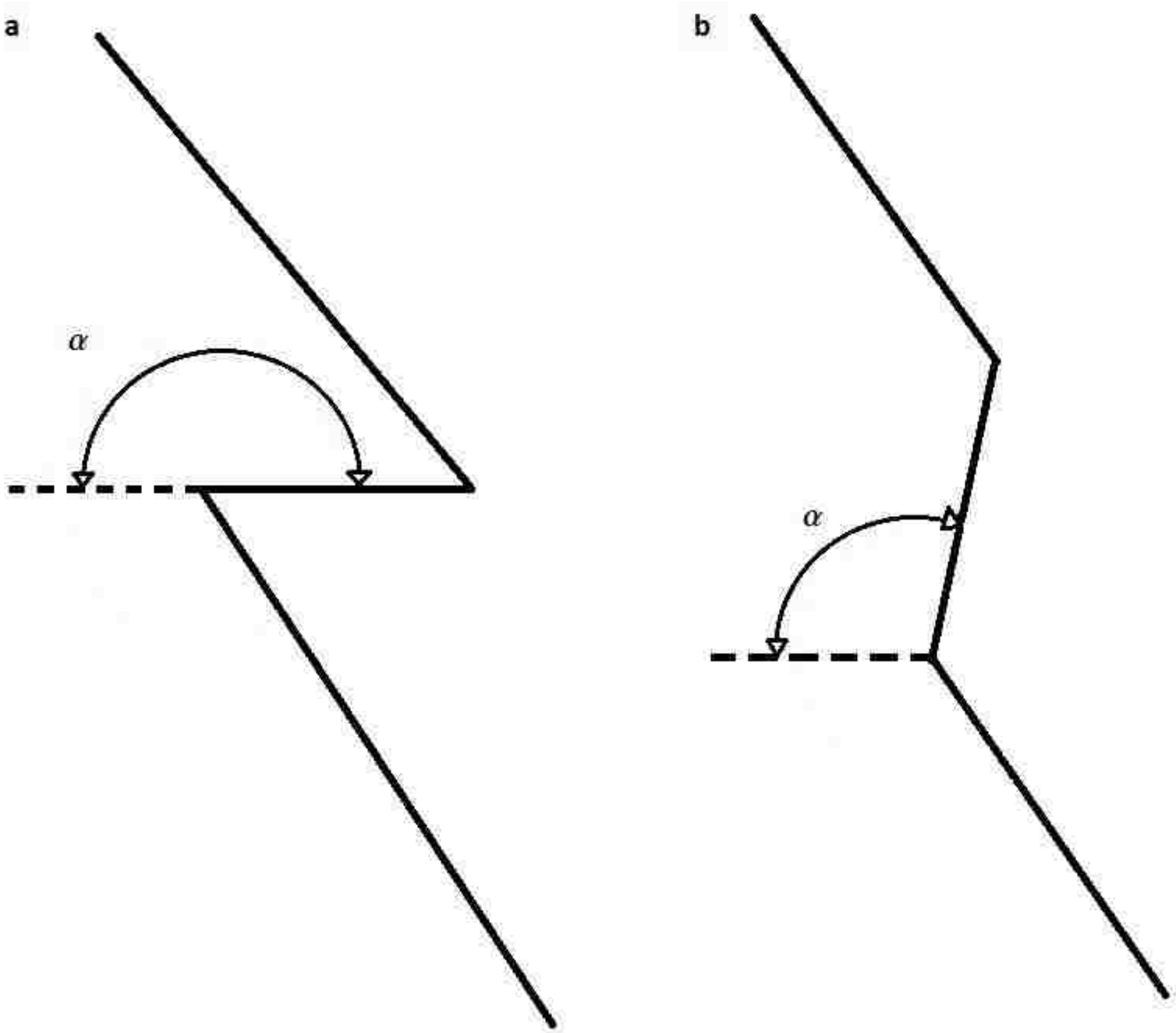

Figure 6.4: the measured angles α for a) flat overhang or overhang greater than 120 degrees and b) shallow overhang or overhang less than 120 degrees for the RAI

Table 6.1: Summary of classes used in the Rock-slope Activity Index.

Name	Description
Talus	Small debris mostly found in the bottom of the slope, although can be found throughout the slope
Intact	Little to no fracturing of rock, would act as one large rock if released
10 cm	Rock that is either in place or has moved that is smaller than 10 cm
20 cm	Rock that is either in place or has moved that is between 10 cm and 20 cm
30 cm	Rock that is either in place or has moved that is larger than 30 cm
Overhang <120°	Overhangs from near vertical to 120°
Overhang >120°	Overhangs greater than 120°

Intact are areas of whole rocks with little to no discontinuities. These may occur anywhere in the slope and can be surrounded by areas of differential erosion, such as overhangs. These areas, although they may contribute to instability, they do not generally fail on their own. Failure of these areas normally is accompanied with the failure of instable areas such as overhangs.

Figure 6.3 shows the intact size classes of 10 cm, 20 cm and 30 cm which are areas considered to have erosion actively occurring. This is normally through breakup of the parent rock, but as stated in the talus description, there can be movement of rock from original place. These classes are distinguished according to size, with the assumption that as debris gets larger, the impending risk will increase. The size differences depend on the average length of the protruding sides where the average is the name of the class.

Overhang is classified into two categories dependent on slope with the assumption that the steeper the overhang, the more material will be above it as well as stability will be decreased. These classes are separated at 120 degrees as can be seen in Figure 6.4.

6.3 Characterizing with geomorphological indices:

Localized slope and roughness are used as morphologic indices for the classification of rock-slopes for the RAI. Slope provides a good indicator of morphology by itself, distinguishing between stable areas composed of rock versus unstable areas. For example, talus or soil deposits can be evaluated by the angle of repose, which tends to be shallow. Overhangs can be highlighted by steep slopes ($>90^o$). Roughness has been shown to be a characterizer for different geomorphological features such as alluvial fans (Frankel & Dolan, 2007). Together they are able to identify the differences between landslide failure modes [(Dunham, GNS-Report 2015) and (Berti, Corsini, & Daehne 2013)] examined different algorithms for surface roughness and discussed the best and easiest to use. They concluded that roughness as a standard deviation of slope was found to be a good indicator of roughness as well as relatively easy to compute.

Using these indices, slopes were explored manually, as seen in figure 6.5, to see where thresholds which indicated different geomorphological classes were located. This was done through a process of manual classification because of the intermingling of classes which existed on the slopes. Statistical analysis was attempted, but it was found that areas of different classes overlapped and were hard to define in separate point clouds. Manual classification looked at all geomorphological indices calculated and found the best combination to distinguish between classes. In the end, three indices were used, Slope, Rough35 and Rough85. Table 6.2 provides an explanation of these indices.

Two roughness indices were used because different roughness windows highlight different features within a terrain. The roughness window to use depends upon the size of the object which you are trying to distinguish, therefore if small objects are to be considered, a smaller window would suffice but if large objects, such as boulders were the target, a window larger than the boulders in question would need to be used. Using a window too small or too large will create unwanted noise or smoothing. When using more than one roughness window to classify, they should be sufficiently different sizes that they are showing different features. In this case, 50 cm of difference was used.

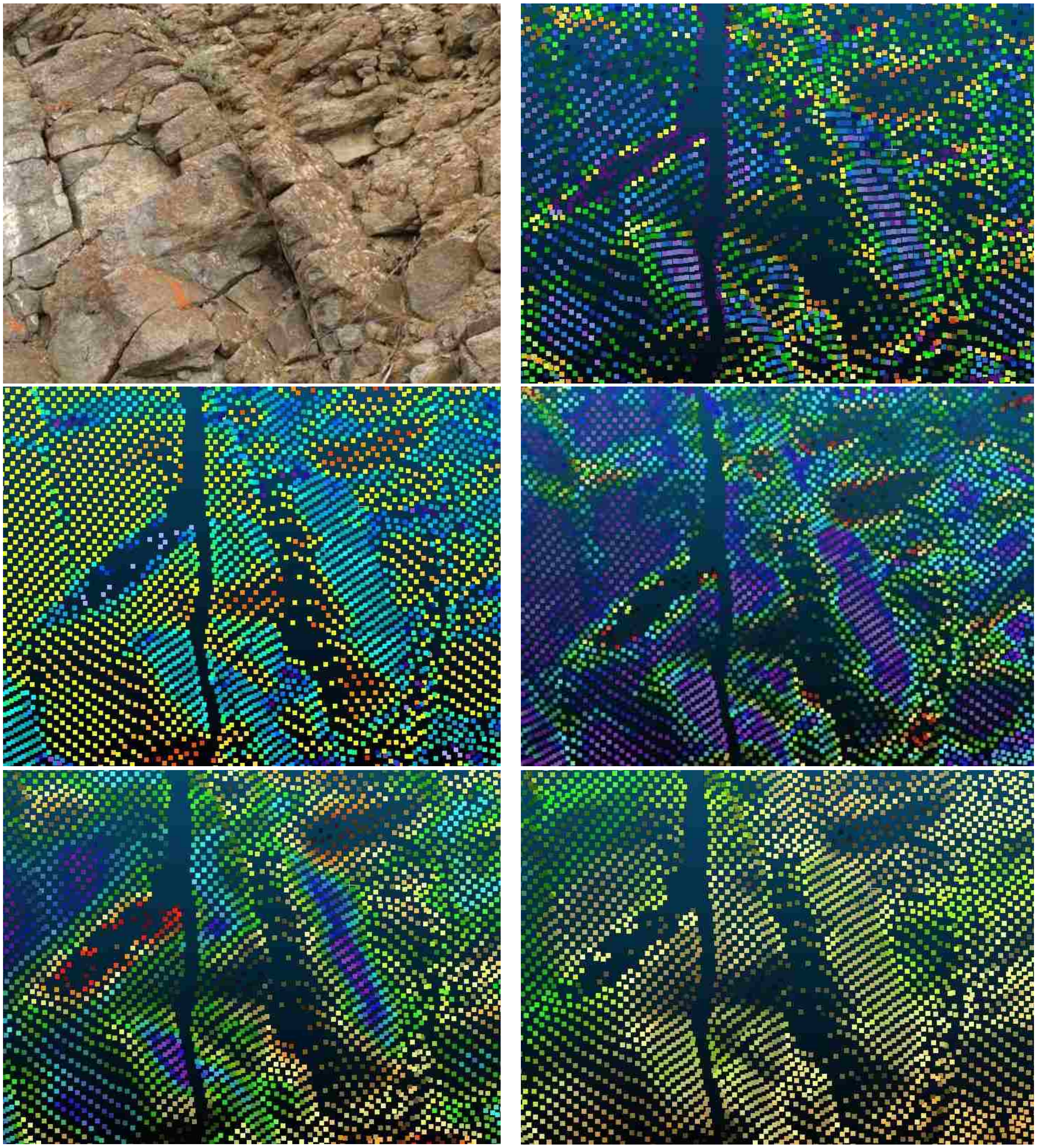

Top: Photo, Curve, Middle: Slope, Rough1, Bottom: Rough3, Rough10

Figure 6.5: Example comparison of five indices to photo of 30 cm classification

6.4 Classification:

Once the indices were established, as seen in figure 6.6, thresholds for each class were determined and an algorithm to classify was established. Figure 6.7 shows a flow chart of this process starting with the 3D point cloud, the first step is to determine slope categories between less than 90 degrees and greater than 90 degrees which classify normal slope material versus overhang. Above 90 degrees was then split into the two categories of <120 degrees and >120 degrees.

Slope material under 90 degrees was split into five categories, talus, intact, and the size categories of 10 cm, 20 cm and 30 cm. Because the size categories, talus and intact are close together in size, Roughness35 was used to distinguish between them with four categories. The two roughest categories were for 20 cm and 30 cm. To distinguish between the last three categories, roughness85 was used as an overall smoother split into two with the rougher of the two being 10 cm and the smoother being talus if it was below 35 degrees in slope and intact if it was above. It was found that the indices had a difficult time distinguishing between talus and intact so the slope was used as the deciding factor assuming that 35 degrees is the angle of repose.

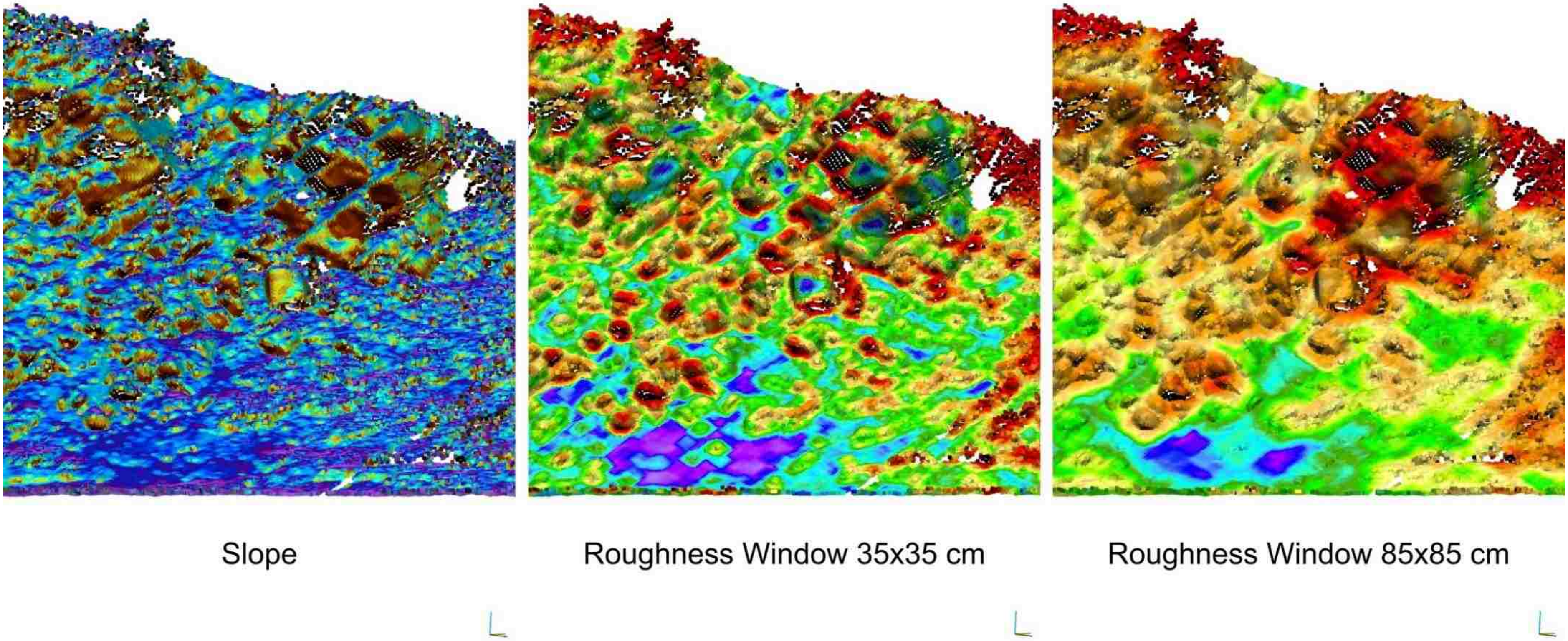

Slope

Roughness Window 35x35 cm

Roughness Window 85x85 cm

Figure 6.6: The three chosen indices for classification of the RAI.

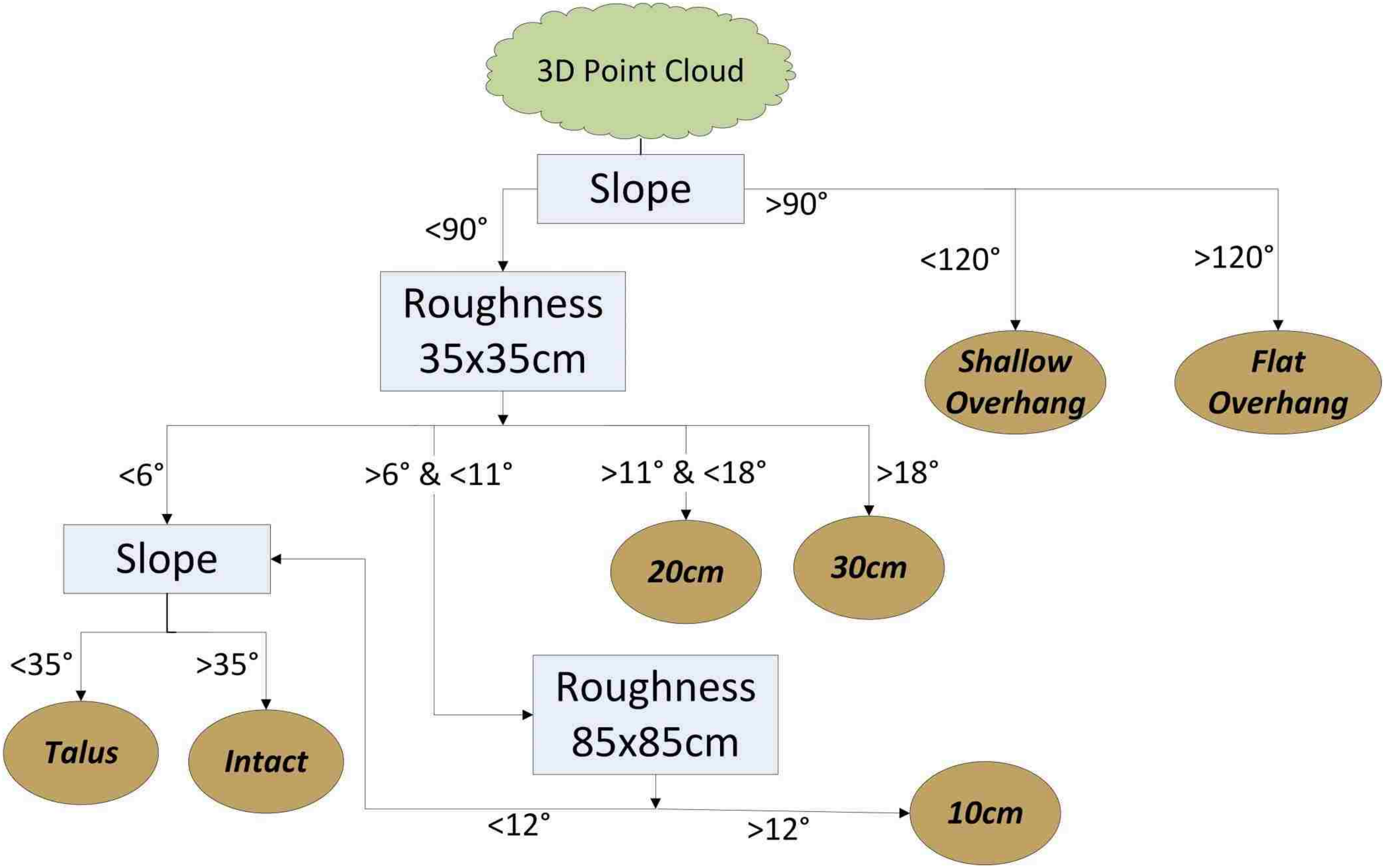

Figure 6.7: Each pixel has values for the roughnesses and slope which are used to determine which use this flow chart to determine classification.

6.5 RAI Rating:

Lidar can capture information about individual cells, enabling the design of a classification system to use each individual cell's properties. Using the classification systems as a guide, each cell was given three ratings related to: size, height and failure rate. The overall concept is based on the principle of Kinetic Energy assuming the following equations:

$$KE = \frac{1}{2} * m * v^2$$

Where KE is Kinetic Energy, m is mass and v is velocity. Size and height are used to find mass and velocity of each cell. Once the Kinetic Energy released for each cell is known, it can be multiplied by the class failure rate to obtain the cell's potential energy release for a specific time. Using the classes and individual cell properties, mass and velocity are calculated as follows:

6.5.1 Mass:

Volume is used as a proxy for mass because an estimation of the volume can be determined quickly via the lidar data. It is assumed that the specific gravity is the same across a slope.

$$m = V * SG$$

where V is volume and SG is specific gravity. The area calculated in the lidar processing above was used to determine the volume with the assumption of the depths in Table 6.2. These depths use average lengths of each class for talus, intact and the size classes. For the overhangs, 10 overhangs were measured, and an average rounded size was used as a depth with the assumption that the overhangs less than 120 degrees will have less material above them than the overhangs over 120 degrees.

Table 6.2: Assumed depth and typical failure rates in each RAI category based on change that occurred over a 1-year period

	Assumed Depth (m)	Failure Rate (%)
Undefined	0.025	0.40
Talus	0.025	0.00
Intact	0.05	0.10
10 cm	0.1	0.18
20 cm	0.2	0.34
30 cm	0.3	0.71
<120	0.5	1.98
>120	0.75	1.97

6.5.2 Velocity:

Each cell has a centroid with elevation, so a relative height can be determined as the elevation of the cell minus the base elevation. From this relative height (h), velocity can be calculated using the following relationship:

$$v = \sqrt{2gh}$$

6.6 Failure Rate:

The failure rate for the rock slope was determined by a manual method because the computer generated failure rate was found to have too much noise. In the future, once this problem is resolved, the computer failure rate will be preferred. Appendix E shows the difference between the two failure rates.

The manual failure rate was determined using photos from two years, 2013 and 2014, which were examined for change. When a change was spotted, screen captures were taken of the 2013 and 2014 photos, the RAI classification for 2013 and the change detection located on the point cloud. The area of change was then identified on the RAI classification cloud using the change detection and photos as reference and the points within the failure were counted according to class. In all this method identified 18 failure areas, although more may be present but not identified due to angle of the photos or size. To find the exact location on the 3D point cloud can be difficult. General areas are normally easy to identify, but specific spots can pose a challenge. Because of this, many of the areas are approximately in the correct place and the cells counted may be greater than the actual cells with failure. It is assumed that this excess would account for the failures not identified.

6.6.1 Cell RAI Score:

With the understanding that:

$$KE = \frac{1}{2}VSG\left(\sqrt{2gh}\right)^2$$

The RAI hazard score for each cell can be calculated:

$$RAI = KEP$$

Where P is the failure rate from table 6.2 above.

Each cell within a grid can be classified and a hazard score can be calculated. This allows users to pinpoint areas that might be potential problems and understand slope processes that are causing these issues.

6.7 Implementation of RAI:

Figure 6.8 shows a small section of MP87 along the Glenn Highway in Alaska with 6.8a a photo, 6.8b the RAI classification and 6.8c the RAI hazard rating. The areas that we wish to distinguish are overhang, areas of smaller debris sources and areas that are relatively stable. In the photo it is fairly easy to distinguish intact and talus areas that are relatively stable and areas smaller debris sources, but overhangs can be difficult to precisely locate without a good reference to the direction of the ground.

In the classification system, overhangs are easily distinguishable in the yellow and red colors. The size classes highlighted in blue with 10 cm being the lightest pick up the smaller debris sources, although they do not necessarily pick out correct sizes. The 30 cm size catches the edges of rocks, which are normally any size while the 20 and 10 cm detect areas that have smaller debris in them. Talus and intact are distinguished with the green and purple colors and are somewhat interchangeable because the only difference is the slope in their definitions. Although they may not exactly identify the talus and intact areas, it is giving a sense of the potential differential stability between areas of low slope, less than 35 degrees and higher slope.

The hazard map is a reflection of the classification system as it highlights the same areas as the classification map, overhang followed by areas of small debris source receive the KE rating. Also the hazard map shows increasing hazard scores at different levels as cells move up the slope because of the height effect on the velocity, a component of the KE equation. Highlighted in darker colors (oranges going to reds) are the overhangs and large active areas. Areas such as medium and small active progressively get darker orange/yellow colors up the slope. Areas that stay light yellow represent areas of talus and massive stable having little impact on kinetic energy release.

6.8 Performance of the RAI:

Examples of RAI can be seen in Figures 6.9 and 6.10 show two sites, MP 87 and MP 85.5 respectively with lidar point cloud data (a), classification system (b) and hazard rating (c). (See Appendix F for other sites) The RAI classification system generalizes the talus and intact as well as the size classes. These generalizations though are more representations of what is going on in individual areas for example although a large rock area is not classified as 100 percent active large, the edge, which is classified, shows the area that is most likely to be eroding. Areas in the center of the rock might have small erosion going on, but larger failures tend to happen towards the edges of the block as a whole, thus highlighting the area that will most likely fail and allowing users to investigate further.

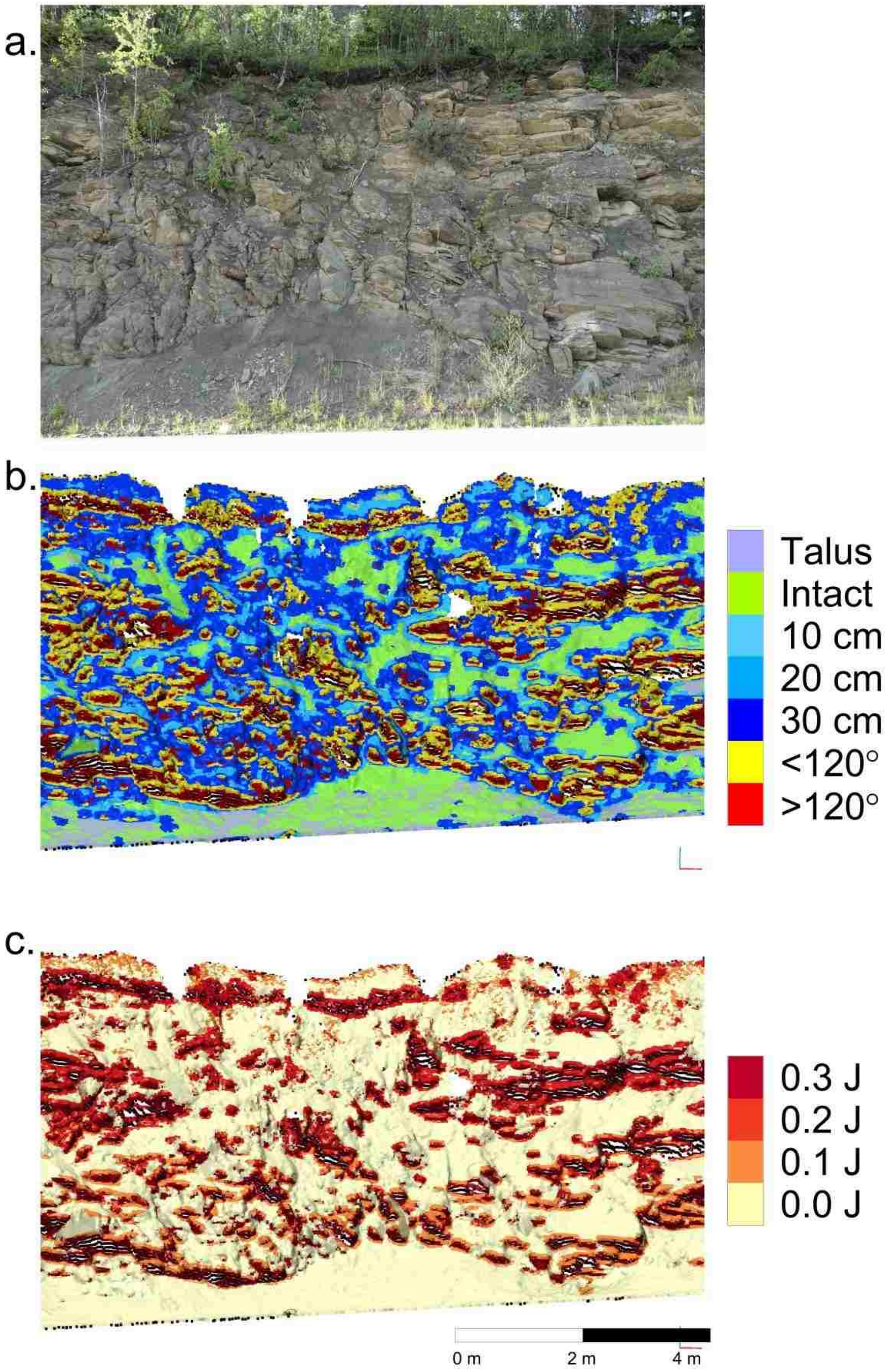

Figure 6.8: Example area of RAI system. a. photo of area, b. RAI classification, and c. RAI hazard rating

Because the data was calibrated to one year's worth of MP 87 this model might have some inherent flaws when the failure rate is considered. Although it should be a representative year for the failure rate, MP 87 contains different types of rocks than the MP 85.5 and other sites. Also this model does not include larger failures that will occur over the lifetime of the slope. The weather as well as type of rock will affect the rate of failure in rocks so location specific information can be added to this model to customize it for individual locations and slopes as well as overall data from multiple sites so an average can be obtained will create a more robust model.

6.9 Application of the RAI:

The RAI allows users understanding of slope processes so focus can be on the most hazardous areas. Through applying to individual sites, users can understand which areas are contributing the most to overall hazard of a slope. Figure 6.11 demonstrates 4 resolutions of RAI scores from cell size to site. This allows users to examine overall trends within a slope and quickly locate areas that might need more examination.

Another application which will be discussed in Chapter 8 is understanding frequency and magnitude relationships which allow for forward prediction. This allows asset managers to plan maintenance and operations as well as focus on slopes which are likely to fail more often.

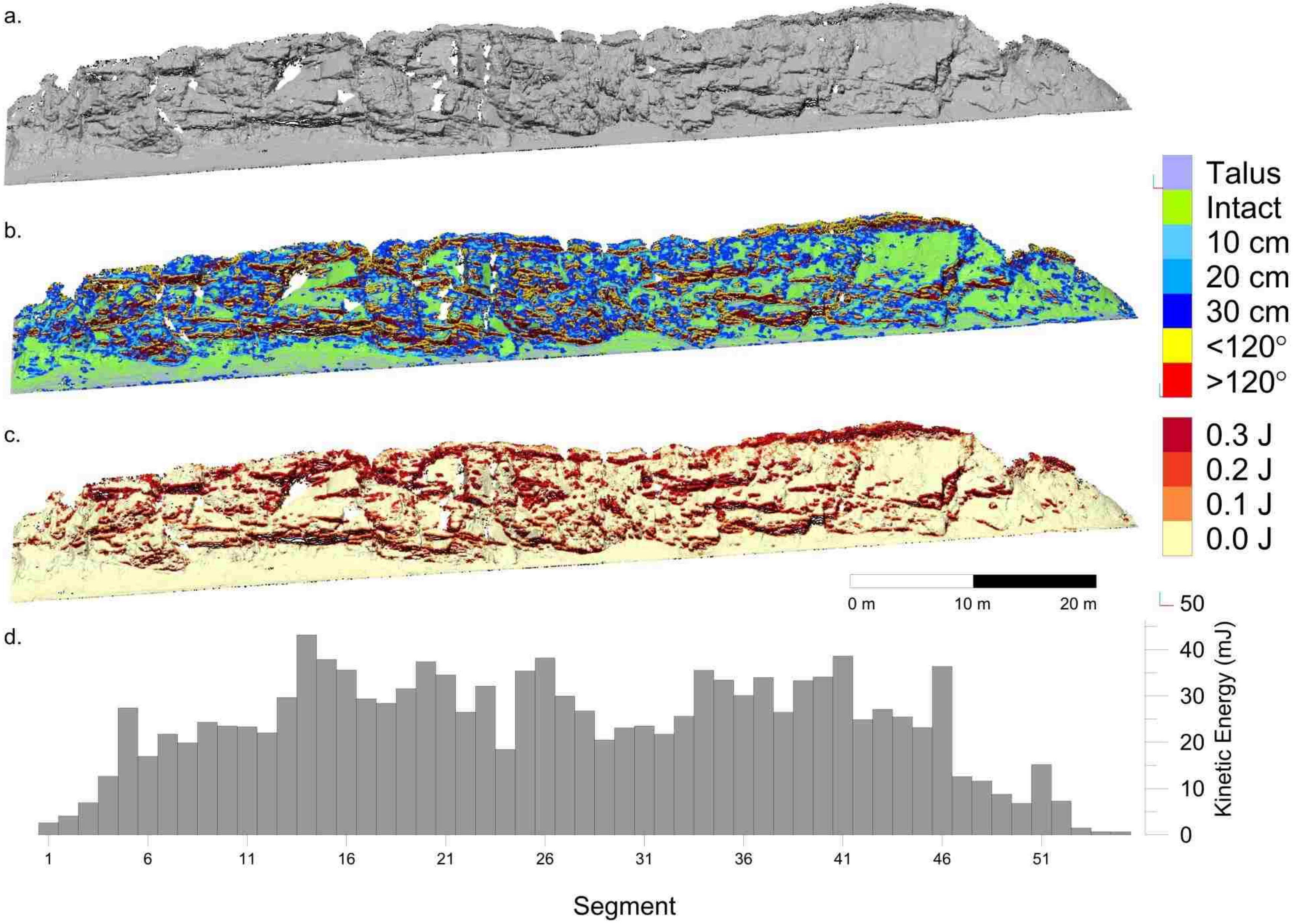

Figure 6.9: MP 87 a. lidar scan, b. RAI classification, and c. RAI-KE rating d. 2 m RAI-KE totals

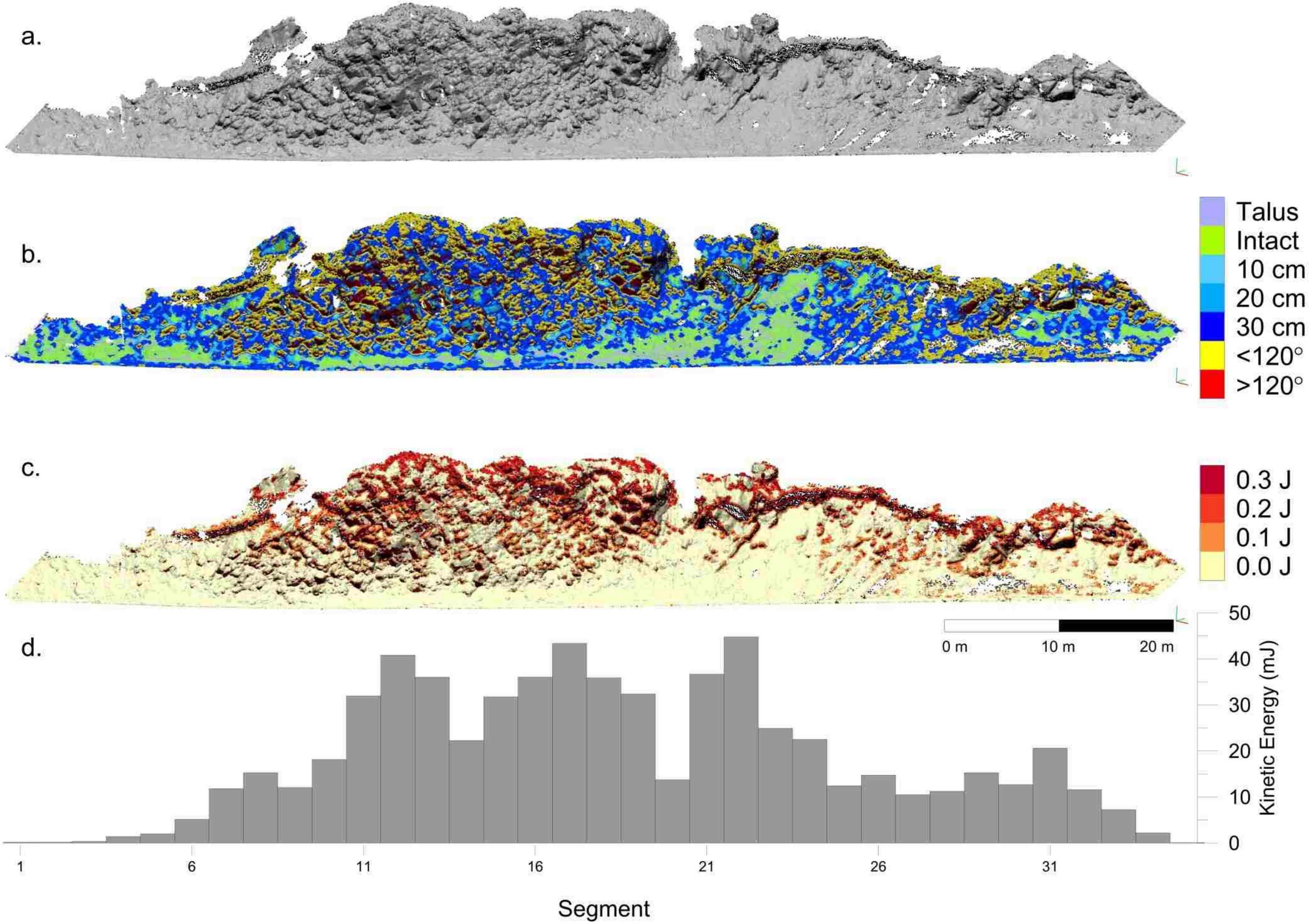

Figure 6.10: MP 85.5 a. lidar scan, b. RAI classification, and c. RAI-KE rating d. 2m RAI-KE totals

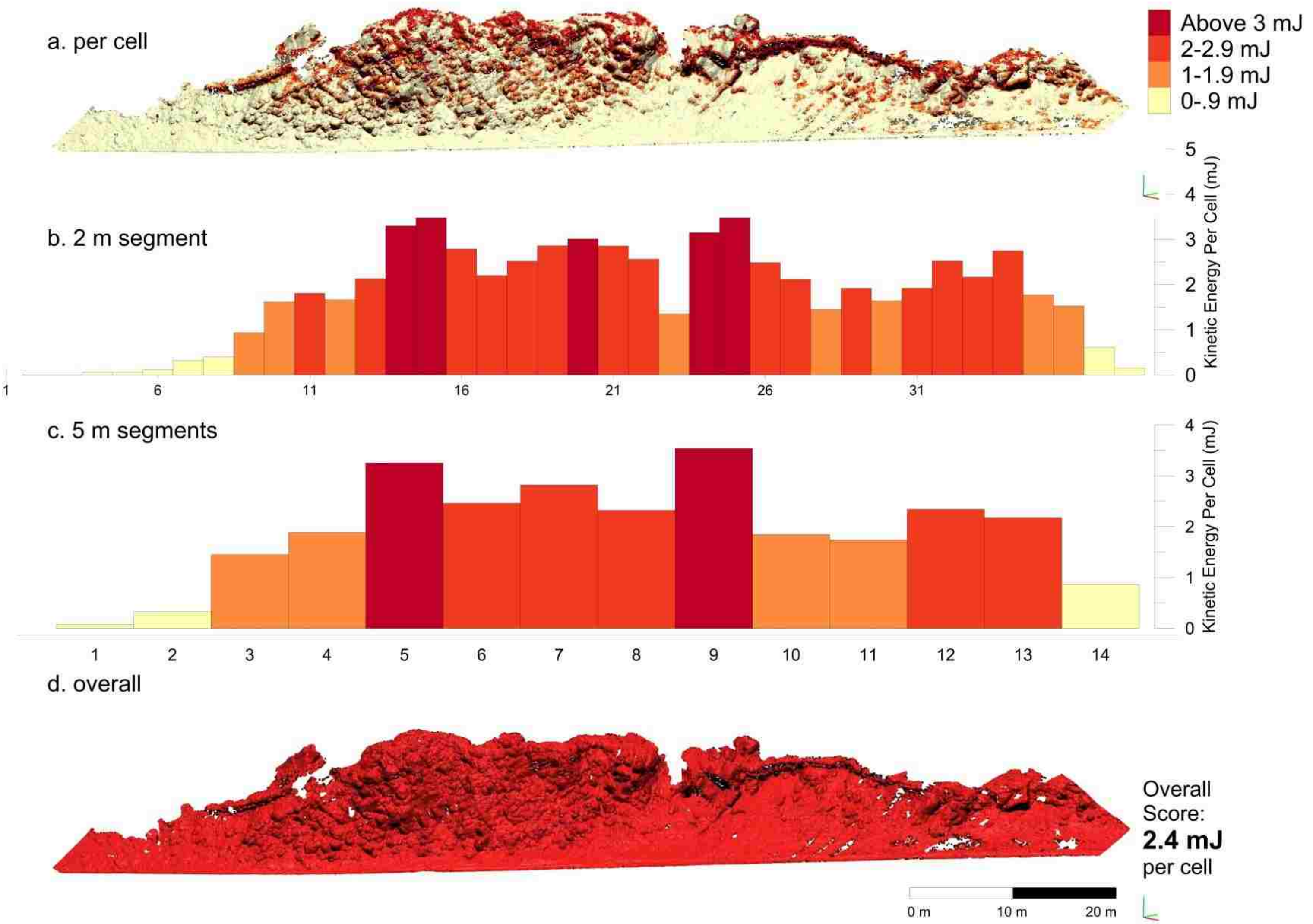

Figure 6.11: Glenn Highway milepost 85.5 shown in four resolutions of RAI a. overall per cell score, b. 2m segments, c. 5 m segments and d. overall site score per cell

7. Comparison between current systems and RAI and change

The main objective of this project is to find or create a classification system that can be easily used with advancing 3D point data. Many transportation agencies are beginning to use lidar imagery as a way to inventory and assess the state of infrastructure, but to the author's knowledge, a system that allows quick understanding of rock slopes using these clouds is not available. In this study, two existing classification systems are examined and then a third created by the author (RAI) is compared to these for abilities to enhance the lidar cloud imagery and assess rock slopes remotely. For this study, all work was done remotely through photography, lidar imagery and notes from those who visited the site.

The two systems used, the Rockslope Deterioration Assessment (RDA) and Rock-fall Hazard Rating System (RHRS), were chosen for different reasons. RHRS is used by many Department of Transportations around the United States (Huang, Darrow, & Calvin, 2009) and therefore familiar to many potential users of a new lidar based system. The RDA focuses more on deterioration and complements the RHRS which has limited deterioration consideration.

This chapter examines the usages, attributes, and application of these two systems for a greater understanding of classification systems in order to design a remote classification system the Rock-slope Activity Index (RAI). This examination is made through remote sensing, although the RDA and RHRS are not set up to be remotely implemented systems. Each attribute has been considered and analyzed for remote understanding. Attributes that were able to be measured remotely were combined into modified systems. The ability of these modified systems and how they worked in accomplishing the objective of the full system was considered.

As technology advances and new types of data become available, these systems are not designed to use these new resources and updates need to be made to take advantage of higher resolution spatial and temporal data. For this reason, a new type of classification system needs to be created to understand and draw out the information that is currently locked in these new data types.

7.1 Attributes

Table 7.1 lists all the attributes from the three systems and indicates whether the attribute is measured directly or indirectly. Direct measurement is defined as one that the classification system uses as a measured attribute, indirectly measured is defined as something that is either an input into another attribute or is inferred through another attributes. Attributes from the original Pierson system, the RDA system and the RAI were considered in this list. Most attributes have at least two classification systems using them, but there are exceptions, mostly with attributes used in the RDA.

Of these attributes, most were able to be successfully measured remotely, although the accuracy of these measurements depended upon several factors. For the remote assessment, site photographs, mobile lidar, terrestrial based lidar as well as online resources such as google earth were used. The object was to map the attributes on the point clouds then used these mapped clouds to evaluate for each classification. Some point clouds for later scans had photographs mapped on them allowing the real color of the object to be seen with each point. This helped in the mapping process as it was easier to locate features identified in photographs on photograph mapped clouds. When there was no photograph mapping, the accuracy was diminished due to the inability to locate exact features in a 3D point clouds from the 2D reference of a photograph. Even with the photograph mapping, the accuracy was not necessarily as high as desired as the photograph mapping was sometimes misaligned, or areas of several levels of an attribute fell within close proximity.

Table 7.1: Attributes used in the RHRS, RDA and RAI

Attribute	RAI	RDA	RHRS
Altitude and exposure	Indirectly	Directly	Indirectly, Subsequent
Aspect		Directly	
Climate	Indirectly	Directly	Directly
Differential Erosion	Directly	Indirectly	Directly, Subsequent
Disturbance	Indirectly	Directly	
Dynamic Stresses	Indirectly	Directly	
Excavation Method	Indirectly	Directly	
Fracture Aperture	Indirectly	Directly	
Fracture Spacing/Block Size	Directly	Directly	Directly
Overhanging	Directly		
Rock Condition	Indirectly	Indirectly	Directly
Rock Strength	Assumed	Directly	
Rock Structure		Directly	Indirectly, Subsequent
Rock-fall History	Directly		Directly
Slope Geometry	indirectly	Directly	Indirectly, Subsequent
Slope Height	Directly	Indirectly	Directly
Stabilization Measures		Directly	
Static Stresses		Directly	Indirectly, Subsequent
Structural Condition	Indirectly	Indirectly	Directly
Time Since Excavation		Directly	
Vegetation		Directly	
Water	Indirectly	Directly	Directly
Weathering	Directly	Directly	Directly, Subsequent

Some attributes didn’t change greatly across the slopes, for example altitude, static and dynamic stress, excavation methods, time since excavation, and direct disturbance were all very similar or the same at each site. There was variation from site to site, but not significant amounts. Other attributes, such as water at sites were difficult to assess because there was no evidence of surface water in remote surveys and ground water data could not be obtained. There are rivers running near both sites so it is assumed there is an influence of water, but it could not be accurately assessed. For this reason the attributes used for the RDA were only the four main variables: fractures spacing (or block size), fracture aperture, rock compressive strength and rock material weathering grade and for the RHRS structural condition, rock friction, ditch effectiveness, rock fall history, slope height, and block size.

The RDA and RHRS both have quantitative and qualitative attributes with in their systems. As could be expected, fracture spacing/block size, fracture aperture, rock compressive strength, and slope height are all quantitative measurements. The other five variables used were all qualitative to some extent although there may have been some quantitative aspect to the determination of score; engineering judgment was involved in the calculation. All of these attributes, once determined were scaled according to the classification systems scale. These scales produced a number that only could be compared within each classification system, which in itself becomes a qualitative value. This information is useful, but has no real world meaning.

Using the understanding of the classification systems and their attributes that were currently in use, the RAI measures attributes through the use of geomorphological indices that allow an automated processes so that the mapping step can be eliminated. This also eliminates the human error and bias associated with this step. Although still in its early stages, the RAI has already shown that several attributes, including height and overhangs can be directly extracted automatically and then classified providing a higher resolution and more accurate picture of the state of the slope. Other attributes such as weathering and rock condition are measured indirectly through use of roughness in automated processes. Some attributes are variables within the failure probability such as stresses and climate. These attributes were combined to calculate a probability of kinetic energy release a quantitative measurement that has real world meaning.

7.2 Remote Abilities

The main focus of this exercise was to see how well data could be processed remotely and how automated each system can be classified. Each system had different levels of remote classification, varying from RDA, which is a mostly hands on procedure with only a few qualities that are readily identified remotely, to the RAI which was designed as a remote system. Three metrics are used to assess the remote abilities of each system: resolution of data, automation of collection and automation of analysis.

Resolution of data depends upon the source. There were four main sources for this project, lidar point clouds, photographs, field notes and other sources such as maintenance records and GIS layers available through the state of Alaska. Of these, the photographs were found to be the best for identifying RHRS and RDA attributes. Lidar could measure some of the attributes, but normally a photograph was needed to confirm different classes within an attribute. There were some things which lidar was better for, such as elevation and aspect on the RDA and used inclusively for the RAI. Field notes taken in the summer of 2013 were used to help with classifications, although field notes may not be considered remote. Other sources were used in a very limited manner and more as a secondary source than primary for information.

With photographs, automation was not available, although there are some programs which might have the capability to do some of the processing, this study did not employee them. Lidar allowed for automation depending on the attribute. For the RAI, automation was built in, but for the RHRS and RDA automation was available for little to none of the attributes.

Once attributes were mapped onto point clouds, there was some automation in the processing for the RDA through code written specifically for that purpose. The RHRS was easier and faster to do by hand. The RAI was designed as an automated system.

Overall, the RDA and RAI were more conducive to remote analysis using the lidar with the RAI being the best because it is designed for this purpose. There are some drawbacks to having remotely analyzed systems. One is that some information is lost and not conveyed through point clouds or photographs so the accuracy of systems such as the RDA and RHRS are not as precise as if done in the field. Another problem, inherent to the RAI is some information that can only be analyzed at this time through manual processes is missed. For example there is no account for the rock type, which can be distinguished in photographs and when field measurements are taken, but the RAI as it currently stands cannot distinguish between rock types and therefore assumes a uniform rock, which assumption can be in gross error in some situations.

7.3 Comparison

Table 7.2 is a comparison between each of the systems and how they each preform or handle different aspects of an analysis from the use to the final score. Each system was designed for a purpose and works well at their purpose but not all systems are compatible with remote analysis. Overall analysis of the RHRS was easier to remotely implement by hand, because it was chosen to do it at intervals of 10 meters of slope. The RDA could have been done similarly, but it was decided to map the attributes to a point cloud which added to the labor. The most laborious part of the RAI is the processing of point clouds into usable form, i.e. georeferenced and filtered. Once that is done implementation can easily be done with an executed code. Both of these systems can be remotely implemented, but the outcome will not be the same if done in the field.

Full automation cannot be achieved by either the RHRS or RDA. There needs to be a human aspect to the rating with these systems. The RAI was built to be automated and therefore preforms well in this aspect.

Table 7.2: Comparison between the three classes

	RAI	RDA	RHRS
Use	For lidar scans to characterize the potential hazard of a slope. Can be a first run to find areas to target for further study.	Assess the progressive breakdown of rock slopes and determine mitigation techniques.	Classify hill cuts mostly along transportation corridors in a standardized method for communication of potential hazard and risk
Labor Process	Once clouds are acquired, the process is: remove vegetation, run software process, interpret the results.	Field work to measure discontinuity spacing, aperture, classify weathering and find rock strength. Classification of additional attributes, most done as observations in the field	Field work, normally done as an assessment filling out a questionnaire and making some measurements.
Automation	Once the point cloud is processed, this can be run through software to automatically classify and create hazard mapping	None	None
Ability to be done remotely	Can be done entirely remotely with point clouds, point clouds need to be gained on site	Some remote ability with photographs and point clouds	Some remote ability, GIS information can help classification
Field work required	None	Mostly done by field work	Field work required
Labor requirements	Processing of lidar cloud	Field work assessment	Field work assessment
Skill set needed	After cloud is acquired and georeferenced, knowledge of software including 3d point cloud software visualization	Technical training on how to find rock strengths is easy with small introductory coarse	Technical training on how to fill out the system
Interpretation	Several ways of interpretation, there is looking at scores overall for sites, looking at a site sectioned into 10 m sections or looking at the actual point cloud.	A number for phase one of the system can be fed into the other phases with relevant information to find possible solutions to deteriorating slopes	High scores are unstable, low scores are stable. Can break apart the scoring, if available to understand why a score is high/low
Meaning of score	Amount of potential energy released from a slope	Arbitrary number	Arbitrary number

Agreement among the systems is difficult to fully assess because they measure slightly different aspects of the rock slope. Also, each system has its own scale and therefore cannot be directly related. Figure 7.1 shows a map of four sites with scores from each of the three systems. The scale is somewhat comparable, with blue being the lowest and red being the highest. The RHRS scores use the exponentially increasing scale that is indicative of the level of severity. The RAI used 10 mJ as a maximum, although there can potentially be scores higher than this, all of the sites per cell score were less than this. The RDA is on the 0-100 scale as used in the paper.

For the most part, the three systems score towards the lower end of their scales for all the sites. All three systems agree on Glenn Highway Milepost 87 on the level of severity, but the other three sites have one system each that varies from the level of severity of the other two. The site with the most disagreement is Parks Highway 240.9 where the RAI has a score that is two levels higher than the other two systems.

Figure 7.2 shows Glenn Highway milepost 87 with the three systems, including the class system for the RAI and a red, green, blue (RGB) mapped point cloud for comparison. Both the RHRS and RDA are coarse due to visual classifications and field techniques. In comparison the RAI has greater resolution because it takes advantage of the finer resolution lidar data. The RAI has a pixel level resolution. Comparing the systems at a site level is difficult because of the different resolutions found in each system. This being said, there is some agreement with the RAI and RDA in low end values, but the similarities are limited to these portions.

7.4 Conclusion

Each system works well in its intended use, but extending the use of primarily field technique systems to use with remote sensing techniques such as lidar highlights incompatibilities between remote and field techniques as well as opens up to loss of data both through measurements that are hard or impossible to take remotely as well as loss of fine detail offered by remote sensed technology.

There is a need for tools for advancing technologies such as lidar, to process and understand the large amounts of data that are received from these methods. Currently these methods do not exist and valuable data is missed because there is no way to extract and understand it. The RAI fills part of this need, allowing rapid assessment of rock slope point clouds that allow users to further focus on areas of concern and possible hazards.

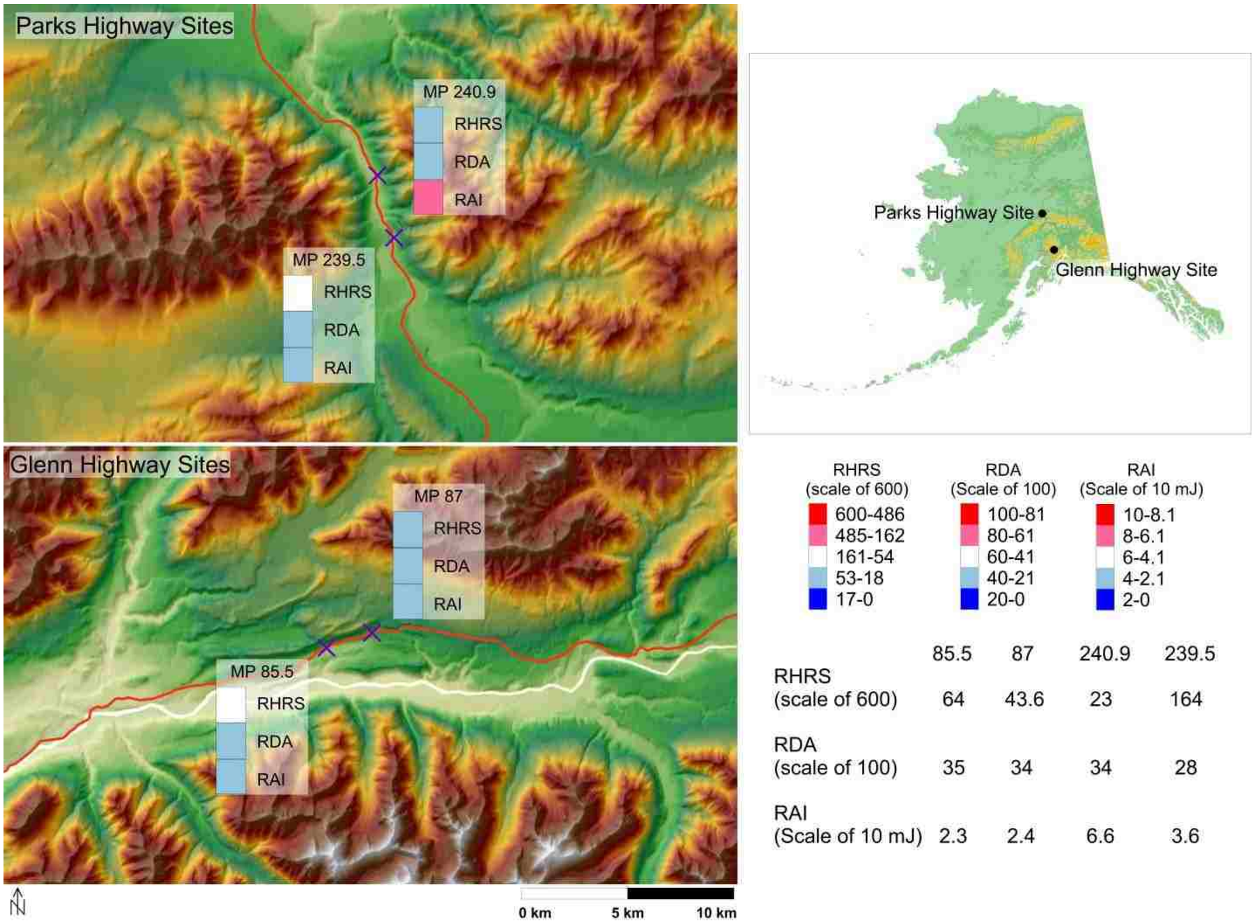

	85.5	87	240.9	239.5
RHRS (scale of 600)	64	43.6	23	164
RDA (scale of 100)	35	34	34	28
RAI (Scale of 10 mJ)	2.3	2.4	6.6	3.6

Figure 7.1: Comparison of the three systems, RHRS, RDA and RAI for four sites along Parks and Glenn Highway.

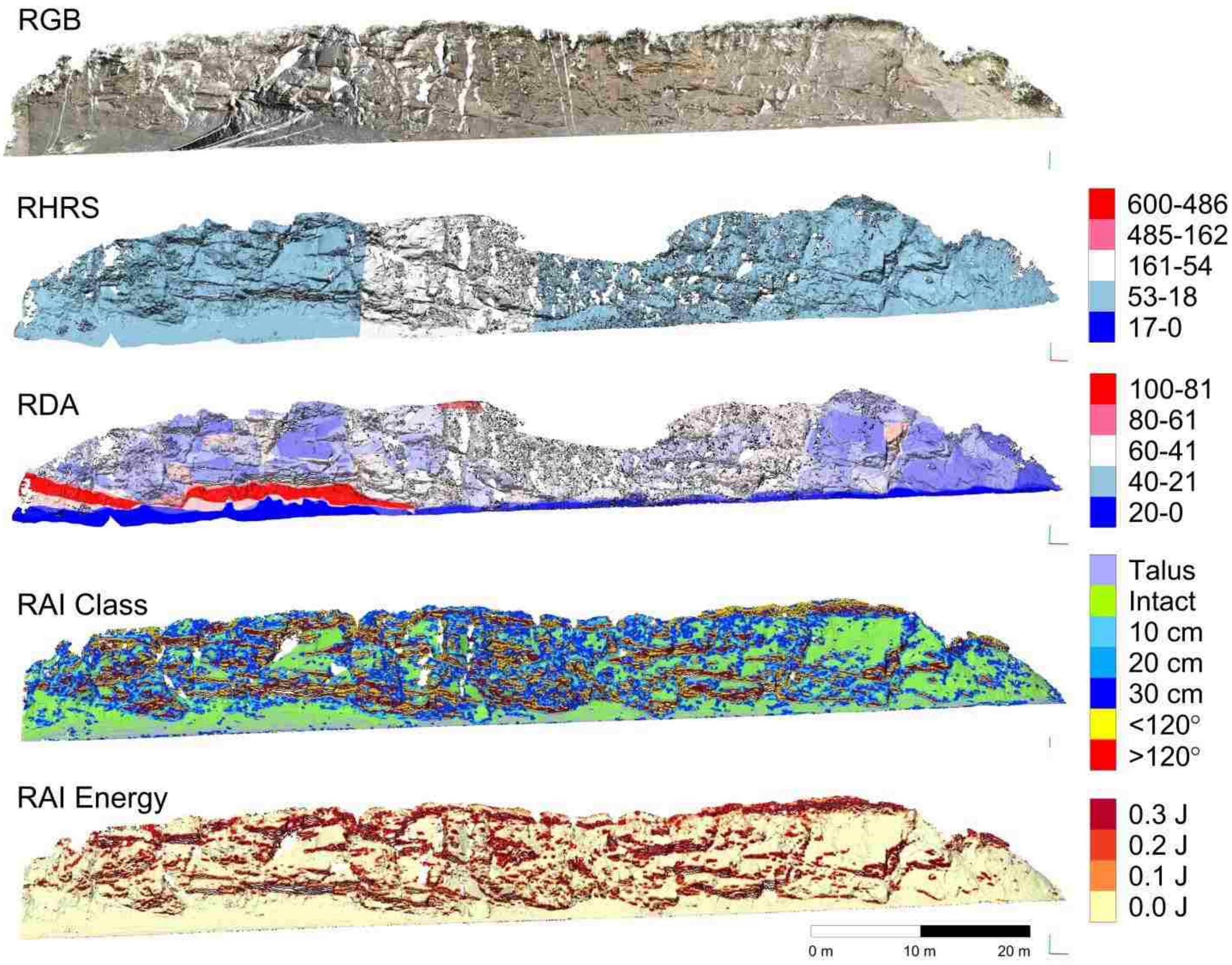

Figure 7.2: Point clouds for Glenn highway Milepost 87 showing the three systems, RHRS, RDA and RAI along with the RGB point cloud of the site.

8. Frequency Magnitude

Frequency magnitude relationships can help predict the future failure of slopes given that the past is representative of the future. For this project we based our model on Barlow et al. (2012) where cliff erosion was represented using negative power law scaling. This chapter applies the principles discussed by Barlow et al. (2012) and applies them to the RAI classification system for making “forward” predictions and a simple forward prediction model.

8.1 Change Detection Method

Temporal series of lidar scans can be used in the creation of change detection. When a newer scan in a series is subtracted from an older, the change is shown as differences between the two scans. Using the time between scans, a rate of erosion or accretion (deposition) can be quantified.

To understand frequency magnitude relationships within the slope, a magnitude of failures must first be established. This required the identification of individual failures (Figure 8.1) which was accomplished by finding individual clusters of cells that had negative change. (Olsen et al 2015, submitted) Once a cluster was identified, a volume was calculated through the difference between the two scans. The result of this was a list of failure surface volumes. Using the RAI classification, a class was assigned according to the predominate class within the failure assuming that the predominant class was initiating source.

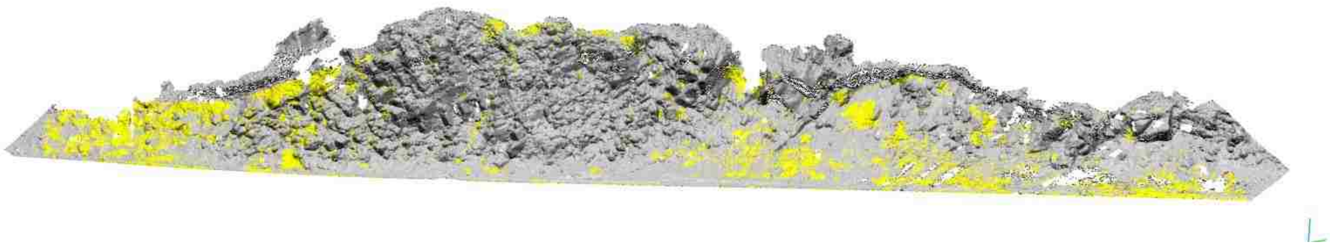

Figure 8.1: Failure clusters at Glenn Highway Milepost 85.5. Individual failures can be seen in yellow.

8.2 Sites Used

In total, 10 sites were included in this exercise. These were chosen because of availability of three scans, spanning from 2012-14 (Table 8.1). Two sets of scans were processed by the RAI Hazard Rating Program discussed in Chapter 5. The output for the magnitudes of failures was used and analyzed using an Excel spreadsheet following the Barlow et al. (2012) methodologies.

Table 8.1: Data availability for all twelve sites along Glenn (LL) and Parks (GG) Highways.

	2012	2013	2014
LL87 (LL16C)	x	x	x
LL85.5 (LL14B)	x	x	x
LL14C	x	x	x
LL14E	x	x	x
LL16A	x	x	x
LL16B	x	x	x
LL16D	x	x	x
GG07D	x	x	x
GG07E		x	
GG08B (239.5 n)		x	
GG08C (239.5 s)	x	x	x
GG10 (LL240.9)	x	x	x

8.3 Error Sources

There are several sources of possible error that are introduced into the calculations. This section identifies three of those sources: clustering error, use of non-classified data and binning errors.

8.3.1 Clustering Errors Within Change Detection

The error in change detection comes from two primary sources: cloud alignment and noise errors. Cloud alignment issues are caused by misalignment of scans due to geo-positioning and scans not capturing the exact same points on surfaces during multiple scans. The first issue of misalignment is improved by good planning and execution of scans with strong GPS and control points. Error due to scan alignment will also depend upon precision of instrumentation and cannot be entirely eliminated, but can be kept to a minimum. Noise within a cloud is caused by many different sources as discussed in Section

5.3. One of the main sources of noise is vegetation growing on a slope. This can be reduced by filtering the point cloud and manually removing the vegetation; however, this will not eliminate all vegetation points. For the following analysis, the vegetation was not removed in all the clouds. If vegetation was removed in one year, there was an effort to do so in subsequent scans, but quality of removal may vary. Figure 8.2 shows vegetation on a slope, while some of the vegetation is easy to pick out, not all of it is caught with filters.

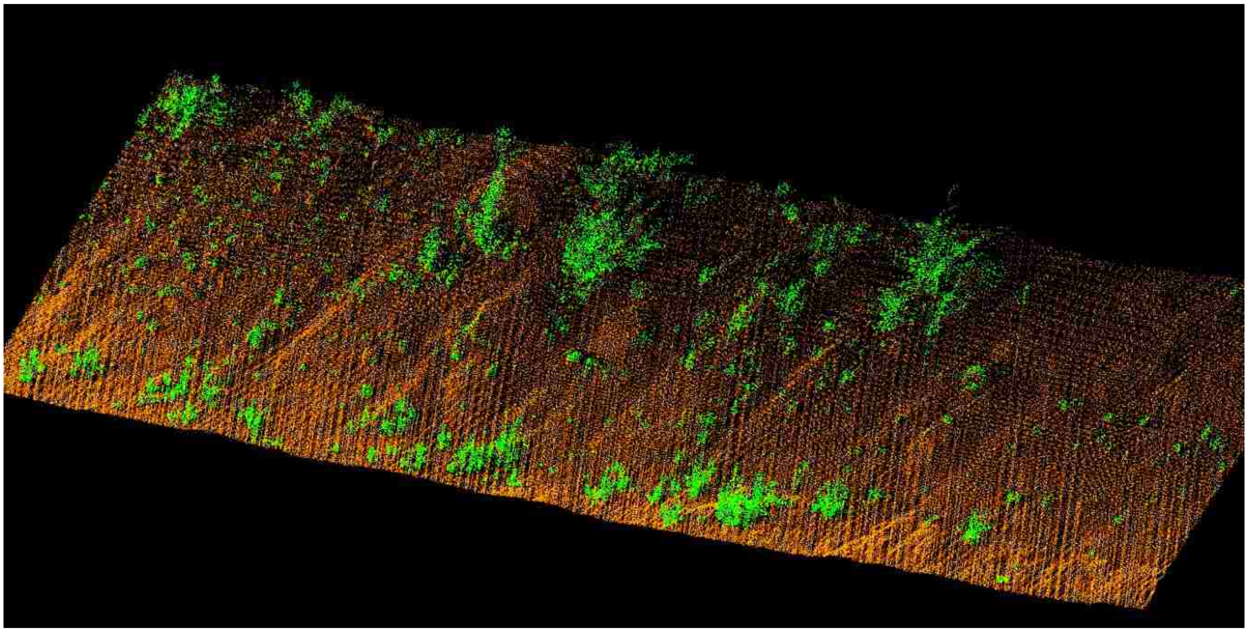

Figure 8.2: Lidar point cloud showing slope in orange and vegetation in green.

8.3.2 Use of non-classified Data

In each site, there are failures that receive no classification. These were neglected for the prediction done with the classifications but were kept for the prediction with no classification. Table 8.2 shows the volume of non-classified failures and the percent they are of the total volume for the sites. The most significant percent of total is slightly over 1%; therefore it is assumed that this does not make a significant impact on the results.

Table 8.2: Volume represented in each scan sets of non-classified failures.

	Volume (m^3)	Percent of total
LL87 12-13 (LL16C)	0.03	0.05
LL87 13-14 (LL16C)	0.00	0.01
LL85.5 12-13 (LL14B)	0.03	0.03
LL85.5 13-14 (LL14B)	0.06	0.17
LL14C 12-13	2.97	0.09
LL14C 12-13	22.57	1.04
LL14E 12-13	1.66	0.27
LL14E 13-14	4.26	0.59
LL16A 12-13	0.02	0.04
LL16A 13-14	0.00	0.04
LL16B 12-13 (86.9)	0.06	0.09
LL16B 13-14 (86.9)	0.03	0.19
LL16D 12-13	0.05	0.10
LL16D 13-14	0.02	0.77
GG10 12-13 (LL240.9)	1.55	0.38
GG10 13-14 (LL240.9)	0.17	0.04
GG07D 12-13	0.95	0.24
GG07D 13-14	0.53	0.03
GG08C 12-13 (239.5 s)	1.63	1.06
GG08C 13-14 (239.5 s)	8.82	0.73

8.3.3 Binning and Regression Fits

Each site was divided into classes and binned following methodology adopted by Barlow et al. (2012). The quantity of bins varied from site-to-site and class-to-class depending on the minimum and maximum volumes of failures. It is assumed for this exercise that the adopted limits are also the limits of the possible failures so accuracy can be checked. In real predictive models, a wider range may be used depending upon history of failure at the site. Most data covered the lower end of the volume spectrum (i.e., from about .0001 to .2 m^3). Although the lower bound of measurable data is 0.01 m^3, data below this point did not significantly contribute to overall volumes of failures. To assess the overall accuracy of the model, these predictions and observations are retained. For a final model as will be discussed in the forward prediction section, this limit should be set.

Another error results from there being not enough bins for a good fit. A standard practices for regressions is to have at least 10 observations for every predictor for linear regression (Green, 1991). The data ranges from 1 to 13 observances with an average of 7.6. For purposes of observation prediction analysis, observances of two or more were used. For actual model, a regression should have at least three observances.

Overall the regressions had high R^2 values (typically between .98 and .99). There are four values that fall below 0.9, an example can be seen in Figure 8.3 which shows the overhang less than 120 degrees for site LL14E between 2013-14. When the end points were removed, the predicted value increases as can be seen in Table 8.3 which shows with and without the two points included. With the two points removed, the R^2 value increases but the prediction is further from the observed. In examining the other low R^2 value models, no discernable pattern of R^2 values and ability to predict accurately was found.

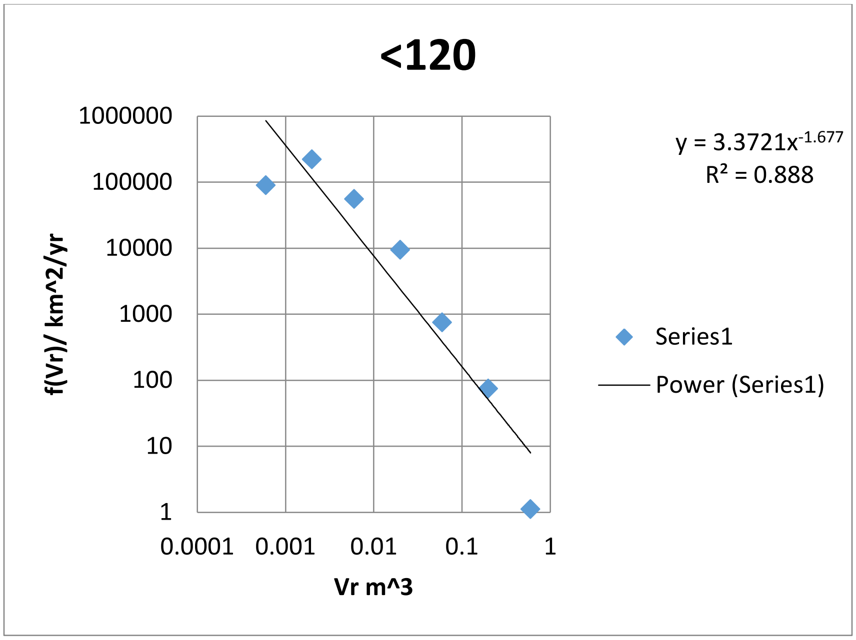

Figure 8.3: Regression of <120 on Glenn Highway MP 87

Table 8.3: Difference in regressions

	Predicted Volume	Percent of observed	R^2
Observed	9.628		
Predicted as seen in Figure 8.3	10.603	110%	.888
Predicted with both end points removed	21.654	225%	.9875

8.4 Models

Three models were used to analyze frequency magnitude relationships. By using three models, results can be compared with each other to see how classification works in prediction. The models are outlined in table 8.4.

Table 8.4: Models for analysis of frequency magnitude relationships.

RAI Classification	Talus	Intact	10 cm	20 cm	30 cm	<120	>120
Reduced RAI Classification	Talus	Intact	Sized (10, 20, and 30 cm)			Overhang	
No Classification	All Classes						

8.5 A-Beta

Barlow et al (2012) used a model developed by (Brunetti et al 2009):

$$V = AN^{-\beta}$$

Where V is the volume, N is the number of failures and A and β are empirically-determined constants.

8.5.1 A term

The A term on a log-log scale is representative of the value at 1. As the A term grows, the line will move up the scale as seen in Figure 8.4. This term is also representative of the activity of a site. It was found that as the A term increased, higher volumes of material were more likely to fail. Figure 8.5 is a box and whiskers plot of the A value according to class.

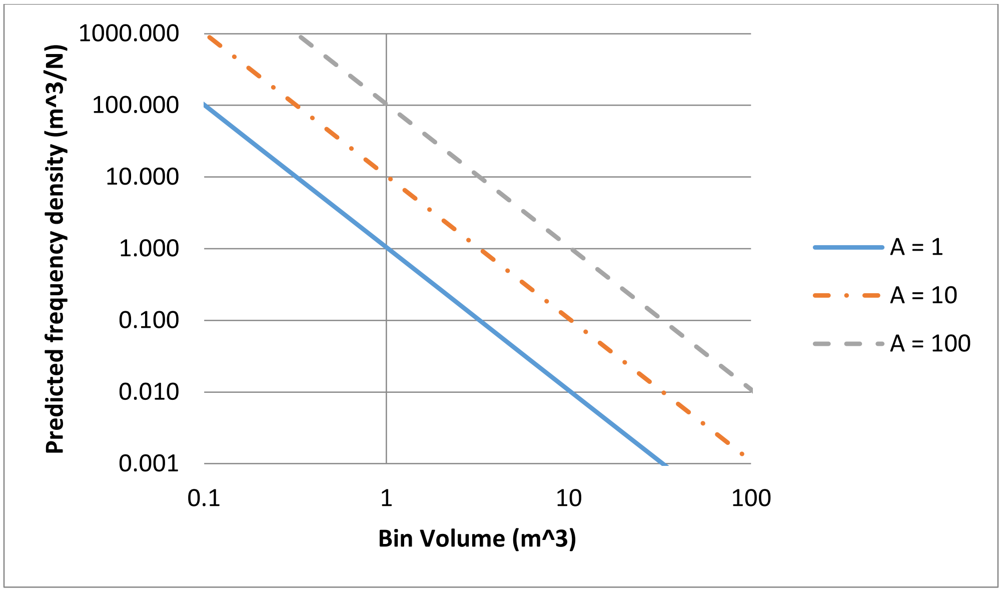

Figure 8.4: A values graphed with beta being kept constant. As the A value increases, so does the intercept with 1.

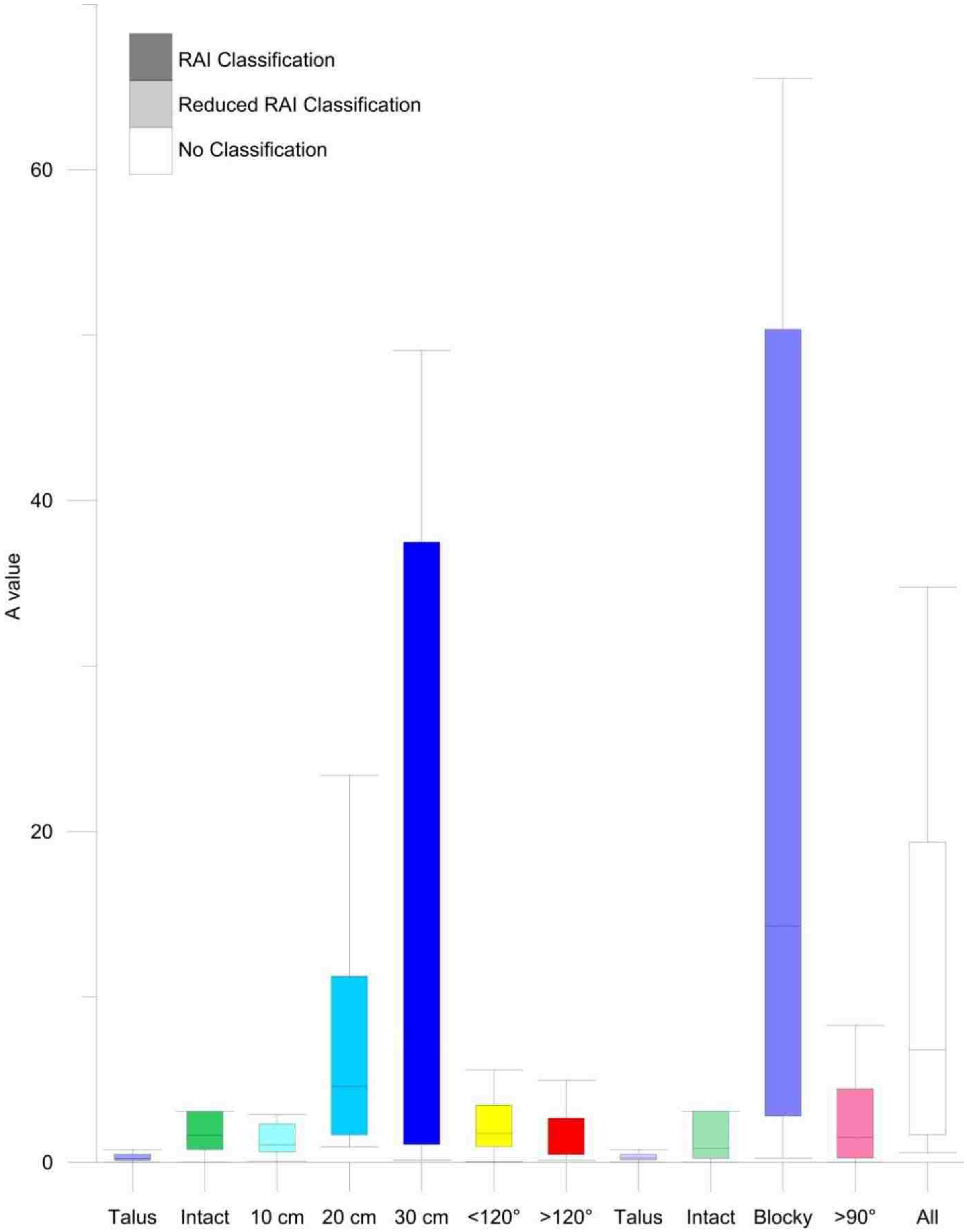

Figure 8.5: Box and whiskers plot of A values for all sites.

The highest A terms were found in the 30 cm sized material. When examining the average failure volume for the 10 sites (Table 8.5), it is clear that 30 cm has the largest amount of failure followed by 20 cm, which has the second largest A value. Talus, 10 cm and >120° all have low A values and low failure volumes. Figure 8.6 is the maximum values of volume overlaid with the corresponding maximum A values.

Table 8.5: statistics on failure volumes for the 7 RAI classes

	Talus	Intact	10 cm	20 cm	30 cm	<120	>120
Average	4	60	4	148	324	14	2
Standard deviation	8	129	6	340	659	23	4
Max	35	607	28	1594	2665	89	15

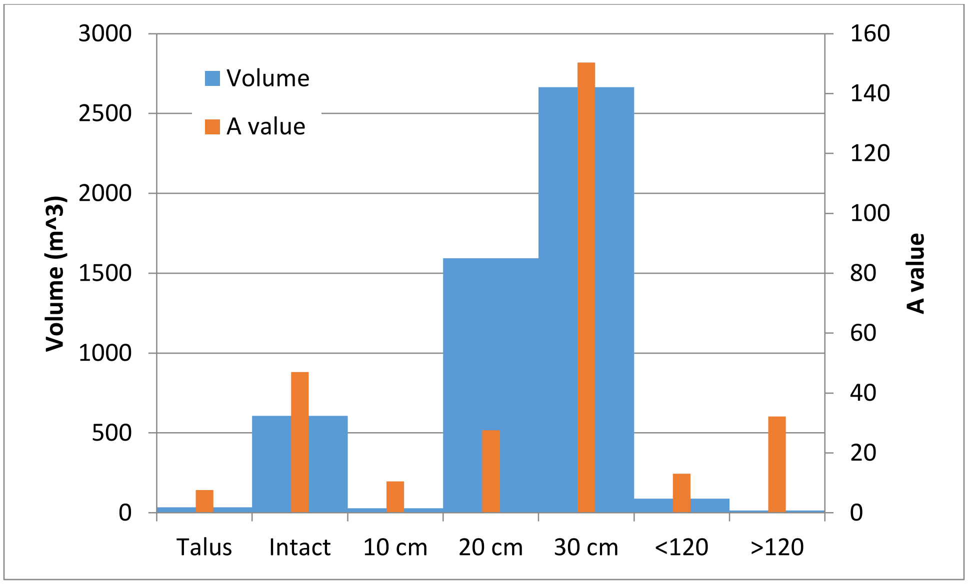

Figure 8.6: Maximum volumes and A value per class. The highest A value corresponds with the highest volume.

8.5.2 Beta Term

Beta signifies the relationship between large and small events. Table 8.6 and Figure 8.7 illustrate a theoretical example of predicted failures and volumes for changing volumes while the A value is constant. For small betas (<2), the predicted failures stays the same over all the bin sizes while the predicted volume decreases with bin size. For large betas (>2) the amount of failures exponentially rises with smaller bin size along with volume in each bin.

Table 8.6: Predicted failures and volumes over bin sizes .06 to 200 m^3.

	Predicted Failures (N)			Predicted Volumes (m^3)		
Bin Size (m*3)	**beta = 1**	**beta = 2**	**beta = 3**	**beta = 1**	**beta = 2**	**beta = 3**
200	1.187	0.005	0.000	285.360	1.187	0.005
60	1.230	0.018	0.000	94.041	1.230	0.018
20	1.160	0.054	0.003	27.886	1.160	0.054
6	1.202	0.176	0.029	9.190	1.202	0.176
2	1.133	0.523	0.266	2.725	1.133	0.523
0.6	1.175	1.723	2.814	0.898	1.175	1.723
0.2	1.107	5.111	26.022	0.266	1.107	5.111
0.06	1.148	16.840	274.988	0.088	1.148	16.840

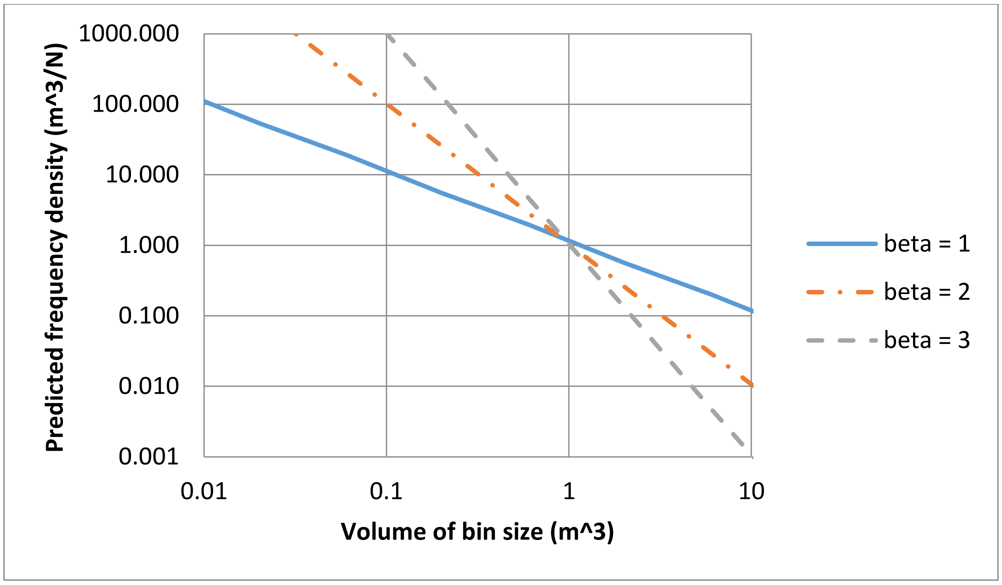

Figure 8.7: Illustration of changing beta values while A value stays the same. As a beta increases smaller events to larger events rise.

Figure 8.8 is a box and whisker plot of the beta values for all the sites. A trend can be seen, especially in the sizes (10, 20 and 30 cm) and overhang (<120 and >120). As the sizes or slope increase, the beta value drops signifying that there will be more large failures than small failures. For most individual sites this holds true when all three years of data are analyzed. (See Appendix G)

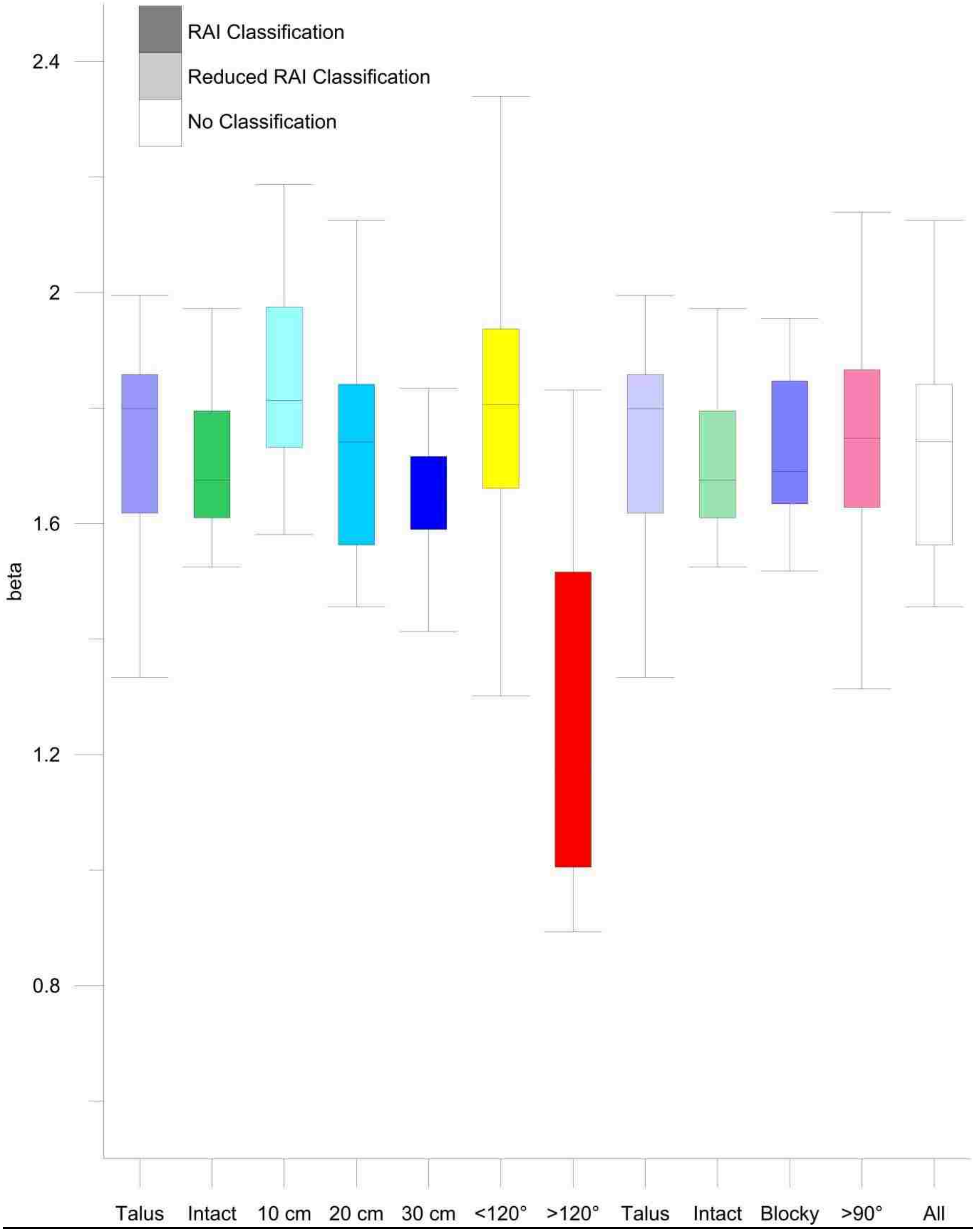

Figure 8.8: Beta values for all sites. General trends occur in the 10 cm, 20 cm and 30 cm and overhang with a downward trend. These downward trends

When considering the relationship of volume to beta, the lower the beta value, the higher the overall volume as can be seen in figure 8.9. Which can be explained partially by larger failures occurring in classes were the relationship between small and large failures is decreasing.

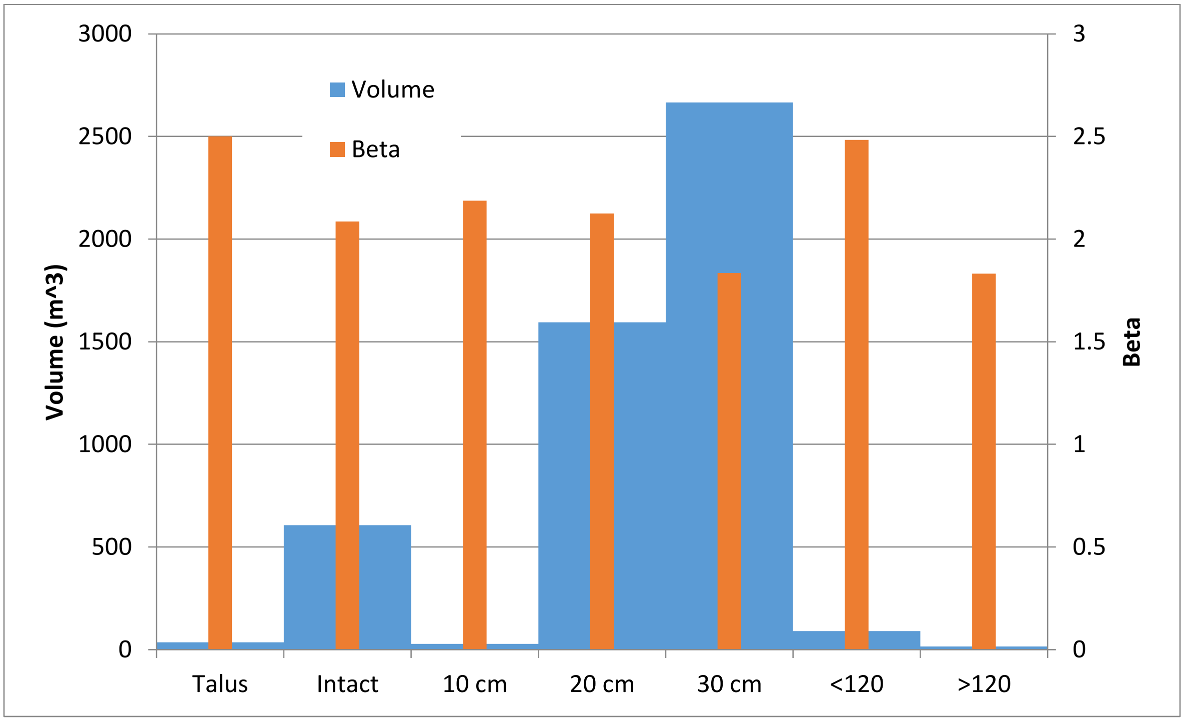

Figure 8.9: Maximum volume and beta value per class. As the beta value goes down, the ratio of large to small events increases which explains the large increase in maximum volume for the smallest beta values.

Overall the A and beta values demonstrate trends in the classes which would be expected. Talus failures are likely to be small in size and not very frequent. Size categories have increasing volume as well as size of failure. Overhang are less frequent, but as the slope increases, the size of failure increases.

8.5 Model accuracy

Parameters A and beta govern the performance of the model. If these values do not predict the observed volumes loss, they are will not make reliable forward predicting models. All three models are now considered to see how well they compare against each other. Figure 8.10 illustrates Table 8.7

which is the ratio of predicted to observed values. The three models are very similar in accuracy with no model out preforming the other models.

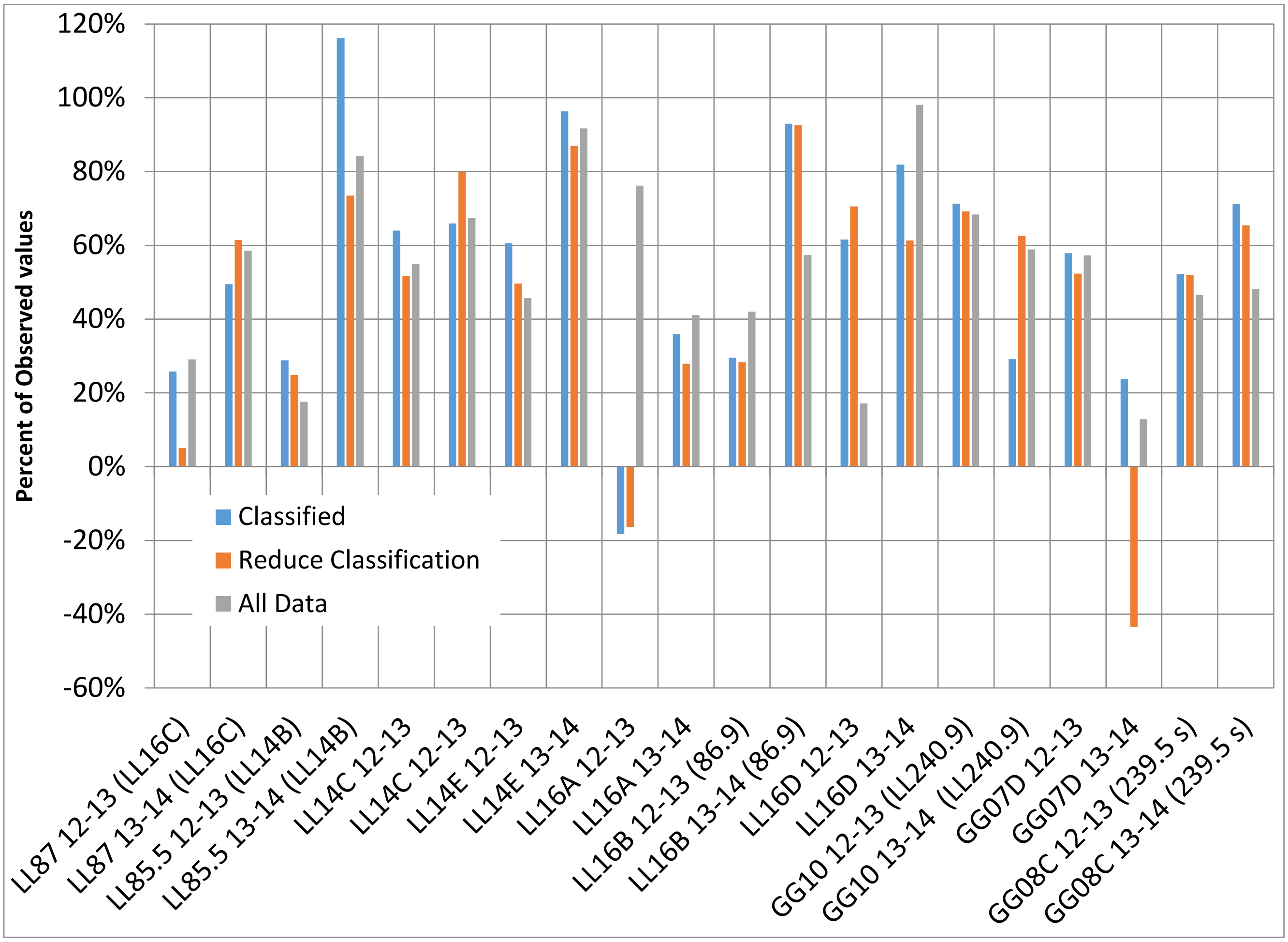

Figure 8.10: Percent of predicted values to observed values assuming that 0% would be equal.

Table 8.7: Percent of predicted values to observed values assuming that 0% is equal. Most of the models over predict the volume of failures in comparison to the observed.

	Classified	Reduce Classification	All Data
LL87 12-13 (LL16C)	26%	5%	29%
LL87 13-14 (LL16C)	49%	61%	59%
LL85.5 12-13 (LL14B)	29%	25%	18%
LL85.5 13-14 (LL14B)	116%	73%	84%
LL14C 12-13	64%	52%	55%
LL14C 12-13	66%	80%	67%
LL14E 12-13	61%	50%	46%
LL14E 13-14	96%	87%	92%
LL16A 12-13	-18%	-16%	76%
LL16A 13-14	36%	28%	41%
LL16B 12-13 (86.9)	29%	28%	42%
LL16B 13-14 (86.9)	93%	92%	57%
LL16D 12-13	62%	71%	17%
LL16D 13-14	82%	61%	98%
GG10 12-13 (LL240.9)	71%	69%	68%
GG10 13-14 (LL240.9)	29%	63%	59%
GG07D 12-13	58%	52%	57%
GG07D 13-14	24%	-43%	13%
GG08C 12-13 (239.5 s)	52%	52%	47%
GG08C 13-14 (239.5 s)	71%	65%	48%

Overall, all the three models preform similar with the reduced classification preforming slightly better (Table 8.8). When individual classes are examined as in Figure 8.11, one class, >120°, predicts higher than the rest of the classes. When data is examined closer, the average number of data points for the >120° class is about 100 points compared to the next smallest of talus at 880 (Table 8.9).

Table 8.8: Average and standard deviation of the three models.

	Classified	Reduce Classification	All Data
Average	155%	148%	154%
Standard Deviation	30%	34%	23%

Considering these factors, the reduced classification model predicts consistently across the four classes, although the prediction is nearly 1.5 times the observed. This needs to be considered during modeling of forward predictions.

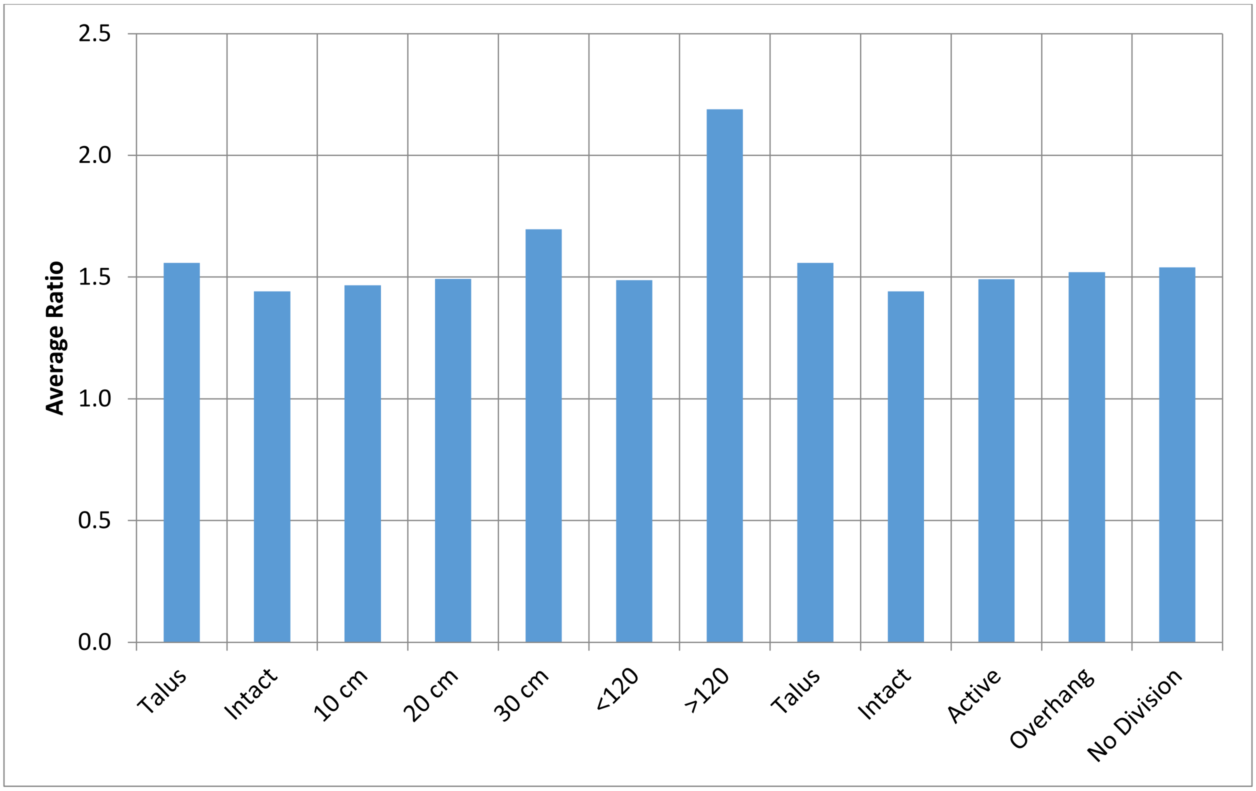

Figure 8.11: Average ratio by classes.

Table 8.9: Average number of failures by class per site

Talus	Intact	10 cm	20 cm	30 cm	<120	>120
886	4088	2001	6257	7523	1667	101

8.6 Forward predictions

For a forward prediction requires two values a volume for a bin determined by power relationship's (A and beta) and a probability of occurrence of failure size. The power law relationship was discussed in Section 4. For each site, two sets of data exists, 2012-13 and 2013-14. For the forward prediction, an average of A and beta were used at each site. Table 8.10 is a list of A and beta values for the ten sites.

Table 8.10: A and beta values using the reduced RAI classification system for the 10 study sites.

	talus		intact		blocks		overhang	
	A	beta	A	beta	A	beta	A	beta
LL87	0.33775	1.685	1.6578	1.679	3.4324	1.7725	1.9322	1.559
LL85.5	0.239435	1.992	0.3719	1.7115	7.06705	1.673	0.44235	1.8935
LL14C	1.2285	1.8785	5.96105	1.681	171.18	1.685	15.507	1.791
LL14E	0.88915	1.706	11.1647	1.6165	50.502	1.6585	2.3022	1.9565
LL16A	0.3942	1.603	1.7276	1.6045	1.85785	1.7855	0.19565	1.7815
LL16B	0.3079	1.502	4.23645	1.461	1.1856	1.7325	0.4608	1.449
LL16D	0.02315	0.8155	1.47985	1.605	2.4645	1.6825	0.6056	1.56
GG10	0.2392	1.918	0.51475	1.9975	36.239	1.6965	2.35675	1.934
GG07D	0.2341	1.767	5.40295	1.679	41.426	1.776	6.524	1.759
GG08C	3.78625	2.164	24.1516	1.849	39.8955	1.912	5.3458	1.7835

The data shows that not all sizes of failures happen each year. For this quick approximation for forward prediction, the A and beta terms have been fixed at the average for each site, in the real world, these would vary from year to year within a range. To simulate that, the maximum volume at each site was considered to vary according to what had been seen at all the sites. The maximum bin for each class at each site was counted and divided by the total bins to calculate the probability that that bin was the largest bin for a given year. Assuming that the smallest failures would happen each year, the probability that the bin would be the largest was subtracted from the total probability as the bin size increased resulting in Table 8.11.

Table 8.11: Likelihood of failures occurring at each bin size.

Bin size	talus	intact	active	overhang
20000	0%	0%	5%	0%
6000	0%	0%	10%	0%
2000	0%	5%	10%	0%
600	0%	10%	19%	0%
200	0%	15%	29%	0%
60	5%	24%	53%	5%
20	10%	62%	67%	10%
6	24%	72%	72%	19%
2	29%	76%	95%	43%
0.6	43%	81%	100%	57%
0.2	62%	95%	100%	81%
0.06	71%	100%	100%	100%

Combining these two values, a volume can be calculated on a yearly basis and multiplied by the number of years to predict into the future. This is illustrated in figure 8.12.

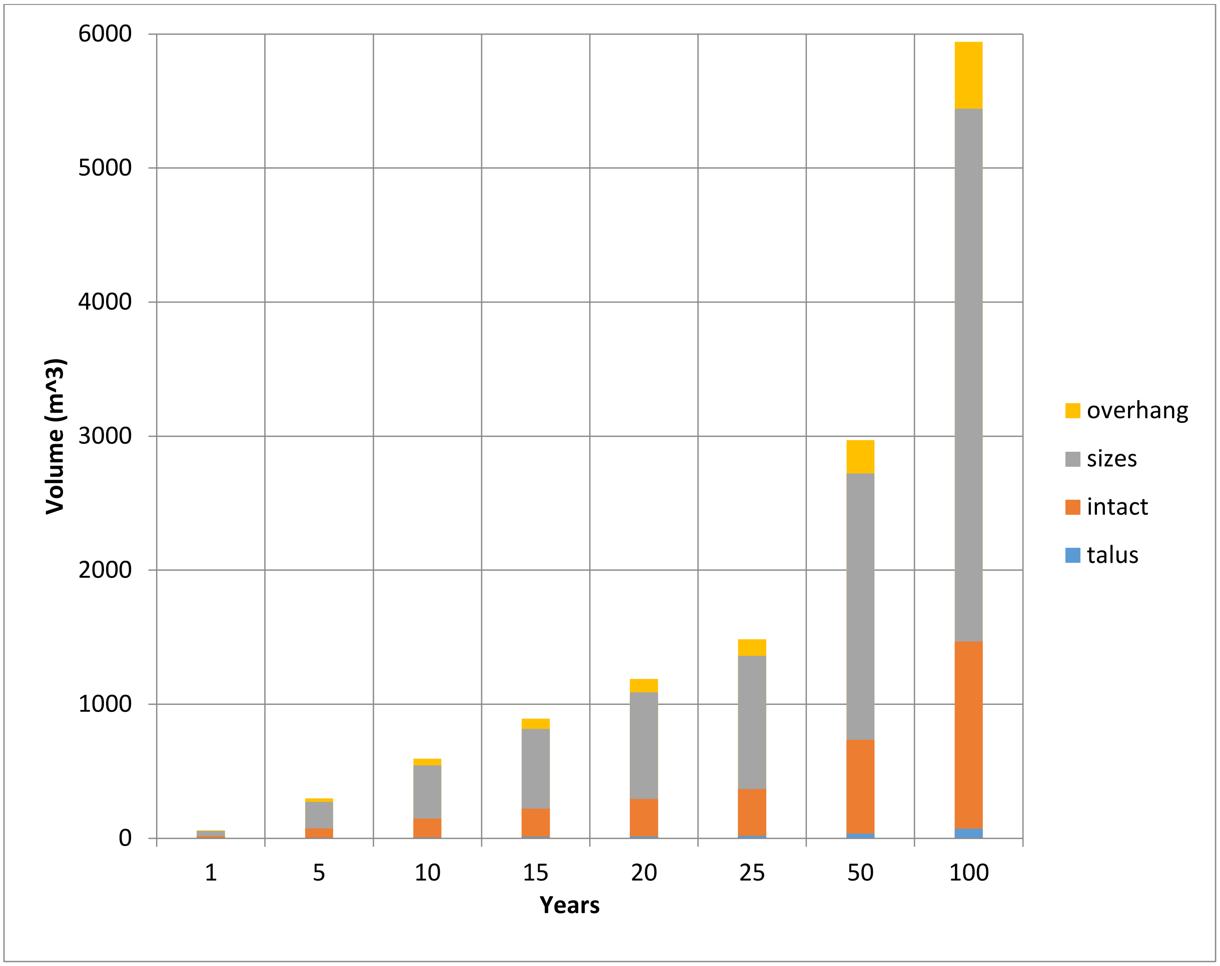

Figure 8.12: Volumes for forward prediction for site LL87.

9. Conclusion

Lato (2012) noted that there needs to be a new classification system to use with the high quality data that is now able to be captured through use of lidar and other remote sensing techniques. A system needs to be easily understood by those that use it as well as have real meaning so it can be interpreted for quality use. Data received from remote sensing techniques can be overwhelming. High resolution stores valuable information in it, but when analyzed at such a resolution, it can be hard to understand and even harder to interpret. The RAI system works to simplify data, but also keep valuable resolution. This system can also use future predictions of failure so allocation of resources for maintenance and operations can be made for better asset management

Appendix A: Glenn Highway and Parks Highway scan sites

Figure A1: Parks Highway sites, also designated as Glitter Gulch (GG)

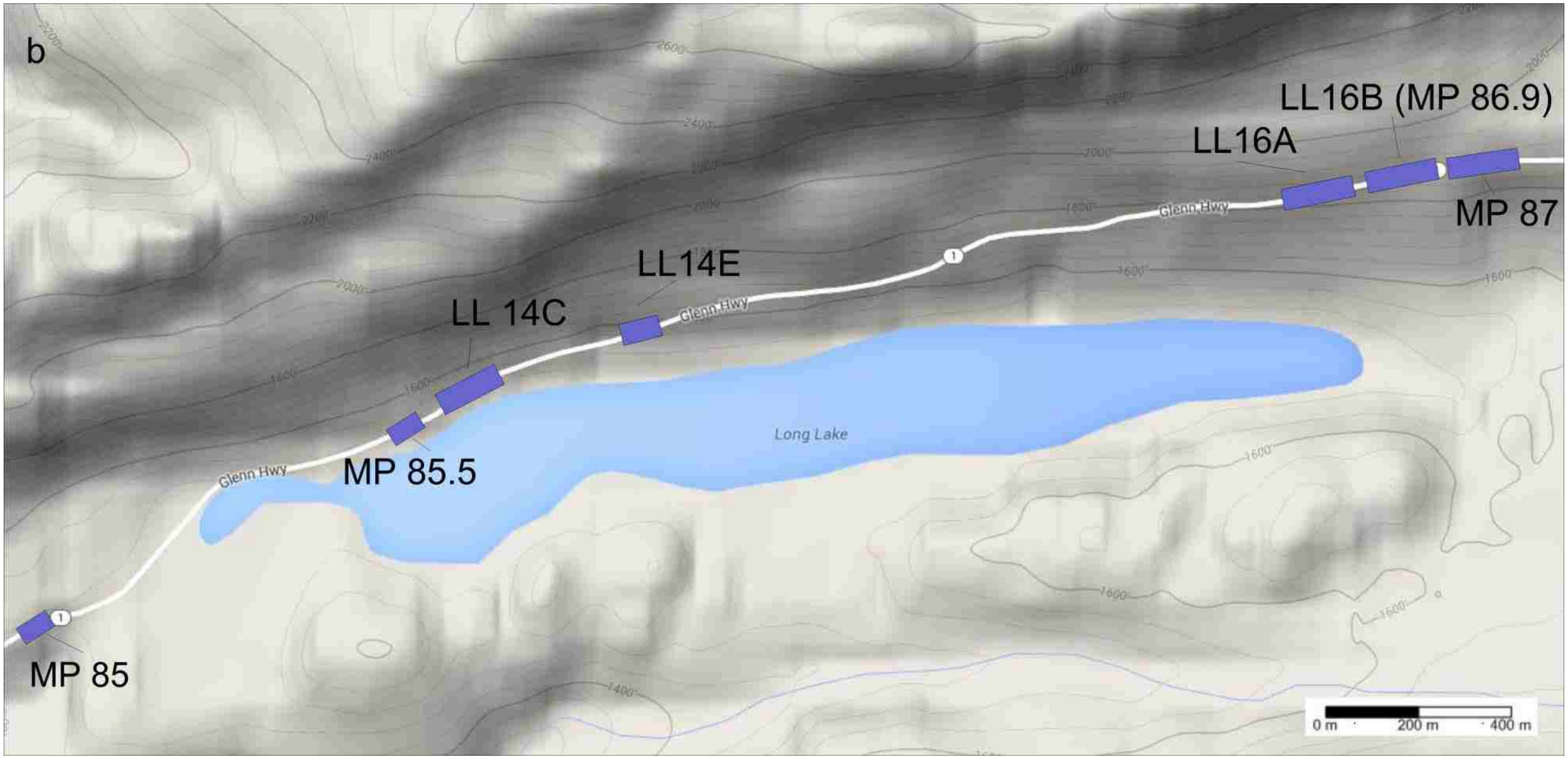

Figure A2: Glenn Highway sites, also designated as Long Lake (LL)

Appendix B: Schmidt Hammer

The Schmidt hammer is a non-destructive method to measure rock hardness. Originally developed for use with concrete (Schmidt 1951) and has been since adapted to use in geologic settings [(Deere & Deere, 1988); (Sachpazis 1990). The hammer is spring loaded and when pressed orthogonally against a sample automatically releases its plunger which records a rebound height. This rebound height can then be correlated to the actual hardness of the rock or strength of the rock.

Sampling

The Schmidt Hammer test was performed on samples of the five lithologies found in the Parks Highway and Glenn Highway study areas. Of these samples, the more prevalent rock at each site was sampled in more than one location. For this reason, Sandstone and Healy Schist both have three samples while the Chickaloon Carbonaceous Siltstone and Chickaloon Formation Mudstone and the Mafic Intrusive all have one sample each. Samples of these rocks were taken for further identification and examination. Samples were taken in August of 2013.

Figure B1: Schmidt hammer sites along Parks Highway

Figure B2: Schmidt hammer sites along Glenn Highway

Sample Size

Each rock sample for the Alaska sites had between 16 and 22 samples. ASTM D873-05 standards suggest 10 samples be taken, averaged and any sample more than 7 units greater or less than the average is removed and the remaining samples are averaged for the R_h (Rebound Value) (ASTM 2005). Ericson (2004) states abnormally high numbers are rare, but abnormally low numbers are quite common because the plunger can easily hit or crush grains in the sample thus dispelling energy. Comparing the top 50, 80 and 100 percent of the R_h values Ericson examined the statistical difference and found that there was not an appreciable change suggesting that all values be used. Because of the possibility of outliers, it was determined to check our raw data to see if any numbers were ±7 of the next lowest or highest number and none were found. For this reason the averages were calculated using all the measured data and by using ASTM standard. Table B1a and B1b shows the averages of the rebound values which show as Ericson found there is not a significant change in the averaged values when the ASTM method being at most +1.3. Because the measured value is more conservative, it was determined to use this as the final rebound values.

Table B1a: Averages of Rebound Values Parks Highway

GG	Measured Average	Count of Samples	ASTM Calculated Average	Count for ASTM Average
Sandstone	43.0	22	43.4	21
Sandstone	39.1	20	39.5	19
Sandstone	45.8	20	46.5	14
Chickaloon Carbonaceous Siltstone	24.5	19	25.5	14
Chicaloon Formation Mudstone??	28.0	16	29.3	14

Table B1b: Averages of Rebound Values Glenn Highway

LL	Measured Average	Count of Samples	ASTM Calculated Average	Count for ASTM Average
Healy Schist #1	60.2	17	60.2	17
Healy Schist #2	63.3	16	65.2	13
Healy Schist #3	67.3	19	67.3	19
Mafic Intrusive (Thm)	60.3	20	62.2	17

Angle Correction

These correlations are for when the hammer is held horizontal to the sample which is impossible to do in many geologic settings. For this reason, there needs to be an angular correction of the value before applying the correlation for the rock strength.

Basu and Aydin (2004) outlined the method of normalizing the Schmidt hammer rebound values. When the hammer is in the horizontal position, the energy released is equal to the kinetic energy of the piston.

$$0.5kx_1^2 = 0.5MV_1^2 \qquad (1)$$

Where:
K = spring constant
x_1 = initial stretch of spring
M = mass of piston
V_1 = Velocity of piston as it touches the plunger

As it rebounds, the energy must also be equal:

$$0.5kx_2^2 = 0.5MV_2^2 \qquad (2)$$

Where
V_2 = velocity of the rebounding piston
x_2 = the rebound of the spring

Therefore:

$$\frac{x_2}{x_1} = \frac{V_2}{V_1} \quad (3)$$

The rebound value or R$_h$ is a ratio of the initial stretch of the spring x$_1$ and the rebounded stretch x$_2$:

$$R_h = \frac{x_2}{x_1} * 100 \quad (4)$$

When the hammer is at any other angle than horizontal, the x$_2$ measured is actually x$_{2\Theta}$ and needs to be converted to find the actual value of R$_h$. This changes the above relationships in equation 1 and 2 to:

$$0.5kx_1^2 + MGx_1\cos(90-\theta) = 0.5MV_{1(\theta)}^2 \quad (5)$$

And:

$$0.5kx_{2(\theta)}^2 + MGx_{2(\theta)}\cos(90-\theta) = 0.5MV_{2(\theta)}^2 \quad (6)$$

Basu and Aydin (2004) have values for the LR and ND Proceq hammers so this equation can be solved for V$_{2\Theta}$ as can be seen in Table B2.

Table B2: Constants for LD and ND Proceq hammers from Basu and Aydin (2004)

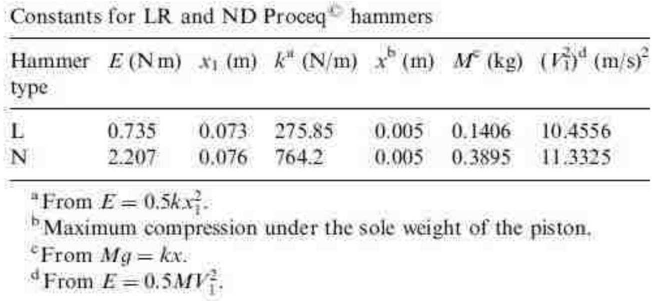

Constants for LR and ND Proceq© hammers

Hammer type	E (N m)	x_1 (m)	k[a] (N/m)	x[b] (m)	M[c] (kg)	(V_1^2)[d] (m/s)^2
L	0.735	0.073	275.85	0.005	0.1406	10.4556
N	2.207	0.076	764.2	0.005	0.3895	11.3325

[a] From $E = 0.5kx_1^2$.
[b] Maximum compression under the sole weight of the piston.
[c] From $Mg = kx$.
[d] From $E = 0.5MV_1^2$.

Using $V_{2(\theta)}^2$, V_2^2 can be solved for:

$$V_2^2 = \frac{V_{2(\theta)}^2(0.5kx_1^2)}{0.5kx_1^2 + Mgx_1(90-\theta)} \quad (7)$$

From this relationship, equation 4 is used to find the corrected R$_h$.

$$R_h = \sqrt{\frac{V_2^2}{V_1^2}} * 100 \quad (8)$$

The hammer used in these samplings was the proceq N hammer. The ND version of this differs from the N by the way that it records the data. The N is an analog system that needs to be recorded manually and the ND has a digital recording system. It is assumed that the values given by Basu and Aydin are the same for both instruments. Table B3 is the results of the angle correction.

Table B3: Results of angle correction

Formation	Angle	Measured Rh	Corrected Rh
Sandstone	45	43.0	38.4
Sandstone	45	39.1	34.1
Sandstone	-30	45.8	41.7
Chickaloon Carbonaceous Siltstone	20	24.5	17.9
Chicaloon Formation Mudstone	30	28.0	31.3
Healy Schist #1	10	60.2	62.2
Healy Schist #2	10	63.3	65.2
Healy Schist #3	10	67.3	69.0
Mafic Intrusive (Thm)	45	60.3	57.2

Calculation of Unconfined Strength

For the purpose of calculating the strength of the rocks, the samples were grouped into five types. The Sandstone and Healy Schist corrected Schmidt values were averaged over the three samples each.

To determine the best relationship, a literature review as conducted. Several papers, including Vellone (2007) compared multiple empirical relationships related to the R_h value. Table B4 is an extract from Vellone (2007) showing seven relationships and how many and what type of units were examined. Of these seven, Vellone (2007) commented that Singh (1983), O'Rourke (1989) and Sachpazis (1990) provided reasonable results for the correlation between Rh and UCS. Torabi (2011) also compared different relations, including Singh, O'Rourke and Sachpazis. He argued that each type of rock should be looked at separately, and studied coal faces and derived an equation using the data gathered.

Table B4: Empirical relations of Schmit Hammer to UCS (Vellone 2007)

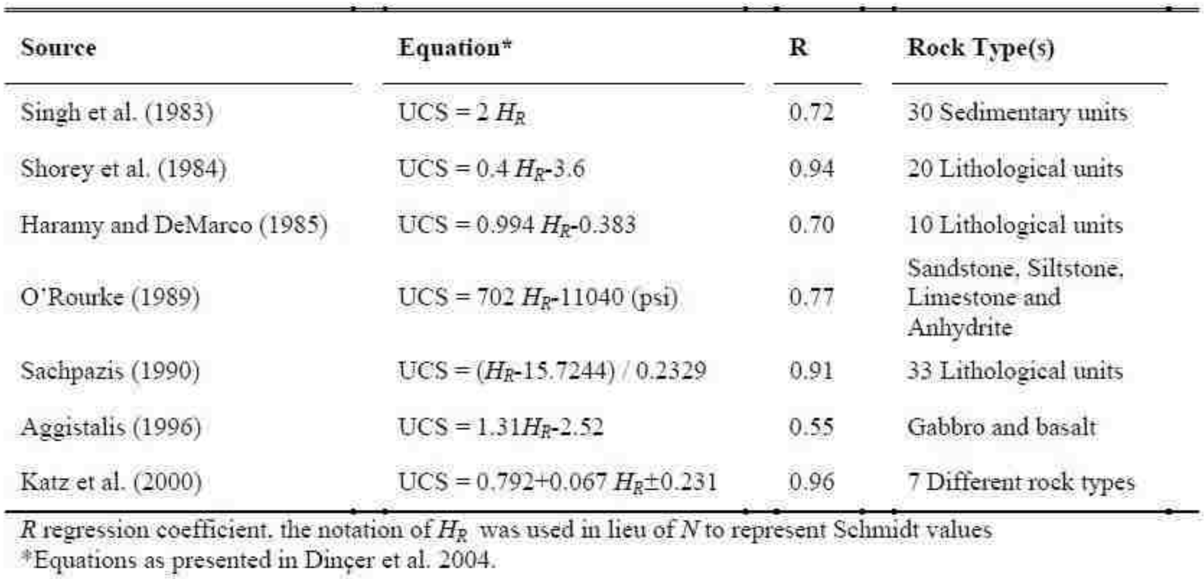

Source	Equation*	R	Rock Type(s)
Singh et al. (1983)	UCS = 2 H_R	0.72	30 Sedimentary units
Shorey et al. (1984)	UCS = 0.4 H_R-3.6	0.94	20 Lithological units
Haramy and DeMarco (1985)	UCS = 0.994 H_R-0.383	0.70	10 Lithological units
O'Rourke (1989)	UCS = 702 H_R-11040 (psi)	0.77	Sandstone, Siltstone, Limestone and Anhydrite
Sachpazis (1990)	UCS = (H_R-15.7244) / 0.2329	0.91	33 Lithological units
Aggistalis (1996)	UCS = 1.31H_R-2.52	0.55	Gabbro and basalt
Katz et al. (2000)	UCS = 0.792+0.067 H_R±0.231	0.96	7 Different rock types

R regression coefficient, the notation of H_R was used in lieu of *N* to represent Schmidt values
*Equations as presented in Dinçer et al. 2004.

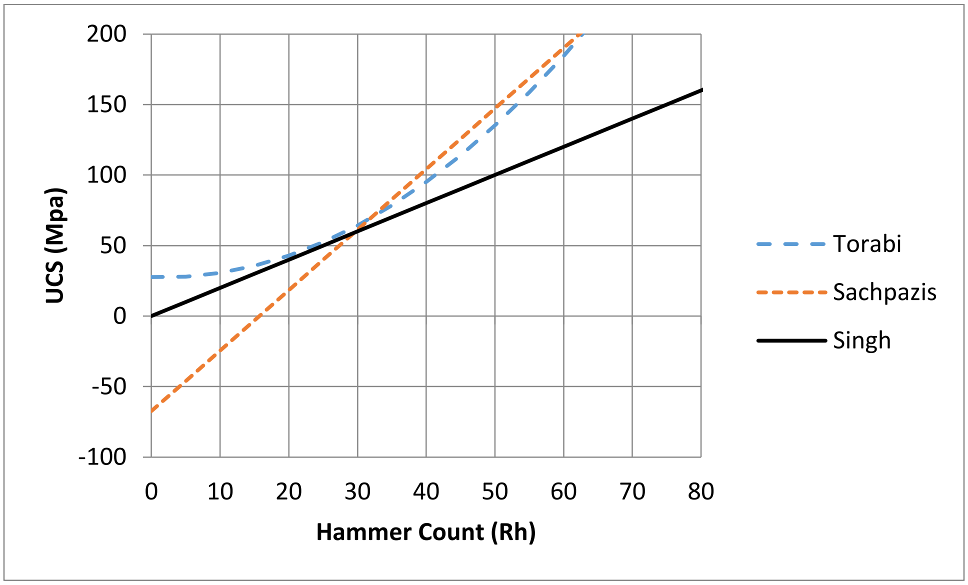

Figure B3: Graphed equations for Torabi et.al. (2011), Sachpazis (1990) and Singh (1983) empirical relations

Using the data from the Schmidt Hammer tests, a comparison was made between Torabi et.al. (2011), Sachpazis (1990) and Singh (1983) to see the differences in the data (See Figure B3). Table B5 shows the results for the five samples that were in the test areas. Sachpazis under estimates lower values of Rh while Singh underestimates larger Rh values although all values are close to each other in the 20-40 count range.

Table B5: Corrected Rh values with strengths from three empirical formulas

Formation	Corrected Rh	Sachpazis (Mpa)	Torabi (Mpa)	Singh (Mpa)
Sandstone	38.1	96.0	88.4	76.2
Chickaloon Carbonaceous Siltstone	17.9	9.5	39.5	35.9
Chicaloon Formation Mudstone	31.3	66.8	67.7	62.6
Healy Schist	65.4	213.4	215.3	130.9
Mafic Intrusion (Thm)	57.2	178.0	169.6	114.3

Field Data for Schmidt Hammer

	Mile Mark	Rock Name	Angle	Schmidt Hammer Readings																					
GG	239.5-6	Healy Schist #1	10	64	64	58	57	64	65	60	54	61	58	55	61	60	60	67	55	60					
GG	239.5-6	Healy Schist #2	10	66	66	61	65	55	65	55	70	60	60	68	64	55	66	67	70						
GG	239.5-8	Healy Schist #3	10	69	69	68	68	69	68	67	70	65	65	67	69	69	66	64	64	66	65	71			
GG	239.5-4	Mafic Intrusion	45	58	62	64	48	50	62	50	64	66	62	62	64	60	63	62	64	60	64	60	60		
LL	85b	Sandstone #1	45	45	40	41	38	40	48	36	44	48	49	49	34	39	45	46	46	49	42	40	40	41	45
LL	86.9ab	Sandstone #1	45	38	38	38	35	45	42	36	30	44	45	39	35	38	40	40	38	38	38	44	40		
LL	87.1	Sandstone #1	-30	49	49	48	53	48	49	54	50	32	35	41	39	41	45	47	51	35	55	47	47		
LL	86.2	Chickaloon Siltstone	20	14	14	22	17	22	28	22	28	32	18	24	27	21	31	31	30	29	24	32			
LL	86.9e	Chickaloon Mudstone	30	20	32	32	27	26	34	30	31	33	26	27	26	24	18	32	30						

Appendix C: First iteration of RDA remote processing

The first iteration of remotely classifying the RDA was done by the following process. It was found that this method was too time consuming.

Process using GIS

Table C1 shows the attributes that were used in the processes along with how they were derived. Figure B1 is a visualization of this in Google Earth from Parks highway MP 239.5.

A DEM file from the lidar and other information such as weathering, ability to see where stabilization and protective measures are located are needed to complete this process.

1. Make a fishnet in ArcGIS (Data Management Tools\Feature Class\Create Fishnet)
    i. This can be various sizes depending on what scale you want the final product to be
    ii. Use the option to create polygons with labels
2. Create aspect raster from DEM (Spatial Analyst Tools\Surface\Aspect)
3. With labels layer, extract multi values to points (Spatial Analyst Tools\Extraction\Extract Multi Values to Points)
    i. Use the aspect and the DEM file to get aspect and elevation.
    ii. This will only give the amount at the center of the polygon. Another way is to use zonal statistics for each layer to extract the mean\max\min values.
4. Gather attributes in form that can be easily analyzed (See Table C1 for attributes and how to measure)
    i. The easiest forms: Google earth files and shapefiles
    ii. This might require the building of a shapefile or kmz of the needed information
5. Import kmz (a compressed keyhole markup language file used in Google Earth) files into ArcMap
6. Select by location each value
    i. Add a column in the fishnet file for each attribute.
    ii. Give each polygon the attribute rating
7. Identify traces
    i. Find their length
    ii. Join them by location and give each polygon on the fishnet the value of the traces
8. Join the point attributes to the polygon attributes
9. Export data
10. Take the data into excel and calculate RDA

    i. For this an excel spreadsheet was set up with the formulas and calculated the RDA rating for each polygon
11. Save the ID of the polygon and the RDA rating into a .csv file
12. Open .csv file in ArcMap and join to the polygon file
13. Display RDA values
    i. This file will be a flat file, use ArcScene and use the DEM as a base file to better visualize
    ii. Export as KMZ file into Google Earth

Table C1: Final RDA Factors used for this project and how they were determined (Nicholson 2004)

Attribute	Form
Fracture Spacing	Manually traced discontinuities and imported into ArcMap
Fracture Aperture	Gave traced discontinuities a relative scale (This was done before the second field investigation)
Rock Compressive Strength	Assumed to be the same (in the next iteration field measurements will be used)
Rock Material Weathering Grade	Created a kmz file with areas of relative weathering
Altitude	Used DEM elevation
Aspect	Derived an aspect map from DEM
Groundwater and Surface Runoff	Assumed to be the same for all cases attempts made through GIS and remote sensing.
Static Stresses	Assumed to be the same for all cases
Dynamic Stresses	Assumed to be the same for all cases
Excavation History	Assumed to be the same for all cases
Stabilization and Protective Measures	Created a kmz file with stabilization and protective features
Vegetation Cover	Created a kmz file outlining the vegetation on the slopes
Slope Geometry	Measured slope
Rock Mass Structure	Calculated from other attribute measurements
Time Since Excavation	Assumed to be the same for all cases attempts made to find original records as to construction, but could not be located
Direct disturbance	Assumed to be the same for all cases

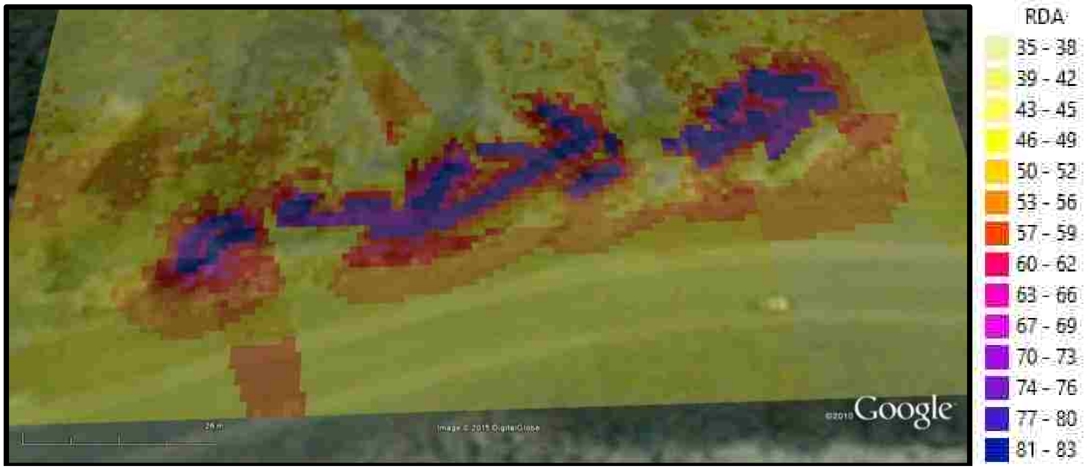

Figure C1: RDA rating on section in Parks Highway near MP 239.5 visualized in Google Earth.

Results of the RDA

Figure C1 represents a three meter by three meter grid of the RDA in Parks Highway area. The areas of purple and blue represent the slope areas with a higher likelihood of failure and coincide with mapped discontinuities. Since the discontinuities were hand traced, if a discontinuity were missed or skipped, the results would have been skewed.

Appendix D: Example RDA point clouds:

Glenn Highway milepost 86.9

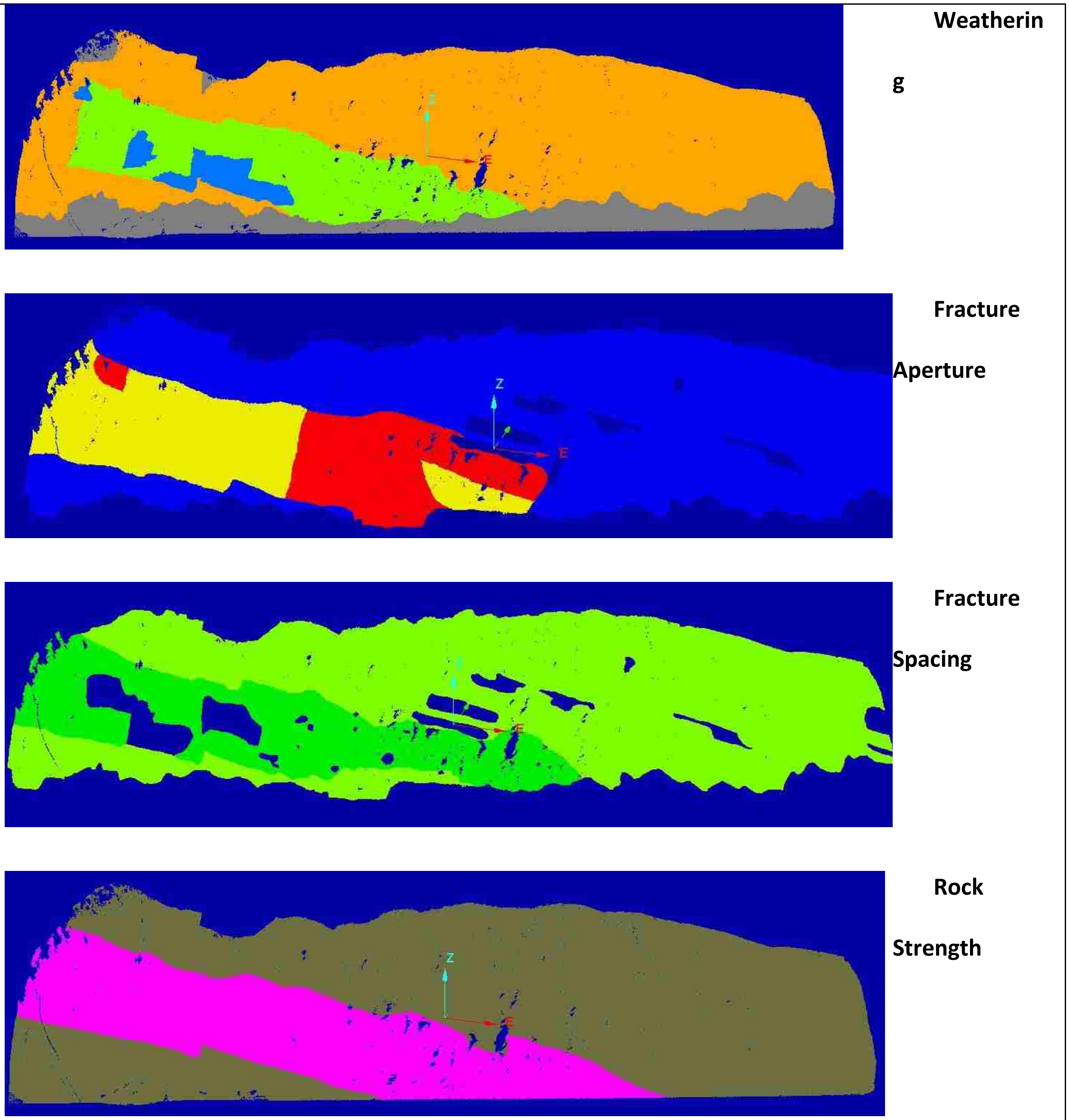

Figure D1: Glenn Highway milepost 86.9 RDA classifications. Colors correspond to Table C2.

Glenn Highway milepost 87

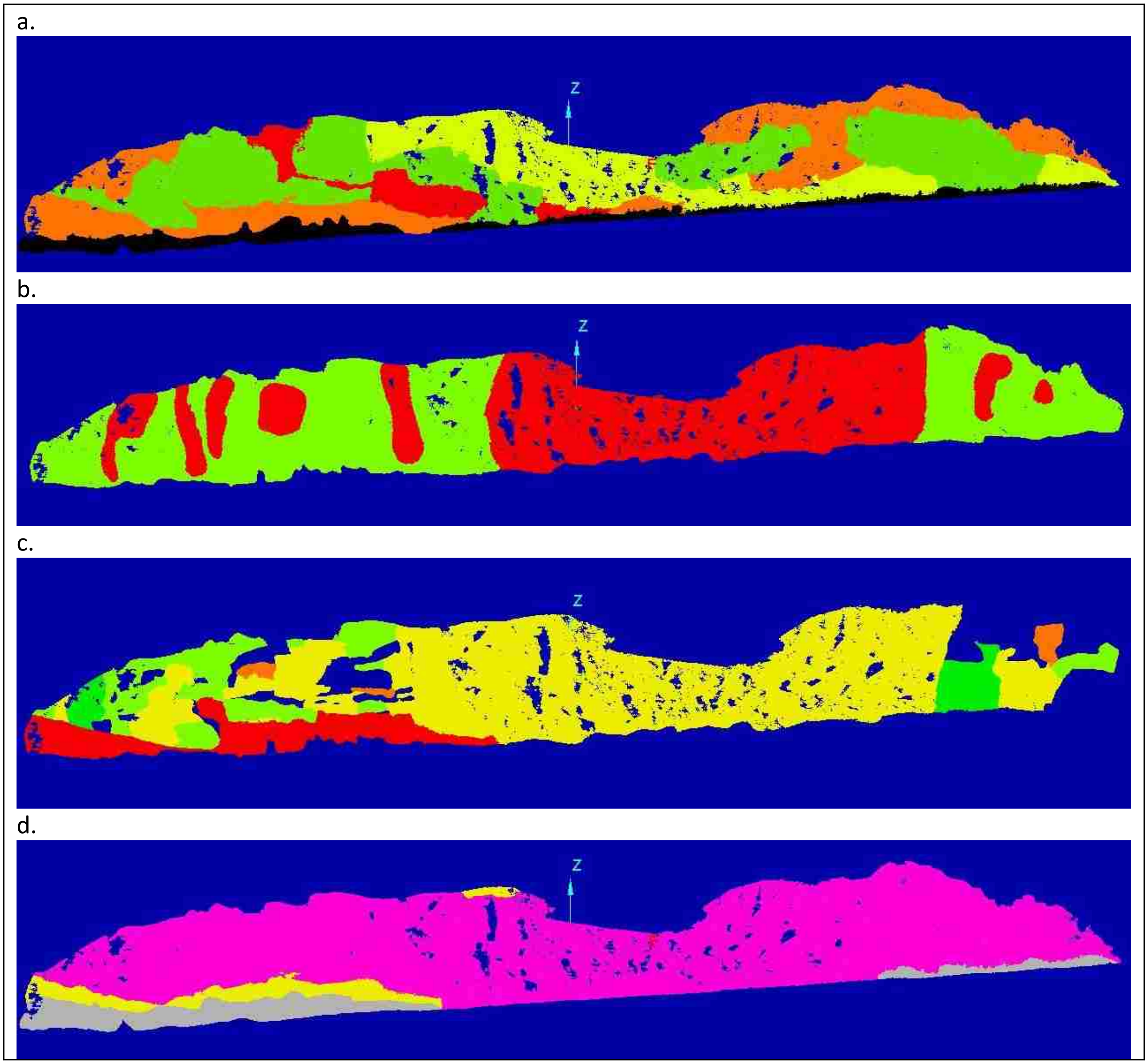

Figure D2: Glenn Highway milepost 87. a) weathering, b) fracture aperture, c) fracture spacing and d) rock strength. Colors correspond to Table C2.

Parks Highway milepost 239.5 south

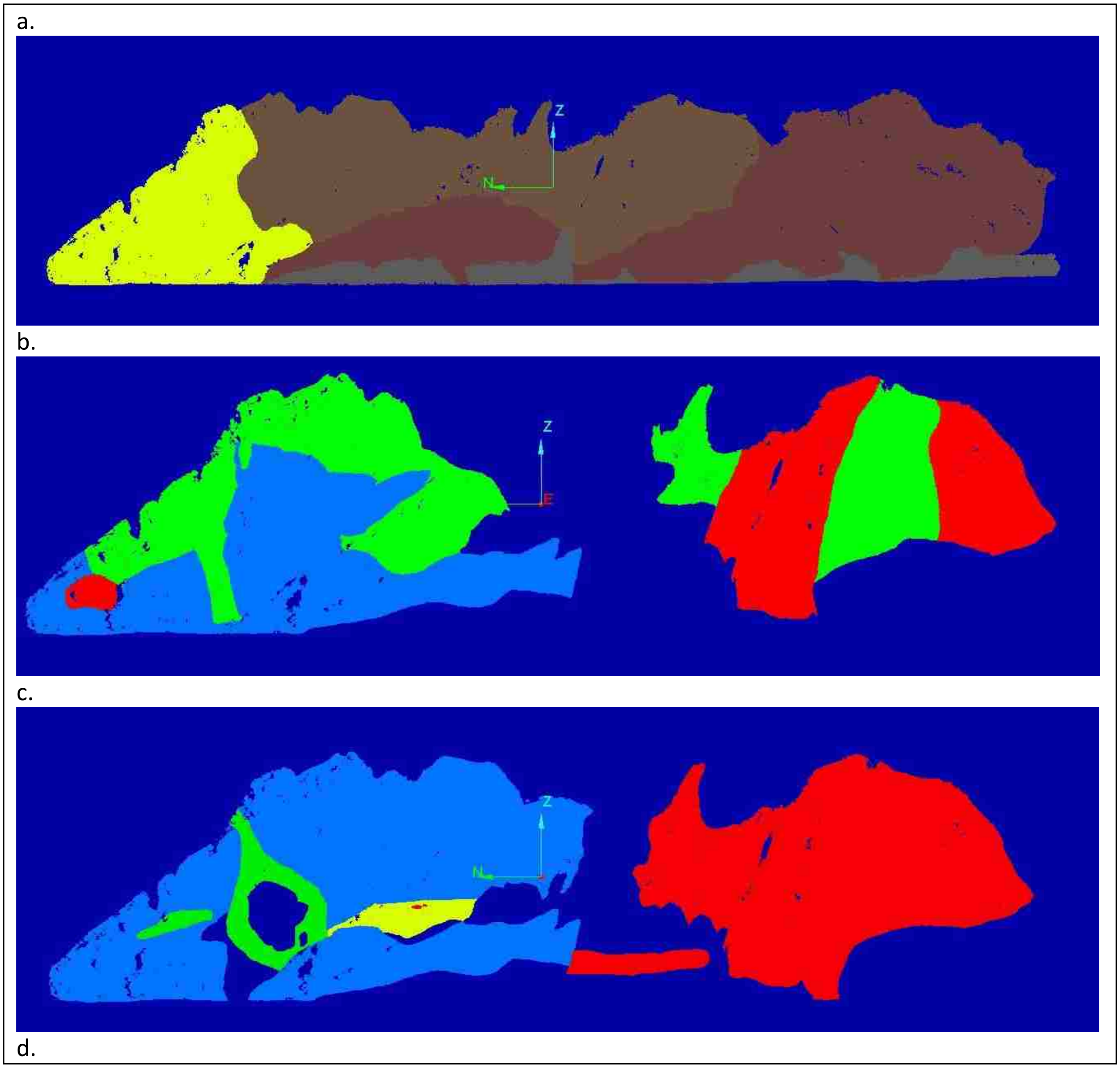

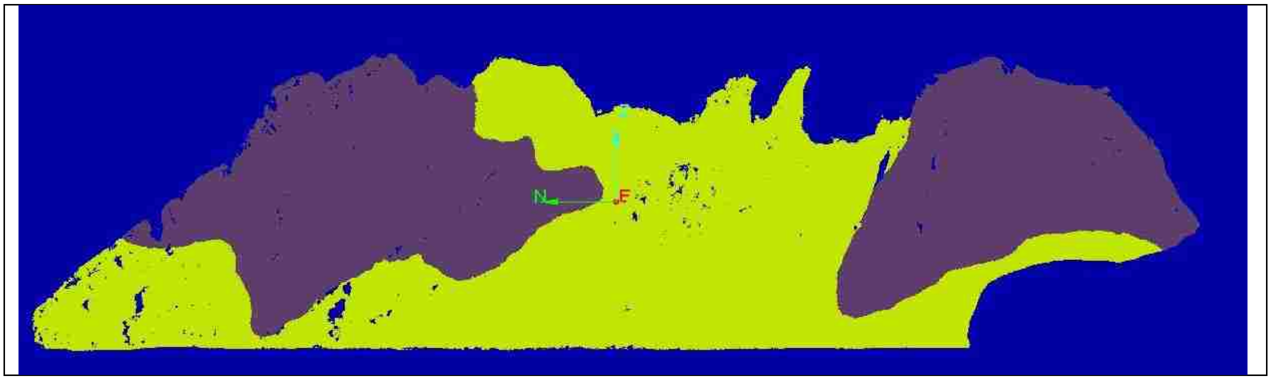

Figure D3: Parks Highway milepost 239.5 south. a) weathering, b) fracture aperture, c) fracture spacing and d) rock strength. Colors correspond to Table C2.

Parks Highway milepost 239.5 north

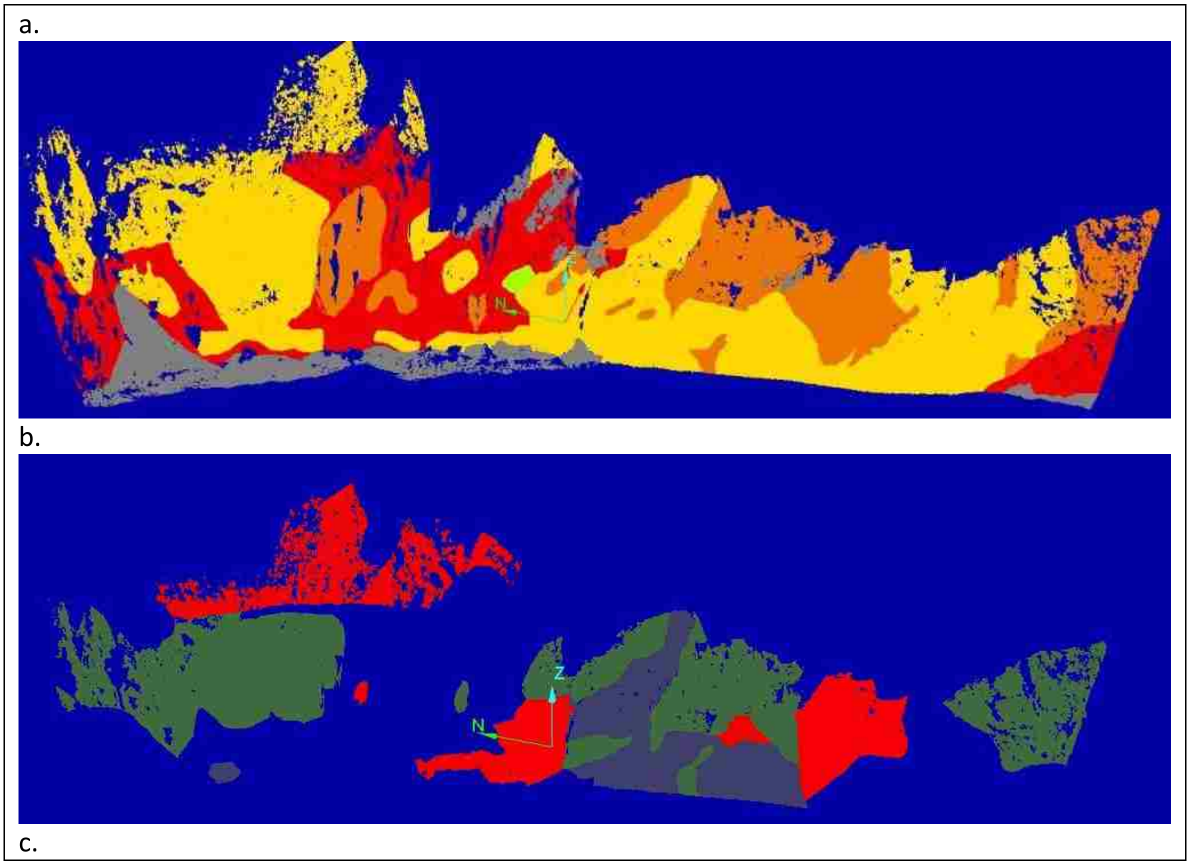

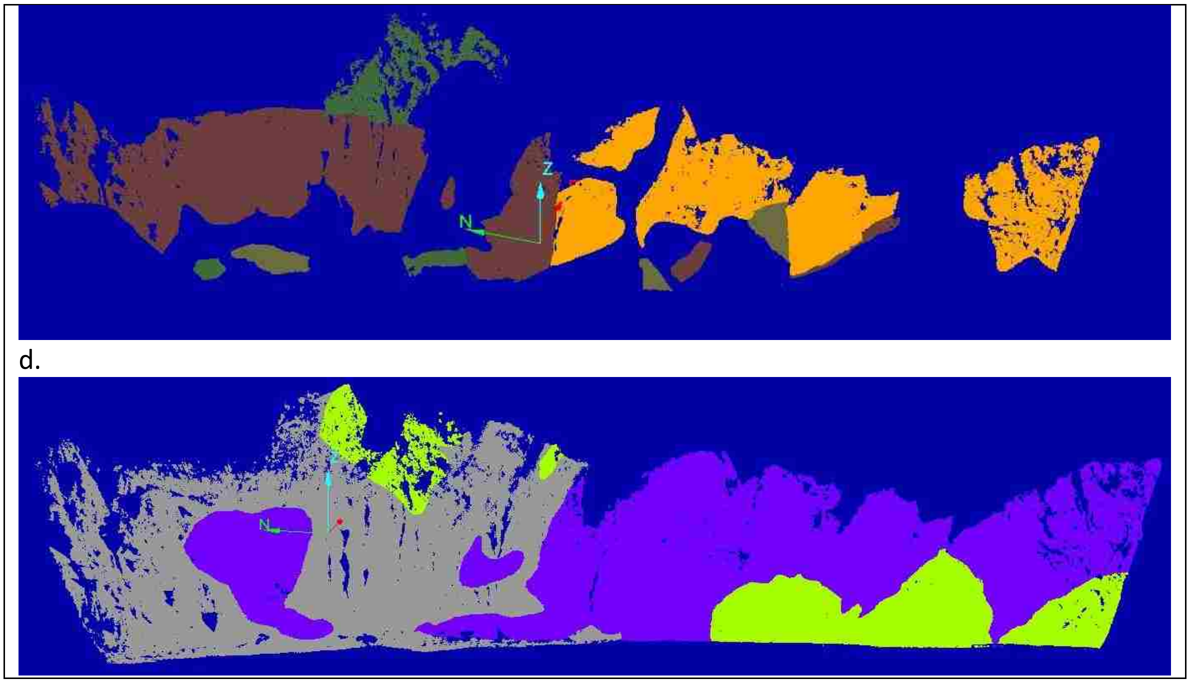

Figure D4: Parks Highway milepost 239.5 north. a) weathering, b) fracture aperture, c) fracture spacing and d) rock strength. Colors correspond to Table C2.

Appendix E: Difference between Computer and Hand calculated failure rates

The failure rate for the rock slope was determined by two methods. The first one was by the computer using the significant change parameters discussed in the section on lidar. The second was a manual method using photographs from two years, 2013 and 2014, which were examined for change. When a change was spotted, four screen captures were taken, the 2013 and 2014 photographs and the RAI classification for 2013 and the change detection located on the point cloud. The area of change was then identified on the RAI classification cloud using the change detection and photographs as reference and the points within the cloud were counted according to class. In all this method identified 18 failure areas, although more may be present but not identified due to angle of the photographs or size. The results of the two methods are shown in the table below.

Table E1: Comparison of computer and hand calculations for change detection

	Computer Calculations	**Hand Classification**
Class	**FR(%)**	**FR(%)**
Undefined	1.83	0.40
Talus	0.61	0.00
Intact	0.97	0.10
10 cm	3.03	0.18
20 cm	6.05	0.34
30 cm	9.25	0.71
<120	23.18	1.98
>120	50.67	1.97
Total	6.26	0.48

The total failure is an order of magnitude difference, although the failures for certain classes have a much wider gap. There are several factors that affect the failure rate in both the computer and hand classifications. For the computer, every change is picked up, even if it is vegetation changes or misalignment in the clouds. To account for this, a significant change threshold can be established, but this too has its drawbacks as smaller failures are likely to be missed. In the hand calculation, the areas need to be identified on the clouds, which is the most difficult part because the photographs are higher resolution then the RGB mapped onto the point clouds. General areas are normally easy to identify, but specific spots can pose a challenge. Because of this, many of the areas are approximately in the correct place and the cells counted may be greater than the actual cells with failure. For both of these methods, the failure rate is considered higher than actual therefore both methods are considered conservative.

Appendix F: RAI scored sites

All figures in this section are on the same scale as seen in figure F1.

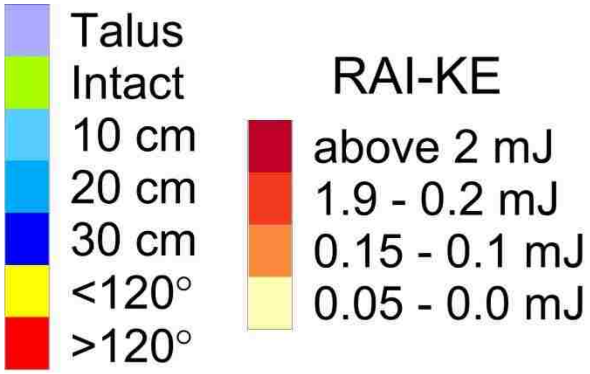

Figure F1: Key for RAI class and KE

Parks Highway Section 07D

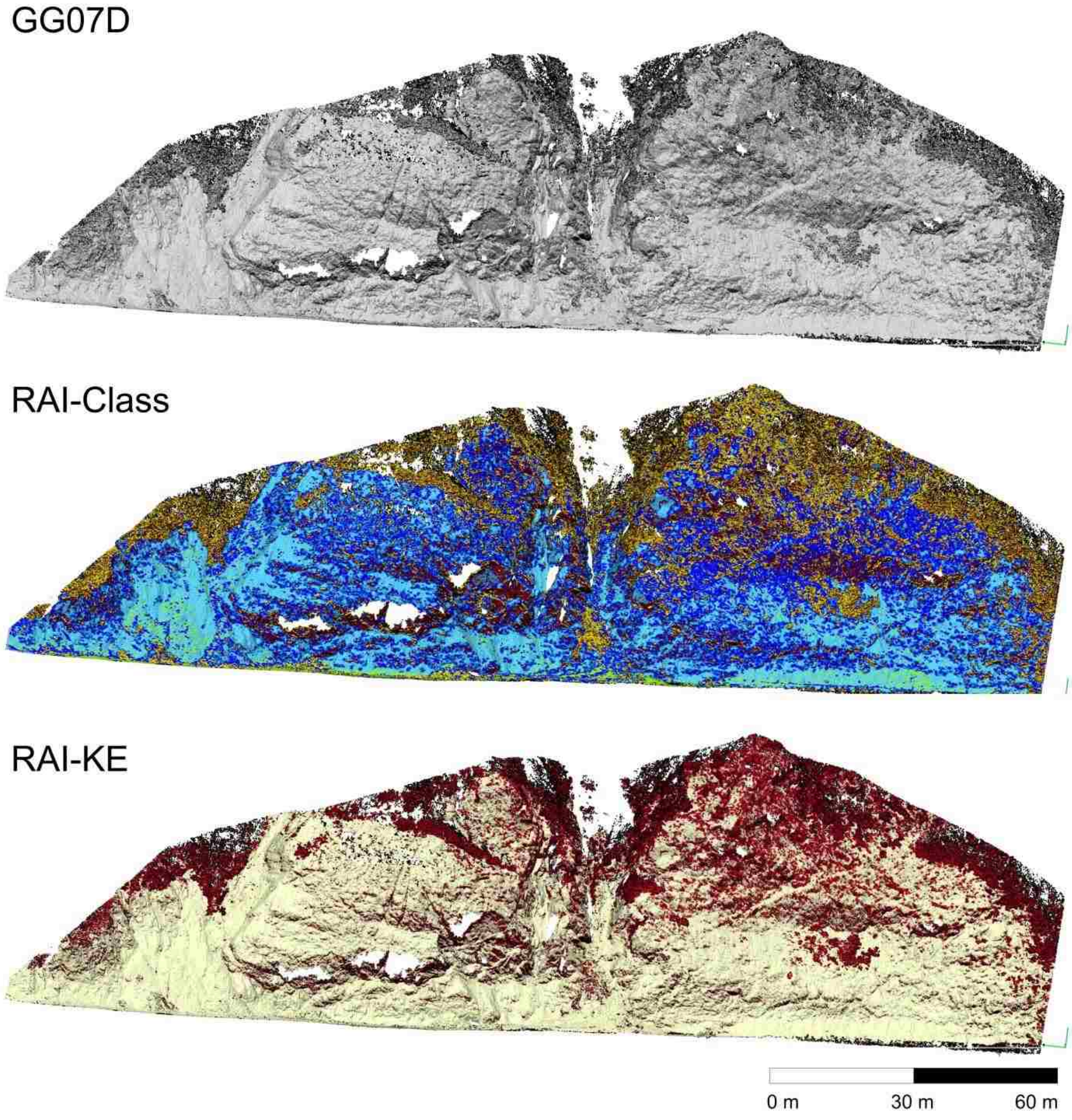

GG07D

RAI-Class

RAI-KE

Parks Highway Section 08C

GG08C

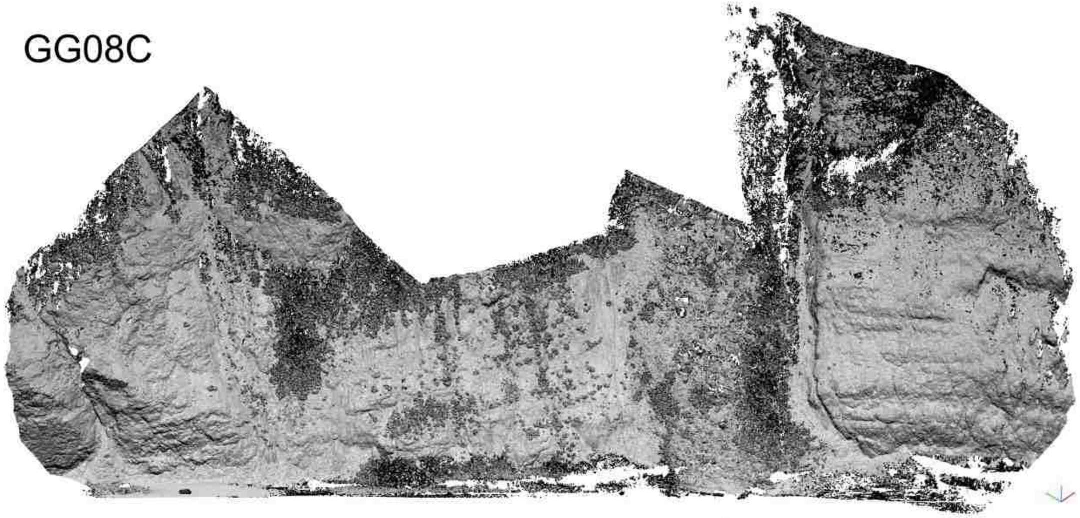

RAI-Class

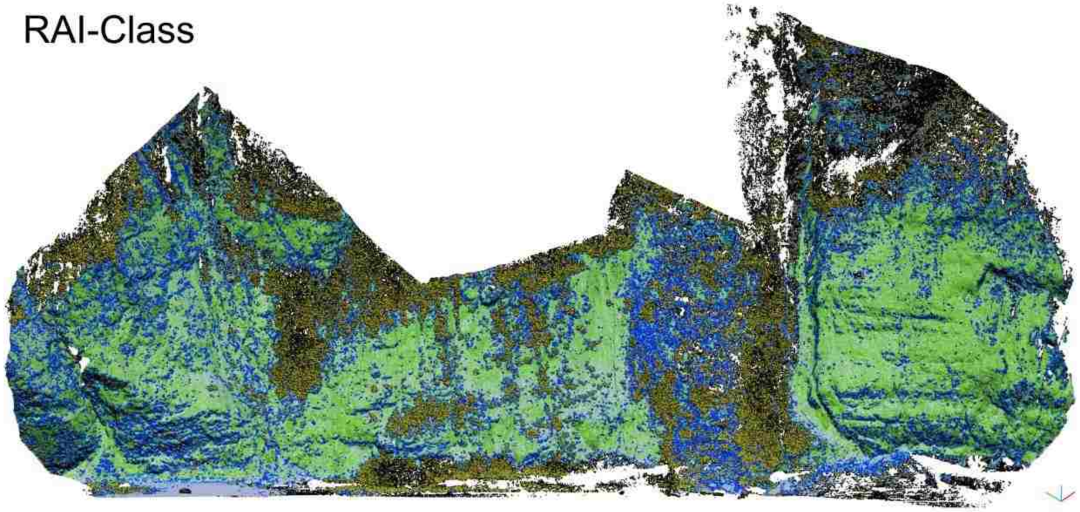

RAI-KE

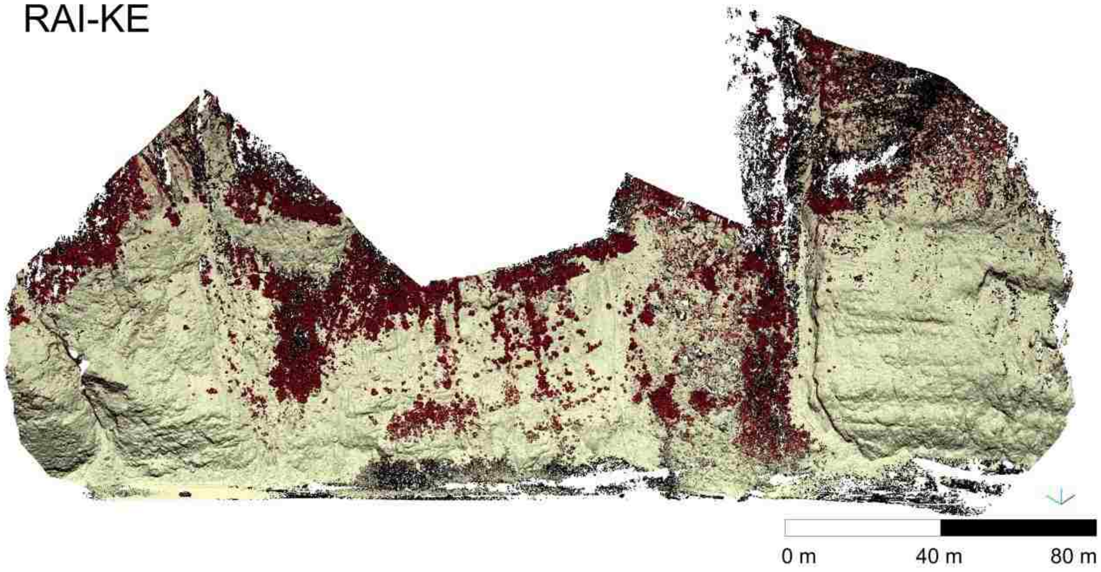

Parks Highway Section 10

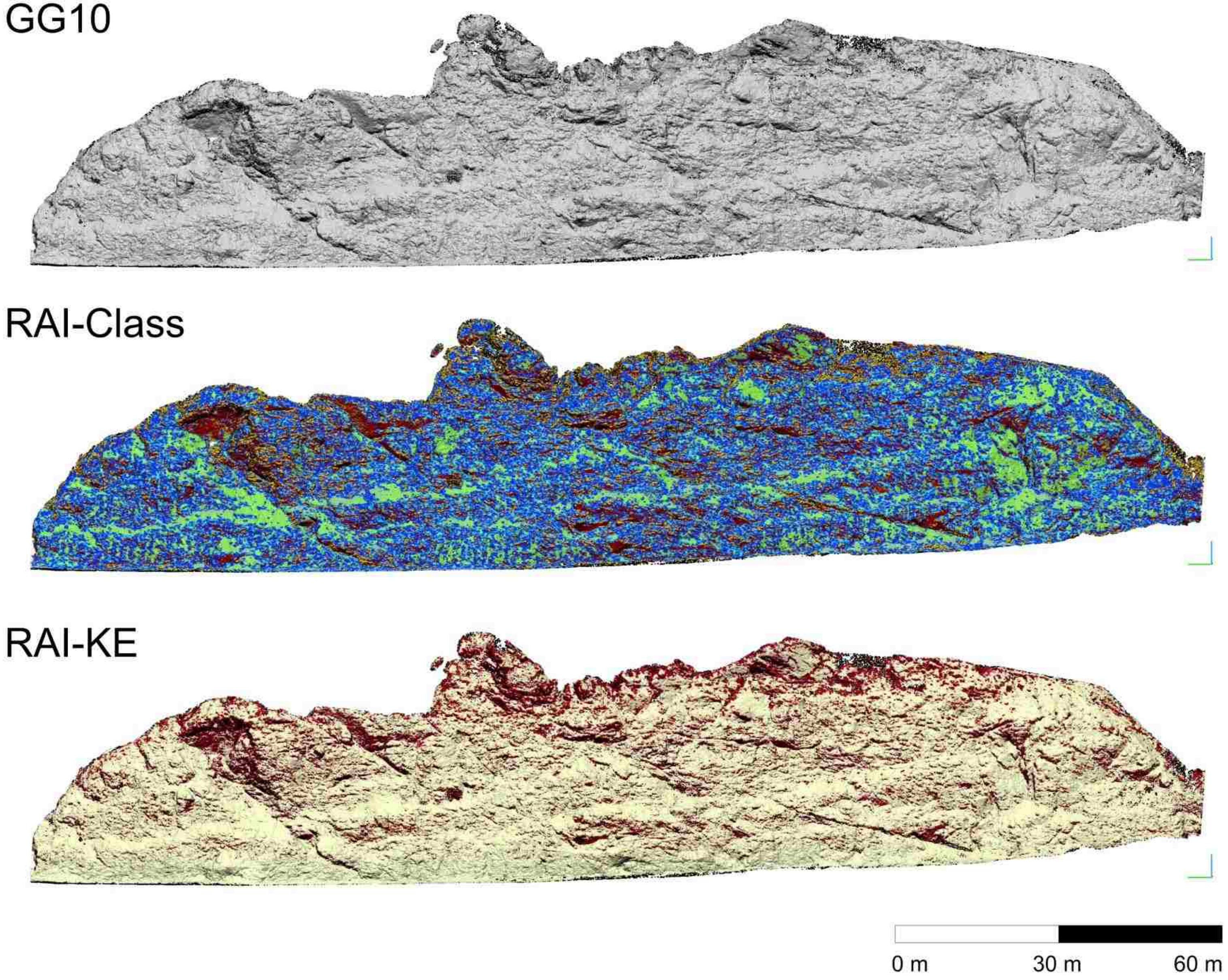

Glenn Highway Section 14 C

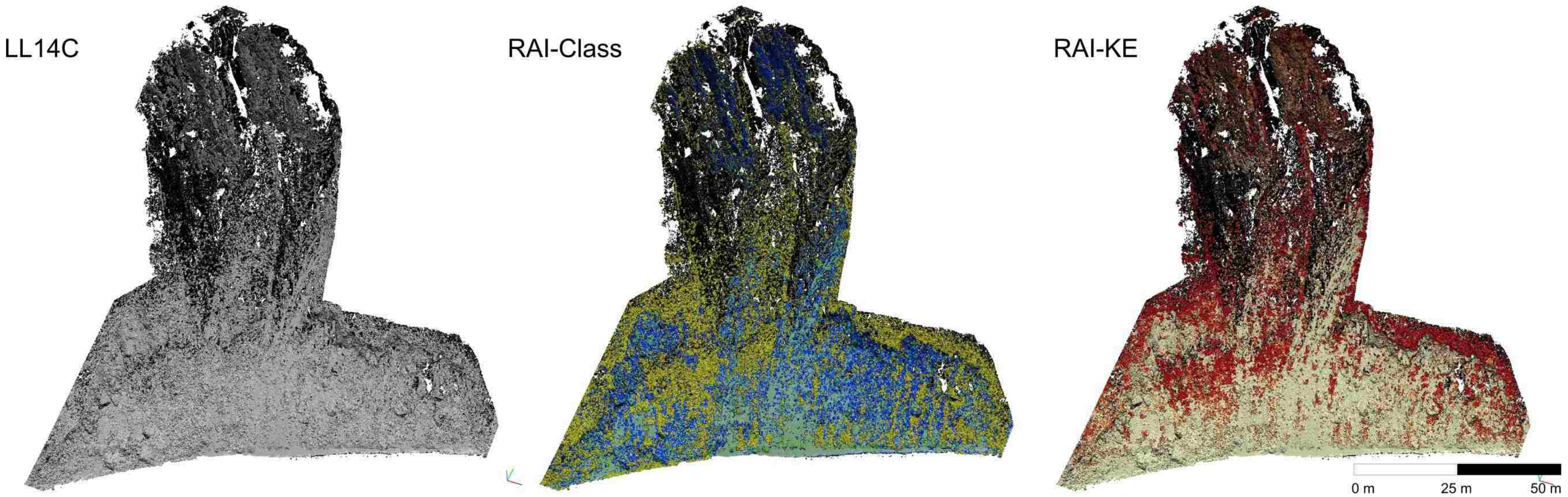

Glenn Highway Section 14 E

LL14E

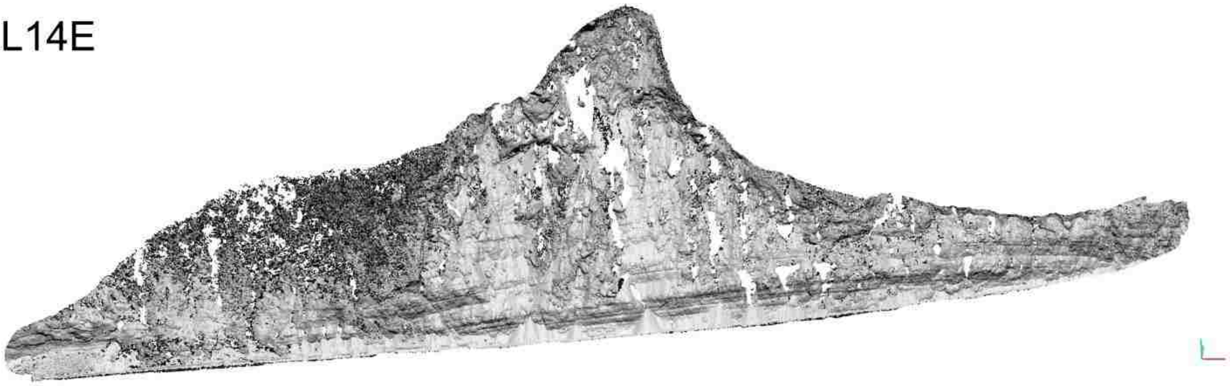

RAI-Class

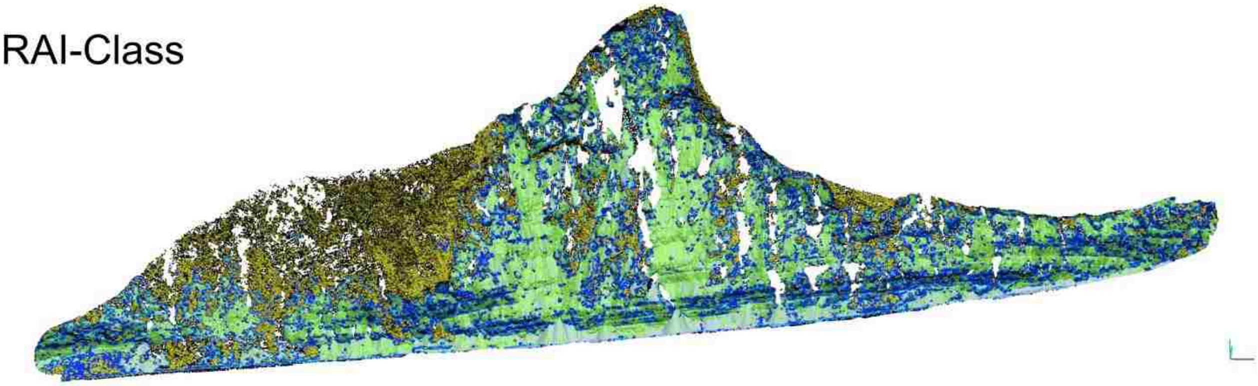

RAI-KE

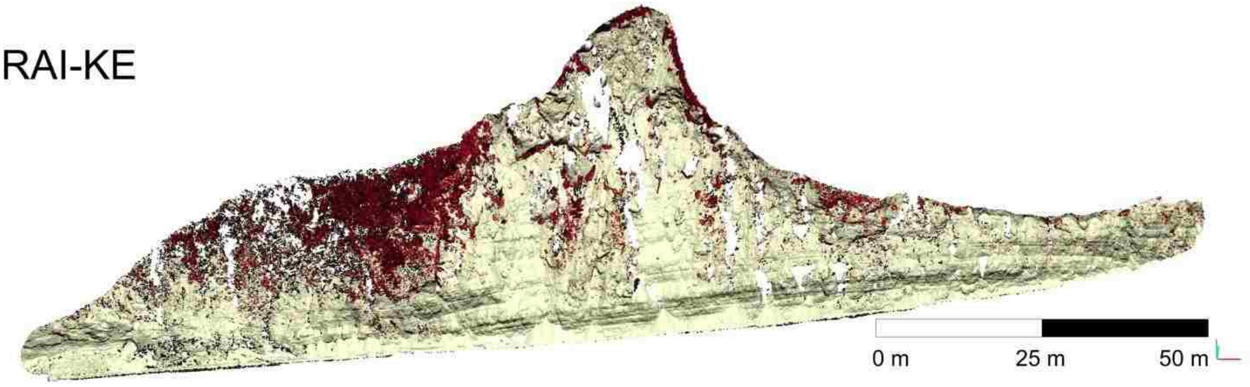

Glenn Highway Section 16A

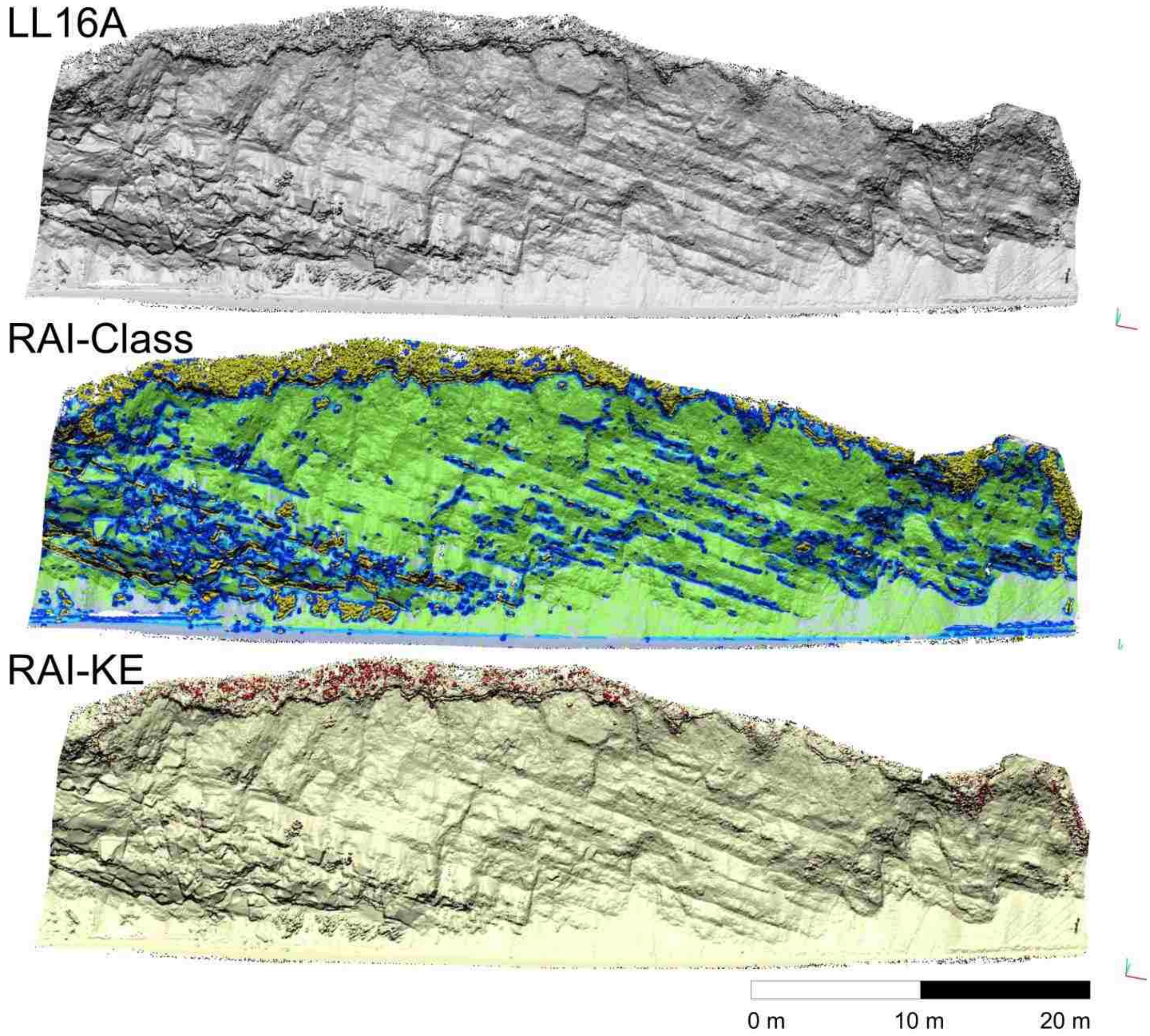

Glenn Highway Section LL 16B

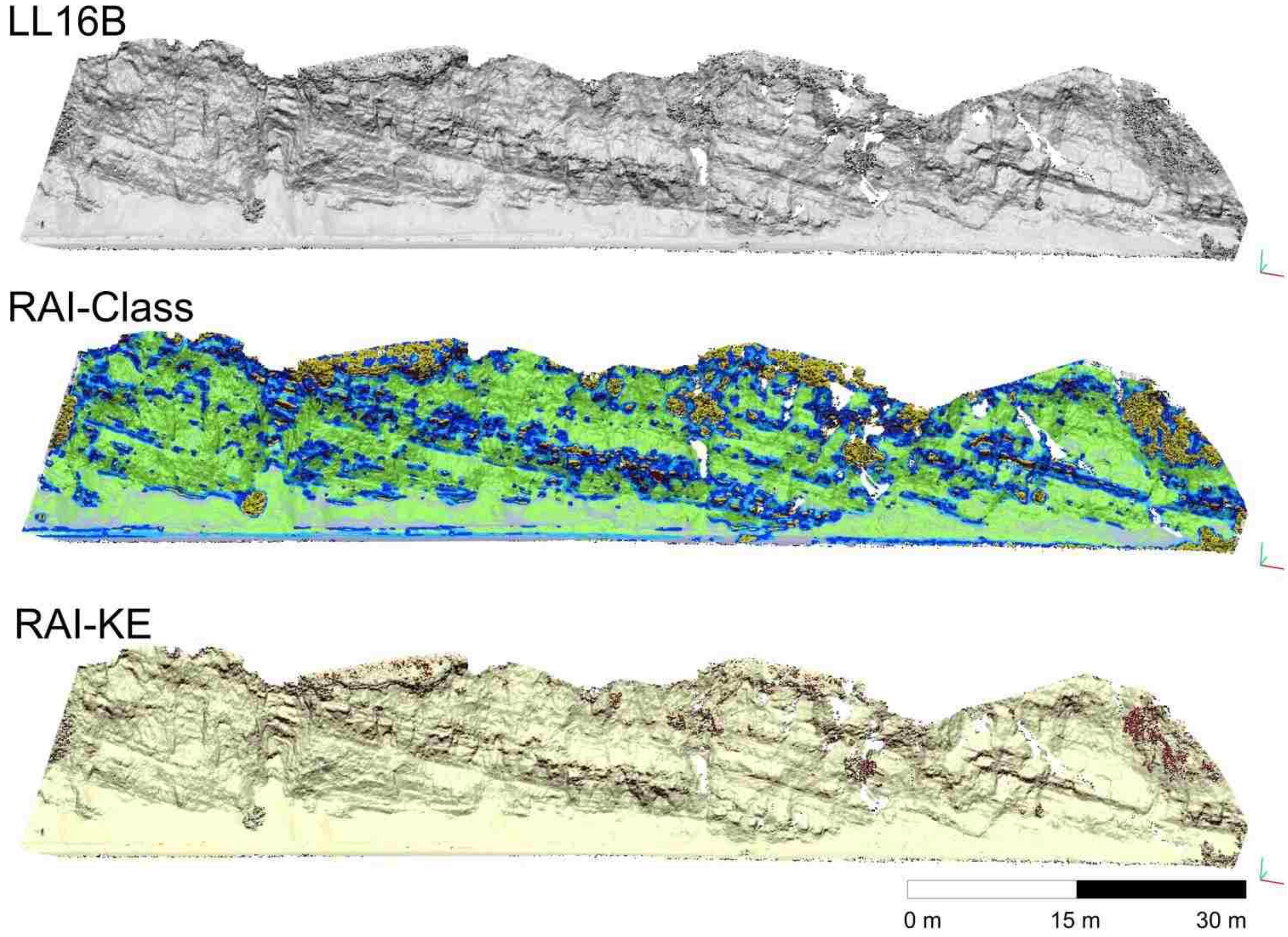

Glenn Highway Section 16D

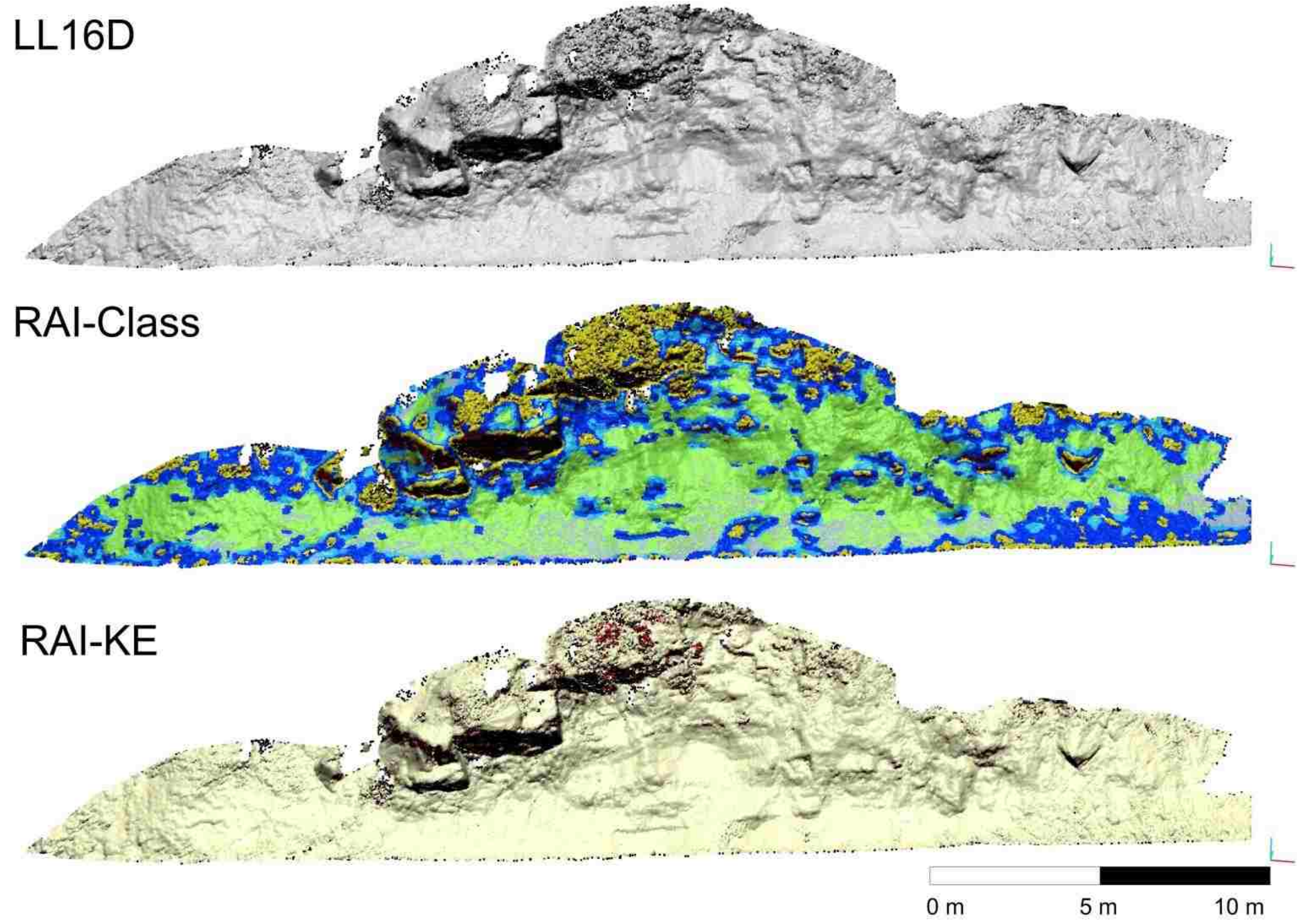

Appendix G: Magnitude Frequency relationship data

Individual sites showing the range of A and beta between the two sets of data.

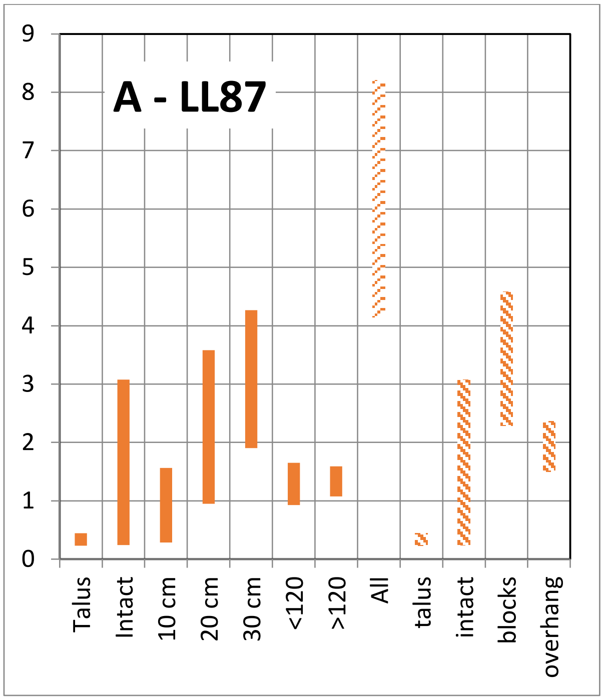

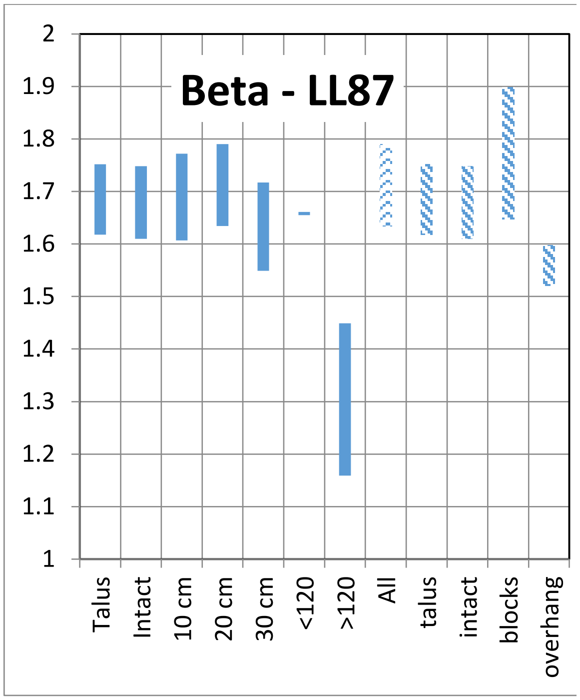

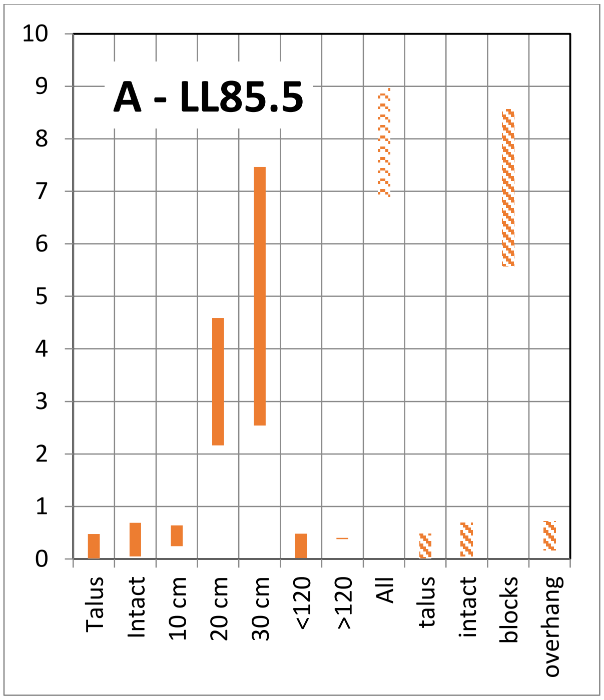

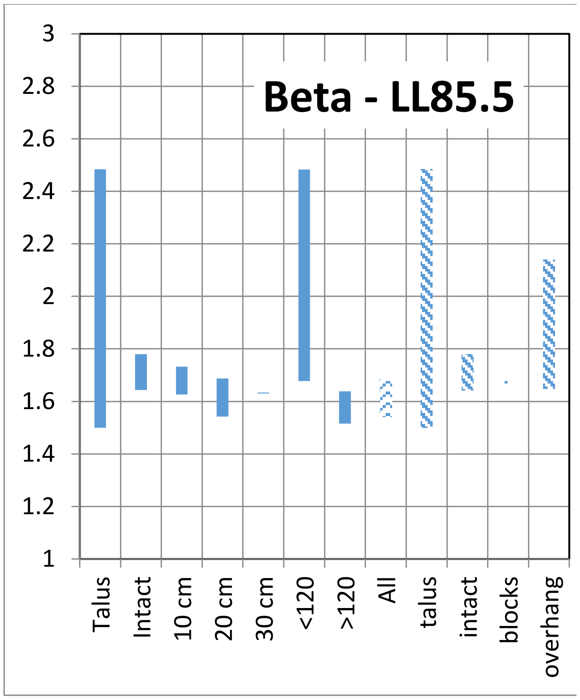

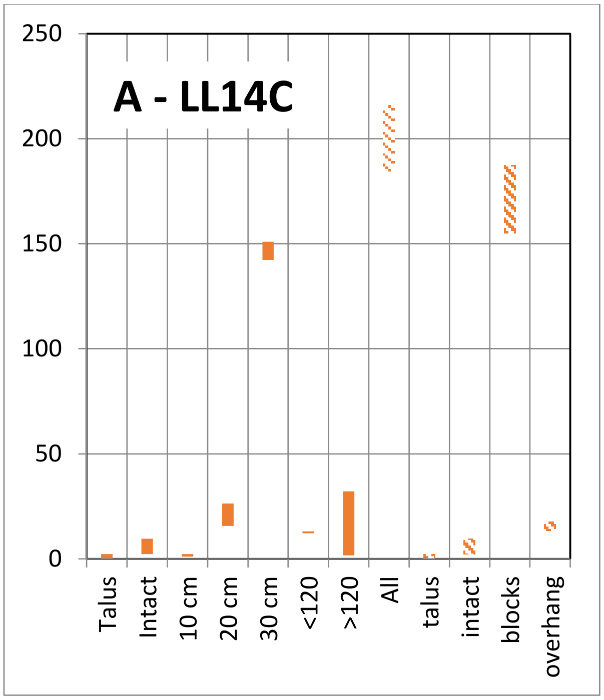
A - LL14C
250
200
150
100
50
0
Talus
Intact
10 cm
20 cm
30 cm
<120
>120
All
talus
intact
blocks
overhang

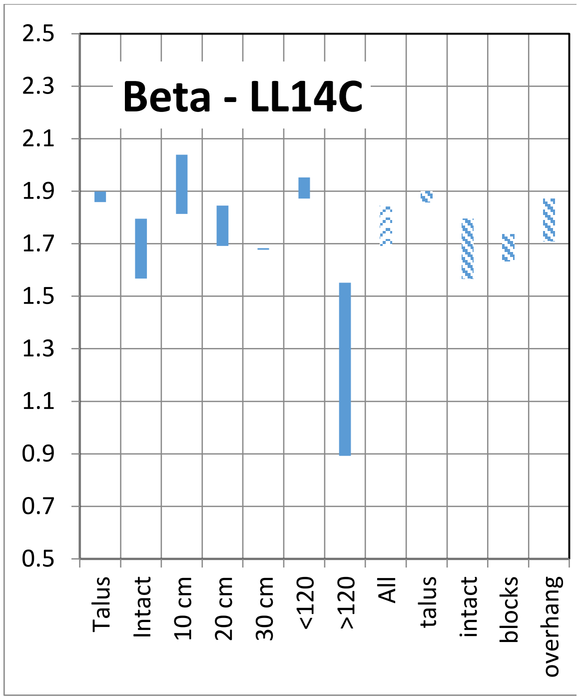
Beta - LL14C
2.5
2.3
2.1
1.9
1.7
1.5
1.3
1.1
0.9
0.7
0.5
Talus
Intact
10 cm
20 cm
30 cm
<120
>120
All
talus
intact
blocks
overhang

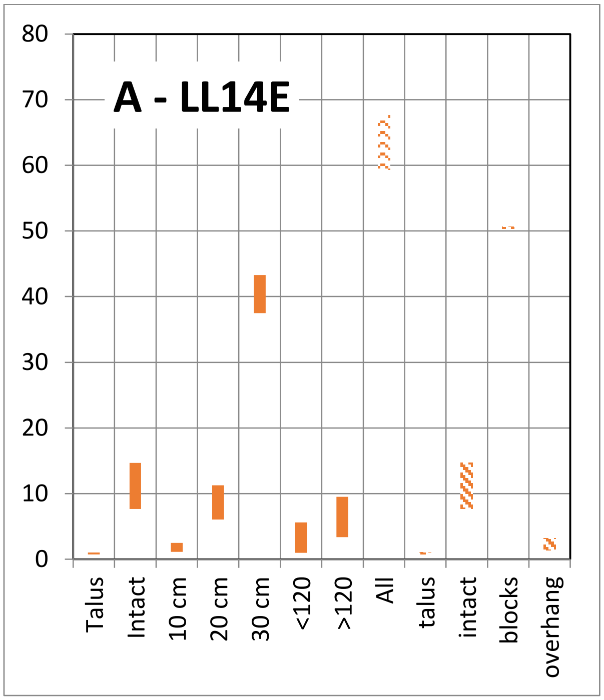
A - LL14E
80
70
60
50
40
30
20
10
0
Talus
Intact
10 cm
20 cm
30 cm
<120
>120
All
talus
intact
blocks
overhang

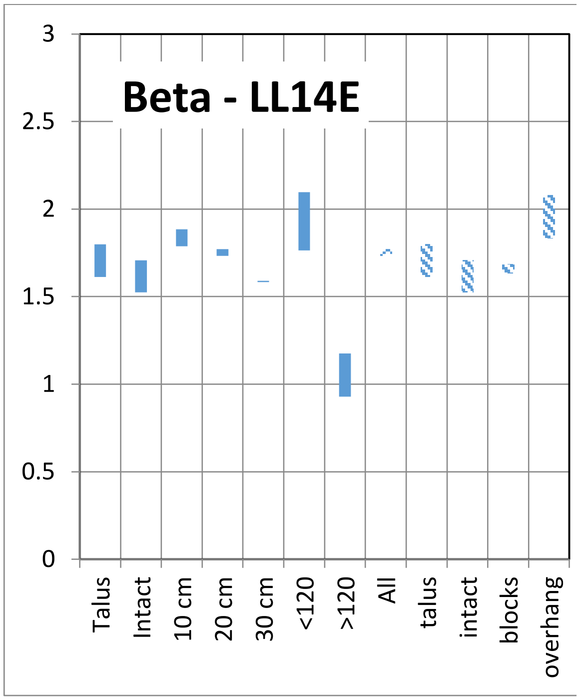
Beta - LL14E
3
2.5
2
1.5
1
0.5
0
Talus
Intact
10 cm
20 cm
30 cm
<120
>120
All
talus
intact
blocks
overhang

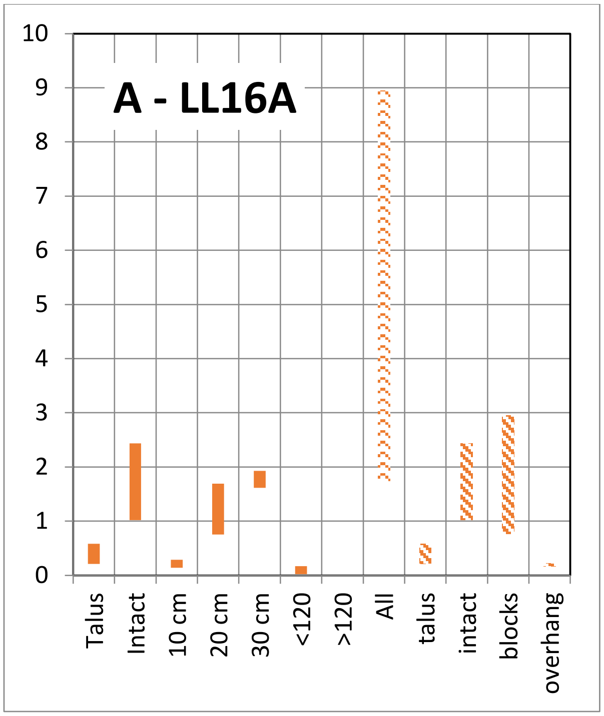
A - LL16A
10
9
8
7
6
5
4
3
2
1
0
Talus
Intact
10 cm
20 cm
30 cm
<120
>120
All
talus
intact
blocks
overhang

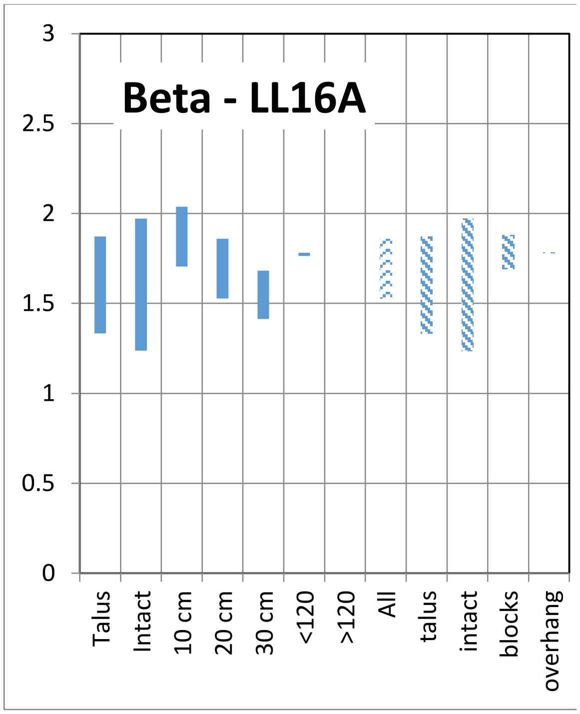
Beta - LL16A
3
2.5
2
1.5
1
0.5
0
Talus
Intact
10 cm
20 cm
30 cm
<120
>120
All
talus
intact
blocks
overhang

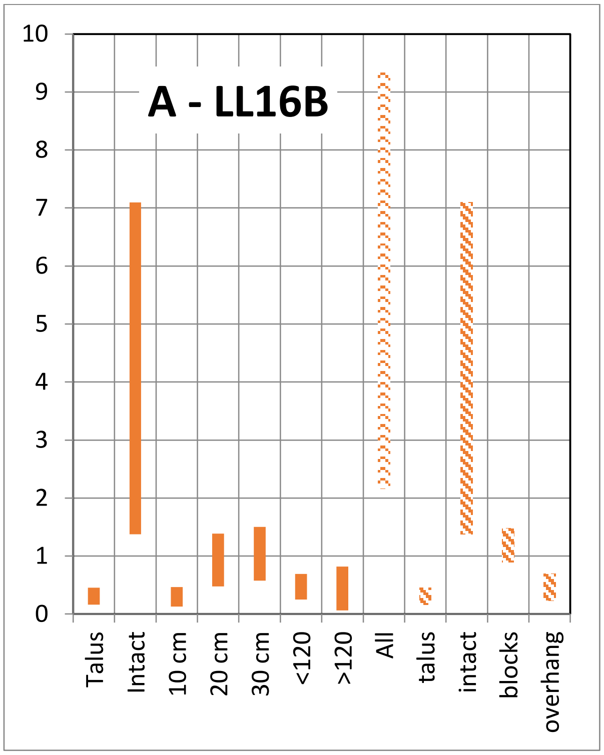
A - LL16B
10
9
8
7
6
5
4
3
2
1
0
Talus
Intact
10 cm
20 cm
30 cm
<120
>120
All
talus
intact
blocks
overhang

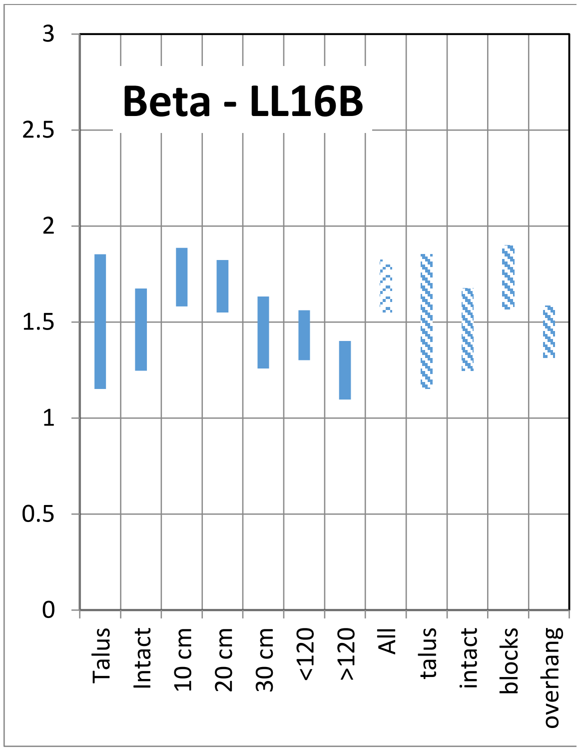
Beta - LL16B
3
2.5
2
1.5
1
0.5
0
Talus
Intact
10 cm
20 cm
30 cm
<120
>120
All
talus
intact
blocks
overhang

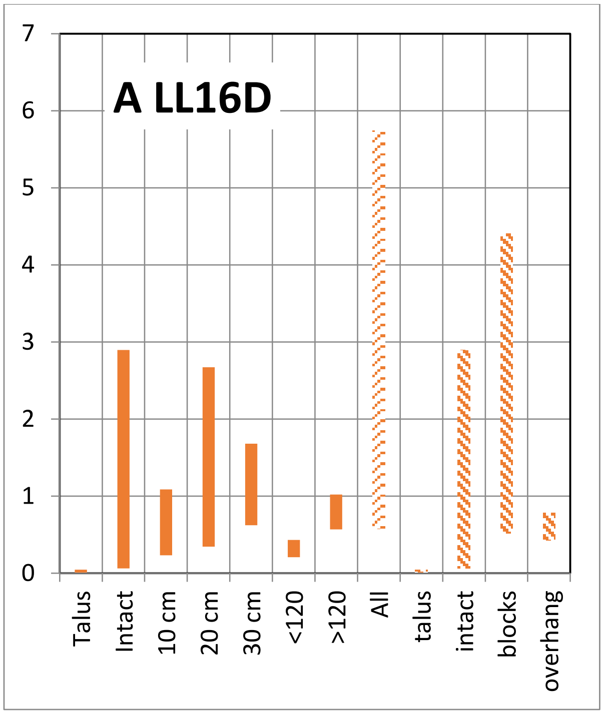
A LL16D
7
6
5
4
3
2
1
0
Talus
Intact
10 cm
20 cm
30 cm
<120
>120
All
talus
intact
blocks
overhang

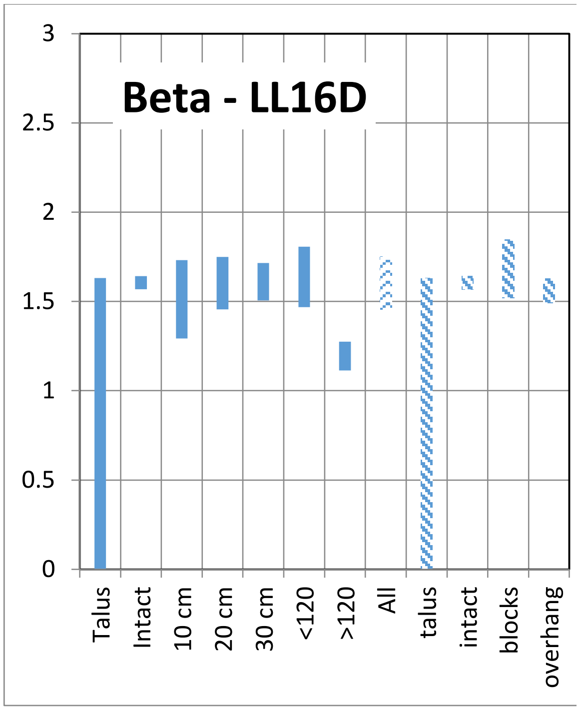
Beta - LL16D
3
2.5
2
1.5
1
0.5
0
Talus
Intact
10 cm
20 cm
30 cm
<120
>120
All
talus
intact
blocks
overhang

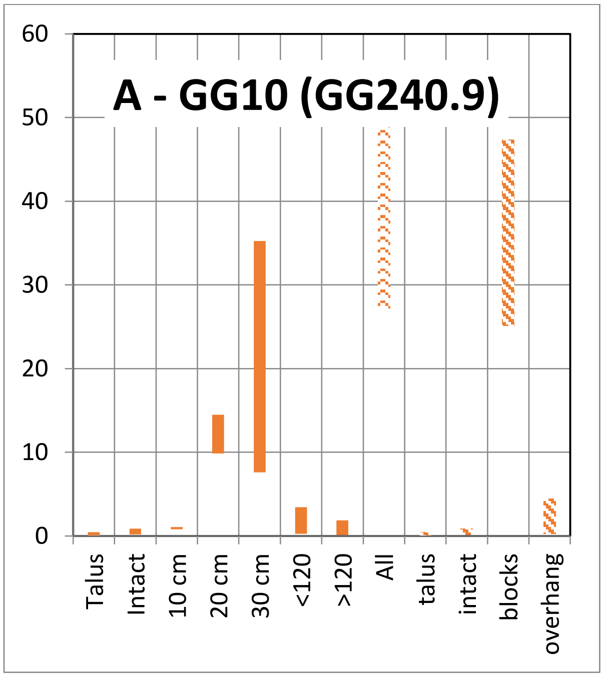
A - GG10 (GG240.9)
60
50
40
30
20
10
0
Talus
Intact
10 cm
20 cm
30 cm
<120
>120
All
talus
intact
blocks
overhang

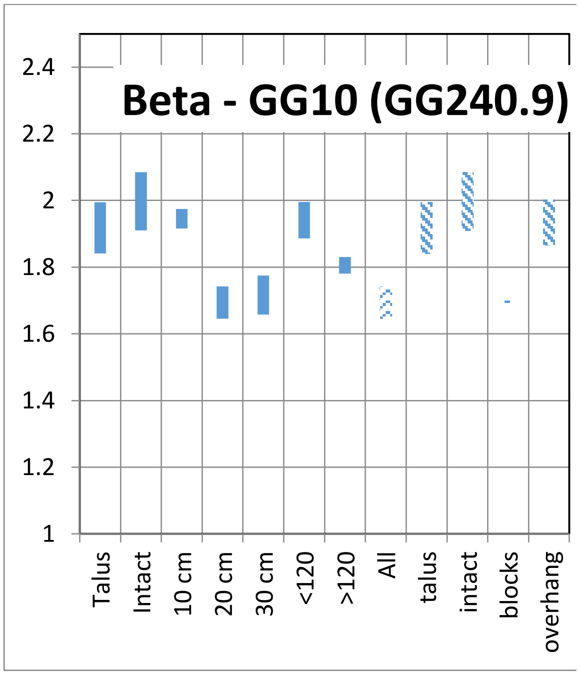
Beta - GG10 (GG240.9)
2.4
2.2
2
1.8
1.6
1.4
1.2
1
Talus
Intact
10 cm
20 cm
30 cm
<120
>120
All
talus
intact
blocks
overhang

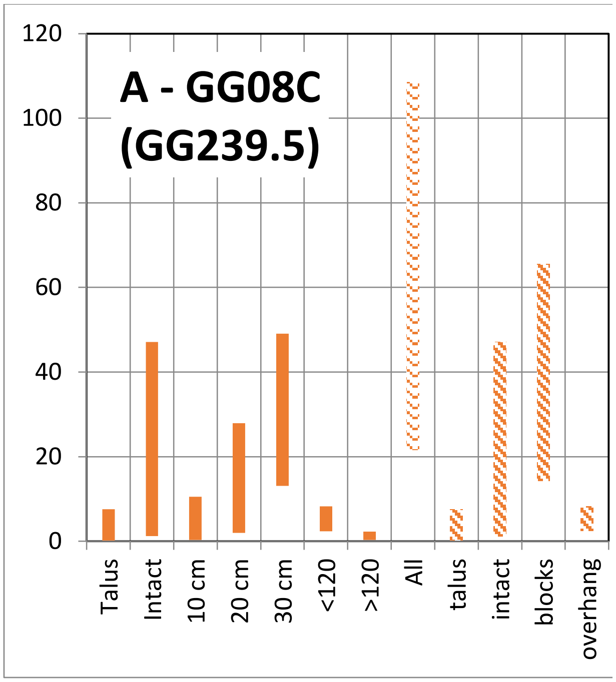
A - GG08C
(GG239.5)
120
100
80
60
40
20
0
Talus
Intact
10 cm
20 cm
30 cm
<120
>120
All
talus
intact
blocks
overhang

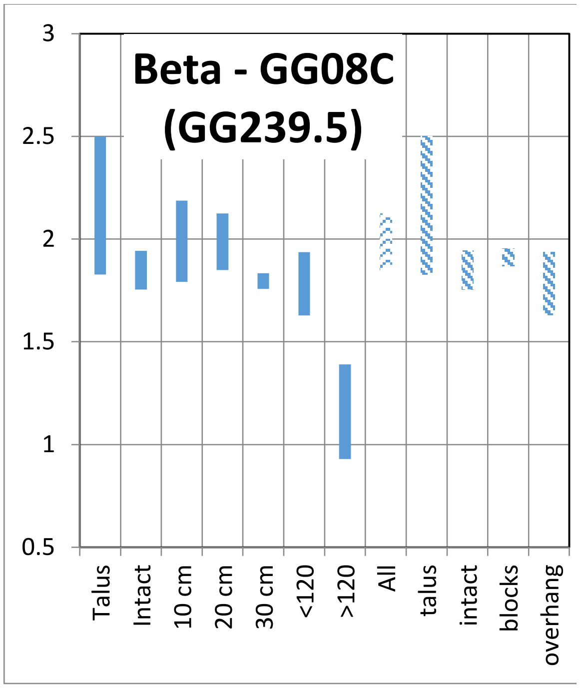
Beta - GG08C
(GG239.5)
3
2.5
2
1.5
1
0.5
Talus
Intact
10 cm
20 cm
30 cm
<120
>120
All
talus
intact
blocks
overhang

References

ASTM. (2005). *Standard test methods for determination of rock hardness by rebound hammer method ASTM 2005.D 873-05.*

Barlow, J., Lim, M., Rosser, N., Petley, D., Brain, M., Norman, E., et al. (2012). Modeling cliff erosion using negative power law scaling of rockfalls. *Geomorphology*, 416-424.

Barton, N., Lien, R., & Lunde, J. (1974). Engineering classifications of rock masses for the design of tunnel support. *Rock mechanics (Vol 6)*, 189-236.

Basu, A., & Aydin, A. (2004). A method for normalization of Schmidt hammer rebound values. *International Journal of Rock Mechanics and Mining Sciences*, 1211-1214.

Belowich, M. A. (2006). *Matanuska Coal Field.* Anchorage Alaska: Alaska geological Society.

Bieniawski, Z. T. (1973). Engineering classification of jointed rock masses. *Transactions of the Southe African Instituion of Civil Engineers 15(12)*, 335-344.

Brunetti, M., Guzzetti, F., & Rossi, M. (2009). Probablitity distributions of landslide volumes. *Nonlinear Processes in Geophysics*, 179-188.

Connor, C., & O'Haire, D. (1988). *Roadside Geology of Alaska.* Missoula: Mountain Press Publsihing Company.

Cunningham, K., Olsen, M., Wartman, J., & Dunham, L. (2015). *A Platform for Proactive, Risk-Based Slope Asset Management, Phase II.* Juneau, Alaska: Alaska Department of Transportation.

Deere, D. U., & Deere, D. W. (1988). *The Rock Quality Designation (RDQ) Index in Practice.* Philadelphia: American Society for Testing Materials.

Deere, D., & Miller, R. (1966). *Engineering classification and index properties for intact rocks (no AFNL-TR 65-116).* New Mexico: Tech Rep Air Fource Weapons Lab.

Dunham, L. A. (In Publication). *Creating a landslide hazard map of Christchurch in New Zealand.* Wellington, New Zealand: GNS-Science.

Ellsworth, P. (2013). Utah DOT Leveraging lidar for Asset Management Leap. *Lidar Magazine*.

Ericson, K. (2004). Geomorphological surfaces of different age and origin in granite landscapes: an evaluation of the Schmidt hammer test. *Earth Surf. Process Landforms 29*, 495-509.

Federal Highway Administration. (2014, September 2). *Asset Management*. Retrieved October 23, 2014, from US Department of Transporation: http://www.fhwa.dot.gov/asset/plans.cfm

FHWA. (2013). *Geotechnical Asset Managment: Publication No. FHWA-CFL/TD-13-003.* Lakewood Colorado: Federal Highway Administration.

Frankel, K. L., & Dolan, J. F. (2007). Characterizing arid region alluvial fan surface roughness with airborne laser swath mapping digital topographic data. *Journal of Geophysical research*.

Goudie, A. S. (2006). The Schmidt Hammer in geomorphological research. *Progress in Physical Geography*, 703-718.

Green, S. B. (1991). How many subjects does it take to do a regression analysis. *Multivariate behavioral research 26.3*, 499-510.

Hoek, E., & Brown, E. T. (1997). Practical estimates of rock mass strength. *International Journal of Rock mechanics and Mining Sciences 34(8)*, 1165-1186.

Huang, S. L., Darrow, M. M., & Calvin, P. (2009). *Unstable Slope Management Program - Background Research and Program Inception.* Alaska Department of Transportation and Public Facilities.

Landslide Technology R and M Consultants. (2010). *Alaska DOT and PF Unstable Slope management Program Detailed Rating Summary.* Alaska DOT.

Lato, M. J., Diederichs, M. S., & Hutchison, D. J. (2012). Evaluating roadside rockmasses for rockfall hazards using lidar data: optimizing data collection and processing protocols. *Natural Hazards 60 (3)*, 831-864.

Metzger, A. T., Olsen, M., Wartman, J., Dunham, L., & Stuedlein, A. (2014). *A Platform for Proactive Risk-Based Slope Asset Management - Phase I.* Seattle: Pacific Northwest Transportation Consortium (PacTrans) .

Miller, J. A., & Whitehead, R. L. (1999). *Ground Wather Atlas of the United States Alaska, Hawaii, Puerto Rico and the US Virgin Islands.* Retrieved April 17, 2015, from USGS: http://pubs.usgs.gov/ha/ha730/ch_n/N-AKsummary.html

Nicholson, D. T. (2004). Hazard assessment for progressive, weathering-related breakdown of excavated rockslopes. *Quarterly Journal of Engineering Geology and Hydrology, 37*, 327-346.

Olsen, M. J., Wartman, J., McAlister, M., Mahmaudabadi, H., O'Banion, M. S., Dunham, L., et al. (Submitted). Point cloud surface modeling and volumetric analysis for rockfall magnitude-frequency relationships.

Olsen, M. J., Young, A. P., & Ashford, A. S. (2012). TopCAT - Topographical Compartment Analysis Tool to analyze seacliff and beach change in GIS. *Computers and Geoscience 45*, 284-292.

O'Rourke, J. (1989). Rock index properties for geoengineering in underground development. *Min. Eng.*, 106-110.

Palmstrom, A. (1995). RMi - A system for characterizing rock mass strength for use in rock engineering. *Journal of Rock Mechanics and Tunnelling Technology, 1(2)*, 69-108.

Pierson, L. A. (1991). *Rockfall Hazard Rating System.* Washington, DC: Federal Highway Adminsitration.

R&M Consultants, INC. (2005). *Glennallen to palmer spur line soils study.* Anchorage, Alaska: R&M Consultants, INC. .

Rister, B., McIntosh, L., & Whelan, J. (2013). *Utilization of Mobile lidar to Verify Bridge Clearance Heights on the Western Kentucky Parkway.* Lexington, KY: University of Kentucky College of Engineering.

Romana, M. (1985). New adjustment ratings for application of Bieniawski classifaction to slpes. *International Symposium on the Role of Rock Mechanics*, 49-53.

Singh, B., & Goel, R. (2011). *Engineering Rock Mass Classification - Tunneling, Foundations andLandslides.* Oxford, UK.

Singh, R., Hassani, F., & Elkington, P. (1983). The application of strength and deformation index testing to the stability assessment of coal measures excavations. *Proc. 24th US Symp. On Rock Mech. Texas A and M Univ.* (pp. 599-609). Balkema, Rotterdam: AEG.

Split Engineering LLC. (1997-2015). Split-FX64 2.1.0. Tucson, Arizona, USA.

Thornberry-Ehrlich, T. (2010). *Denali national Park and Preserve: Geologic Resources Inventory Report.* Denver Colorado: National Parks Service.

Trop, J. M., & Plawman, T. L. (2006). *Bedrock geology of the Glenn Highway from Anchorage to Sheep Mountain, Alaska: Mesozoic-Cenozoic forearc basin development along an accretionary convergent margin.* Anchorage Alaska: Alaska Geologic Society.

Wahrhaftig, C., & Black, R. F. (1958). Engineering Geology along part of the Alaska Railroad. *Geological Survey Professional Paper 293*, 71-116.

Wilson, F. H., Dover, J. H., Bradley, D. C., Weber, F. R., Bundtzen, T. K., & Haeussler, P. J. (1998). *Geologic Map of Central (Interior) Alaska, U.S. Geological Survey Open-File Report OF 98-133.* Anchorage, Alaska: USGS.